

**ORGANO-MINERAL ASSOCIATIONS AND SEQUESTRATION  
MECHANISMS IMPACTING CARBON CYCLING IN DIVERSE  
TERRESTRIAL AND AQUATIC SYSTEMS**

by

Tyler Dale Sowers

A dissertation submitted to the Faculty of the University of Delaware in partial fulfillment of the requirements for the degree of Doctor of Philosophy in Plant and Soil Sciences

Spring 2019

© 2019 Tyler Dale Sowers  
All Rights Reserved

**ORGANO-MINERAL ASSOCIATIONS AND SEQUESTRATION  
MECHANISMS IMPACTING CARBON CYCLING IN DIVERSE  
TERRESTRIAL AND AQUATIC SYSTEMS**

by

Tyler Dale Sowers

Approved: \_\_\_\_\_

Erik Ervin, Ph.D.  
Chair of the Department of Plant and Soil Sciences

Approved: \_\_\_\_\_

Mark Rieger, Ph.D.  
Dean of the College of Agriculture and Natural Resources

Approved: \_\_\_\_\_

Douglas J. Doren, Ph.D.  
Interim Vice Provost for Graduate and Professional Education

I certify that I have read this dissertation and that in my opinion it meets the academic and professional standard required by the University as a dissertation for the degree of Doctor of Philosophy.

Signed:

---

Donald L. Sparks, Ph.D.  
Professor in charge of dissertation

I certify that I have read this dissertation and that in my opinion it meets the academic and professional standard required by the University as a dissertation for the degree of Doctor of Philosophy.

Signed:

---

Owen W. Duckworth, Ph.D.  
Member of dissertation committee

I certify that I have read this dissertation and that in my opinion it meets the academic and professional standard required by the University as a dissertation for the degree of Doctor of Philosophy.

Signed:

---

Jason W. Stuckey, Ph.D.  
Member of dissertation committee

I certify that I have read this dissertation and that in my opinion it meets the academic and professional standard required by the University as a dissertation for the degree of Doctor of Philosophy.

Signed:

---

Deb P. Jaisi, Ph.D.  
Member of dissertation committee

## ACKNOWLEDGMENTS

Throughout my experience pursuing a PhD at the University of Delaware, I've had the fortune of having incredible support from family, friends, and colleagues. I am blessed to have so many people in my life that want to see me succeed. Mary Beth, you were there to celebrate with me during the triumphs and to encourage me through the challenges of my graduate career. Without your support, this accomplishment would truly not have been possible. Grandma Sybil, a lady representing pure kindness, sent Mary Beth and I letters of encouragement and guidance ("Sybil Letters") throughout our time in Delaware and always warmed our spirits when we needed it most. Mom, the strongest person I've ever met, instilled all of the traits necessary for me to succeed. The Williams family has taken me in like one of their own since I jumped in the back of Mr. Frank's truck freshman year of undergrad on our way to an NCSU football game and I will always be grateful for their unwavering support. Jon, you're a brother to me, buddy. LJ and Tyler F., I'm so proud to call you both family.

I would also like to thank my committee members for their guidance throughout my PhD research. Owen, you have had my back for a long time and with each passing year, you continue to hold the guard. Thank you so much for your consistent advice, both professionally and as a friend. Dr. Sparks, Don, your incredible advice, encouragement, and support since the moment we talked has shaped my career, for which I'm grateful. I look forward to your mentorship for years to come.

Finally, I would like to thank all the members of our research group for their assistance and friendship. I look forward to our continued growth as scientists.

## TABLE OF CONTENTS

LIST OF TABLES .....	viii
LIST OF FIGURES .....	x
ABSTRACT .....	xviii

### Chapter

1	ORGANO-MINERAL ASSOCIATIONS AS A DRIVER OF OM CHEMISTRY IN TERRESTRIAL AND AQUATIC SYSTEMS .....	1
1.1	Introduction .....	1
1.2	The Importance of Soils in the Carbon Cycle .....	2
1.3	Metal Oxide-Mediated Sequestration of Organic Matter .....	5
1.4	Limited Investigation of Fe-Ca-OM Ternary Complexation .....	7
1.5	Natural Bacteriogenic Iron Oxides as a Reactive Sorbent .....	8
1.6	Organo-mineral Associations of Permafrost Systems .....	9
1.7	Knowledge Gaps and Motivation .....	10
1.8	Research Questions and Hypotheses .....	11
	REFERENCES .....	13
2	PROBING THE OCCURRENCE AND ORGANO-MINERAL ASSOCIATIONS OF IRON, CALCIUM, AND ORGANIC MATTER TERNARY COMPLEXES .....	20
2.1	Introduction .....	20
2.2	Materials and Methods .....	24
2.2.1	Natural and Laboratory Sources of OM .....	24
2.2.2	Synthetic 2-line Ferrihydrite Synthesis .....	25
2.2.3	Sorption Isotherms .....	26
2.2.4	Sorption Envelopes .....	28
2.2.5	Scanning Transmission X-ray Microscopy .....	29
2.2.6	Processing of STXM-NEXAFS Data .....	30
2.2.7	ATR-FTIR Spectroscopy .....	32
2.3	Results and Discussion .....	32

2.3.1	Effect of Ca on the on DOM and Citric Acid Sorption to Ferrihydrite .....	32
2.3.2	Effect of pH and Ca Concentration on DOM Sorption .....	35
2.3.3	Coupled Ca Decrease with Increasing pH in Batch Reactor Systems.....	38
2.3.4	Increased DOM Sequestration with Increasing Ca Concentration .....	39
2.3.5	Elemental Mapping of Fe, Ca, and C .....	40
2.3.6	Optical Density Correlation Between Elements.....	42
2.3.7	2.3.7 C K-edge STXM-NEXAFS of DOM.....	45
2.3.8	C K-edge STXM-NEXAFS Analysis of Citric Acid .....	49
2.3.9	Ca L-edge STXM-NEXAFS Analysis .....	50
2.3.10	ATR-FTIR.....	51
2.4	Evidence for Fe-Ca-OC Ternary Complex Formation.....	54
REFERENCES .....		74
3	NATURALLY-OCCURRING BACTERIOGENIC IRON OXIDES: AN UNDERSTUDIED, UNIQUE ORGANIC MATTER SINK.....	80
3.1	Introduction .....	80
3.2	Materials and Methods .....	84
3.2.1	Dissolved Organic Matter Extraction and Characterization.....	84
3.2.2	Collection of Bacteriogenic Iron Oxides.....	85
3.2.3	Characterization of BIOs.....	86
3.2.4	Scanning Transmission X-ray Microscopy .....	87
3.2.5	STXM-NEXAFS Data Processing .....	88
3.2.6	Desorption of Native Organic Carbon.....	89
3.2.7	Sorption of Organic Matter and Humic Standards to Bacteriogenic Iron Oxides.....	89
3.2.8	Fourier Transform-Ion Cyclotron Resonance-Mass Spectrometry Analysis.....	91
3.2.9	Spectral Post-Processing .....	92
3.2.10	Intensity-Normalized Quantification of Adsorption and Relative Abundance.....	95
3.2.11	Attenuated Total Reflectance-Fourier Transform Infrared Spectroscopy.....	96
3.3	Results and Discussion .....	96
3.3.1	Investigating BIO Morphology and Native Organic Carbon Chemistry .....	96

3.3.2	Sorption of Dissolved Organic Matter to BIOs .....	99
3.3.3	Solid Phase Organic Matter Speciation .....	102
3.3.4	FT-ICR-MS Analysis of Pre- and Post-sorption DOM .....	104
3.3.5	Effect of Oxygenation on Organic Matter Sorption .....	106
3.4	BIOs as an Emergent Sorbent of Dissolved Organic Matter .....	108
REFERENCES	.....	132
4	ADVANCED SPATIALLY-RESOLVED ANALYSIS OF PERMAFROST ORGANO-MINERAL ASSOCIATIONS .....	140
4.1	Introduction .....	140
4.2	Materials and Methods .....	144
4.2.1	Collection and Preparation of Permafrost Samples .....	144
4.2.2	Scanning Transmission X-ray Microscopy .....	146
4.2.3	STXM-NEXAFS Data Processing and Principal Component Analysis .....	147
4.3	Results and Discussion .....	148
4.3.1	RGB and Optical Density Correlations for C, Ca, Fe .....	148
4.3.2	RGB and Optical Density Correlations for C, Al, Si .....	152
4.3.3	Carbon NEXAFS and PCA .....	156
4.3.4	Iron NEXAFS and PCA .....	160
4.3.5	Calcium NEXAFS .....	163
4.3.6	Aluminum and Silicon NEXAFS .....	164
4.4	Conclusions .....	165
REFERENCES	.....	183
Appendix		
A	PROBING THE OCCURRENCE AND ORGANO-MINERAL ASSOCIATIONS OF IRON, CALCIUM, AND ORGANIC MATTER TERNARY COMPLEXES .....	190
A.1	Copyright Information .....	190
B	NATURALLY-OCCURRING BACTERIOGENIC IRON OXIDES: AN UNDERSTUDIED, UNIQUE ORGANIC MATTER SINK .....	191
B.1	Copyright Information .....	191

## LIST OF TABLES

Table 2.1:	Aqueous carbon concentrations of DOM stock solution.....	57
Table 2.2:	Aqueous elemental composition of DOM stock solution. ....	57
Table 2.3:	Observed peak positions for ATR-FTIR spectra. Peak assignments and references supporting assignment are included. ....	58
Table 2.4:	Pre-edge energy and edge-energy ranges used for average stack maps, along with optical density conversion factors used to convert optical density to elemental thickness. ....	59
Table 2.5:	Values used to convert the C optical density to C thickness. ....	59
Table 2.6:	Langmuir parameters used to model sorption of DOM and citric acid to 2-line ferrihydrite. ....	60
Table 2.7:	C 1s NEXAFS peak energies with C functional group interpretation. ...	61
Table 3.1:	DOM and BIO chemical composition and zeta potential at pH 6.5, with BET surface area for BIO. All values are reported within 10% error. ....	111
Table 3.2:	Molecular composition of DOM stock and DOM-reacted BIO (BIO <sub>200</sub> ). Relative abundancy is reported normalized to total spectral intensity. ....	111
Table 3.3:	FT-ICR-MS abundancy in DOM versus BIO <sub>200</sub> by peak count and total peak intensity of specific organic compound classes.....	111
Table 3.4:	FT-ICR-MS abundancy in DOM extracted from leaf litter for 24 hrs by peak count and total peak intensity of specific organic compound classes. This DOM was not used in sorption experiments. ....	112
Table 3.5:	Pre-edge energy and edge-energy ranges used for average stack maps for C and Fe. Values were chosen according to the authors' previous research (Chen et al., 2014a; Sowers et al., 2018). ....	112
Table 3.6:	Desorption of BIO native OC using four different desorbing reagents.	113

Table 3.7:	Langmuir model fitting parameters used to fit sorption isotherm data presented in Fig. 2a, where S is sorbed concentration, $S_{\max}$ is the calculated maximum sorption, K is a sorption constant, C is dissolved sorbate concentration, and E is model efficiency.....	113
Table 3.8:	Langmuir model fitting parameters used to fit sorption isotherm data presented in Fig. 2b, where S is sorbed concentration, $S_{\max}$ is the calculated maximum sorption, K is a sorption constant, C is dissolved sorbate concentration and E is model efficiency.....	114
Table 3.9:	ATR-FTIR peak positions shown in Figure 3.11, with interpreted assignments and corresponding references. ....	115
Table 4.1:	Elemental composition of permafrost soils following digestion using EPA Method 3051 ( <i>aqua regia</i> digestion). All values are reported as percent by mass, with an error of approximately 0.1%. ....	168
Table 4.2:	Pre-edge energy and edge-energy ranges used for average stack maps.....	169
Table 4.3:	Carbon K-edge NEXAFS assignments observed in Figure 4.8. ....	170

## LIST OF FIGURES

- Figure 2.1: DOM (a) and citric acid (b) were reacted with ferrihydrite at pH 6.25  $\pm$  0.10 in duplicate. Samples were treated with and without Ca addition. Sample receiving Ca had a total Ca concentration of 4 mM Ca (152 mg Ca L<sup>-1</sup>)..... 62
- Figure 2.2: Sorption envelopes of DOM sorption to ferrihydrite at pH 4 to 9 in the presence of no added Ca (a), 10 mM Ca (b), or 30 mM Ca (c). An initial C/Fe ratio of 4.7 was used for all samples and experiments were performed in triplicate. .... 63
- Figure 2.3: Aqueous Ca data from sorption envelope experiments conducted from pH 4 to 9. The multicomponent systems consisted of Ca and ferrihydrite or Ca, ferrihydrite, and DOM. The greater decrease in aqueous Ca in the DOM multicomponent system compared to the system without DOM is thought to occur due to ternary interactions of ferrihydrite, Ca, and DOM. .... 64
- Figure 2.4: Sorption of DOM to 2-line ferrihydrite at 4.7 and 12.5 initial C/Fe molar ratios with increasing calcium concentration (up to 60 mM Ca) at pH 6.25  $\pm$  0.10. .... 65
- Figure 2.5: Color-coded composite RGB optical density maps created from STXM-NEXAFS data. Red, green, and blue represent carbon, calcium, and iron, respectively. RGB maps are shown for ferrihydrite-DOM (A), ferrihydrite-Ca-DOM (B), ferrihydrite-citric acid (C), and ferrihydrite-Ca-citric acid samples (D). Cyan regions in Figure 1A and Figure 1D were identified as regions too thick for transmission. .... 66
- Figure 2.6: Elemental optical density correlation plots between C, Ca, and Fe for DOM-bearing (A-C) and citric acid-bearing (D-F) ferrihydrite. Linear correlation coefficients are provided for each plot. Thickness values for each element are also provided (calculated using SI Table S3). .... 67
- Figure 2.7: Optical density correlation plots of Ca versus Fe for ferrihydrite samples reacted with DOM (left) or citric acid (right) in the presence of Ca. .... 68

Figure 2.8: C K-edge STXM average stack optical density map for ferrihydrite-DOM of the C K-edge (287.7-288.8 eV) and the C K-edge minus C pre-edge (287.7-288.8 eV minus 280-282 eV) difference map are shown in A and B, respectively. PCA of the C K-edge stack is shown in C and respective C 1s STXM-NEXAFS spectra for the whole sample and each of the 3 clusters identified through PCA are shown in D. A standard of the DOM stock is also included. Peak assignments are located in Table 7. ....	69
Figure 2.9: C K-edge STXM average stack optical density map for ferrihydrite-Ca-DOM of the C K-edge (287.7-288.8 eV) and the C K-edge minus C pre-edge (287.7-288.8 eV minus 280-282 eV) difference map are shown in A and B, respectively. PCA of the C K-edge stack is shown in C and respective C 1s STXM-NEXAFS spectra for the whole sample and each of the 3 clusters identified through PCA are shown in D. A standard of the DOM stock is also included. <sup>9</sup> Peak assignments are located in Table 7. ....	70
Figure 2.10: C K-edge STXM PCA for ferrihydrite-citric acid and ferrihydrite-Ca-citric acid samples is shown in A and B, respectively. Only one unique cluster was identified for each sample. The region of interest is highlight in yellow in A and in red in B. The contrasting color represent areas of too much sample thickness and were not used in analysis. Corresponding C 1s NEXAFS spectra for A and B are shown in C. Whole sample regions for ferrihydrite-DOM and ferrihydrite-Ca-DOM samples are included as a comparison to citric acid spectra, along with a DOM standard. Peak assignments are located in Table 7. ....	71
Figure 2.11: Ca 2p NEXAFS spectra for DOM and citric acid samples that were reacted with ferrihydrite in the presence of 30 mM Ca. The samples were compared to a Ca-bearing ferrihydrite standard (Fh_Ca) synthesized similarly to Fh_Ca_DOM and Fh_Ca_Citric acid, but in the absence of DOM. Previously published reference standards for Ca sorbed to extracellular polymer structures, CaCl <sub>2</sub> , and calcite are also included. ....	72
Figure 2.12: ATR-FTIR spectra for ferrihydrite samples reacted with either DOM or citric acid in the absence or presence of Ca. A molar C/Fe ratio of 2.5 or 4.7 was used for DOM samples in order to reveal spectra features that may be difficult to distinguish at high molar C/Fe ratios. A reference standard for the stock DOM used for DOM reactions is also included. ....	73

Figure 3.1: Conceptual model of the natural formation of bacteriogenic iron (oxyhydr)oxides (BIOs) in an aqueous system and the interactions hypothesized with organic carbon both during and after formation. Formation of BIOs via oxidation of Fe(II) by iron oxidizing bacteria (A). Organic carbon is incorporated into the mineral during BIOs formation via coprecipitation and sorbed to the surface after formation. The surface texture of these poorly crystalline structures is a fibrous network of highly associated Fe and C (B). Surficial hydroxyl groups on BIO sheaths are expected to exchange predominately with carboxylic moieties (C). Specific OC functional moieties are preferentially exchanged with the surface of BIOs, resulting in moiety-dependent OC sequestration and mobilization (D). ..... 116

Figure 3.2: Naturally-occurring bacteriogenic iron oxides (BIOs) with visible sheens and corresponding biomass observed at the macroscale (A) and field scale (B). Images were taken at White Clay Creek, Newark, Delaware..... 117

Figure 3.3: Generalized schematic of biogenic iron (oxyhydr)oxides collected from White Clay Creek, DE. Observed sheath/rod-like morphology is characteristic of Fe(II)-oxidizing bacteria *Leptothrix* and is expected to be responsible for surface interactions with potential sorptives. Incorporated cell-derived organic matter and surrounding EPS biomass is expected to affect reactivity. Native OC is used in the manuscript to refer to OC already present upon BIOs collection, which includes cell-derived OM and previously sorbed/coprecipitated OC. .... 118

Figure 3.4: X-ray diffractograms for synthetic 2-line ferrihydrite (A) and BIO (B). BIOs was found to correspond well to the beat pattern of 2-line ferrihydrite, along with the inclusion of quartz grains. .... 119

Figure 3.5:	STXM optical density RGB image for BIO (A) paired with NEXAFS spectra at specific regions of interest at the interior or exterior of a BIO sheath (B). Red, green, and blue represent carbon, calcium, and iron, respectively. Purple regions represent areas of high C and Fe correlation whereas cyan regions were identified as areas too thick for transmission (optical density $\geq 2.5$ ). Red coating present at the edges of the sheaths resemble potential C accumulations. NEXAFS spectra show unique OC speciation consisting of (i) aromatic (285.4-285.6 eV), (ii, iii) ketone carbonylic (286.5 eV), (iv) aliphatic (287.4 eV), (v) carboxylic (288.5 eV), and (vi) polysaccharide-associated aliphatic (289.8 eV) functional moieties.....	120
Figure 3.6:	Sorption isotherm plot of DOM, Suwannee River Fulvic Acid (SRFA), or Suwannee River Humic Acid (SRHA) sorption to BIOs (A) compared to surface area-normalized sorption data for DOM sorption to BIOs or synthetic 2-line ferrihydrite (B), followed by desorption of OC from DOM-reacted BIO samples (C). A single Langmuir fit was found to fit both the DOM and SRFA data sets (model efficiency = 0.965) and surface area normalization resulted in a strong Langmuir fit (0.931) for both 2-line ferrihydrite and BIO reacted with DOM. ....	121
Figure 3.7:	Sorption isotherm for DOM sorption to BIO or synthetic 2-line ferrihydrite. Sorption data is normalized to mass of sorbent. ....	122
Figure 3.8:	Sorption isotherm for DOM sorption to BIO or synthetic 2-line ferrihydrite. Sorption data is normalized to the Fe content of the sorbent. ....	123
Figure 3.9:	OC sorption to BIO isotherm (A) with corresponding desorption results (B) for samples reacted at low initial OC concentrations. ....	124
Figure 3.10:	Desorption of SRHA (a) and SRFA (b) from BIOs that were reacted with SRHA or SRFA at OC concentrations ranging from 100 to 800 mg L <sup>-1</sup> . ....	125

- Figure 3.11: ATR-FTIR spectra showcasing potential mechanisms of OM sorption to BIOs and OC species preferentially sequestered. Primary features of interest (Table 3.9) include a shifted asymmetric carboxylic stretch for DOM-reacted BIO (i), asymmetric carboxylic stretch of DOM (ii), aromatic C=C stretching for all spectra (iii), ligand exchanged Fe-COO stretch for all Fe oxide samples (iv), phenolic stretching found only for DOM (v), carboxylic associated-carbohydrate stretching for DOM-reacted BIOs (vi). 1040 to 1005  $\text{cm}^{-1}$  represents the major involvement of BIOs with polysaccharides, with distortions of DOM-reacted BIOs attributable to enrichment by carboxylic moieties. .... 126
- Figure 3.12: ATR-FTIR results for SRHA and SRFA standards. Dominant peaks are found at 1720, 1620, 1400, 1270-1250, and 1225-1200  $\text{cm}^{-1}$ , with corresponding assignments found in Table 3.9. .... 127
- Figure 3.13: van Krevelen diagrams of unreacted DOM (A) compared to BIOs-reacted DOM (BIO<sub>200</sub>) (B). For A, assigned OC compound classification is shown. For B, the degree of sorption is displayed as highly or completely sorbed (dark purple), partially sorbed (color index), or low/no sorption (yellow), derived from spectral intensity pre- and post-sorption (see SI). The relative intensity index modeling sorption of DOM to BIOs was calculated by dividing BIO<sub>200</sub> by the peak intensity of the DOM before sorption. Color-scale indicates this index value, with lower index values signifying high extent of adsorption, while greater values indicate low extent of adsorption. Samples that are at a value of zero may be affected by low initial signal intensity; however, all sorption trends are supported by FTIR analysis of the BIO solid phase. .... 128
- Figure 3.14: van Krevelen diagrams of pre-sorption initial DOM (A) and post-sorption formulae, as categorized by a relative intensity index (see SI for calculation), deemed partially adsorbed to BIOs (B). Colorscale for B indicates this index value, with lower index values indicating high extent of adsorption, while greater values are of indicative of low extent of adsorption. .... 129

Figure 3.15: Molecular fractionation of sorbed OC parsed by formulae O content (O-number). Changes in relative abundance ( $\Delta$ %) of compound classes were parsed by formulae O-number, in which the abundance of post-sorption formulae in each compound class and O-number were compared to that observed in initial, unexposed DOM. The relative abundances of formulae within each O-number and compound class found for the initial DOM was then subtracted from the BIO <sub>200</sub> normalized relative abundances, resulting in a $\Delta$ % value. Positive percentages correspond to enrichment as a result of high sorption of other compounds or as release of native OC from BIO. Negative percentages indicate preferential sorption to BIOs. ....	130
Figure 3.16: The double bond equivalence (DBE) and formulae oxygen number (0 - 25) of compounds in initial DOM (open circles) overlaid by those detected post-sorption to BIOs (closed circles).....	131
Figure 4.1: Cross-section of the Permafrost Tunnel Research Facility operated by the US Army Corps of Engineers Cold Regions Research and Engineering Laboratory (CREEL) in Fairbanks, Alaska. The sampling locations of four permafrost soils are shown as PT_A, PT_B, PT_C, and AT.....	171
Figure 4.2: Color-coded composite RB and RGB optical density maps created from STXM-NEXAFS data. Red, green, and blue represent carbon, calcium, and iron, respectively. Maps are shown for soils PT_A (A, B) and PT_B (C, D).....	172
Figure 4.3: Color-coded composite RB and RGB optical density maps created from STXM-NEXAFS data. Red, green, and blue represent carbon, calcium, and iron, respectively. Maps are shown for soils PT_C (A, B) and AT (C, D).....	173
Figure 4.4: Elemental optical density correlation plots for spatially-resolved C signature versus Fe (A-C) and C versus Ca (D-E) for all PT soils. Linear correlation coefficients are provided for each plot. ....	174
Figure 4.5: Elemental optical density correlation plots for spatially-resolved Fe signature versus Ca for soil PT_C. Linear regression revealed Fe and Ca to be strongly correlated ( $R^2 = 0.78$ ). All other soils had no observable correlation between Fe and Ca.....	175

- Figure 4.6: Color-coded composite RGB optical density maps created from STXM-NEXAFS data. Red, green, and blue represent carbon, aluminum, and silicon, respectively. Maps are shown for soils PT\_A (A), PT\_B (B), PT\_C (C). Note the coating of C to Al and Si phases without overlap, suggesting a lack of sorbed C by these phases. Al and Si phases are likely clay phyllosilicates mixed with quartz fragments. 176
- Figure 4.7: Elemental optical density correlation plots for spatially-resolved Si signature versus Al for a PT soil (PT\_C; A) compared to an AT soil (B). A linear regression line is present for each, with the slope indicating Si:Al ratio. Clay aluminosilicates typically have either a 1:1 or 2:1 ratio of tetrahedral to octahedral sheets, typically representing Si:Al. Therefore, PT\_C (Si:Al = 1.4) is likely a mixture of 2:1 and 1:1 aluminosilicates whereas AT (Si:Al = 2.5) likely consists predominately of 2:1. Values higher than 2 suggest that a component of the observed Si is potentially from sources other than clays, such as quartz. .... 177
- Figure 4.8: Carbon K-edge NEXAFS spectra (A) for unique clusters spatially identified using principal component analysis (PCA) for soils PT\_A (B), PT\_B (C), PT\_C (D), AT\_C (E). All spectra are color-coded to match the adjacent respective PCA map. Yellow regions were too thick (OD >2.25) for analysis. NEXAFS spectra for DI water-extractable leaf litter DOM and DOM sorbed to 2-line ferrihydrite are also included as standards. Peak assignments are found in Table 4.3... 178
- Figure 4.9: Iron L-edge NEXAFS spectra (A) for unique clusters spatially identified using principal component analysis (PCA) for soils PT\_A (B), PT\_B (C), PT\_C (D), AT\_C (E). All spectra are color-coded to match the adjacent respective PCA map. Yellow regions, excluding PT\_B, were too thick (OD >2.25) for analysis. Reference compounds of FeO and Fe<sub>2</sub>O<sub>3</sub> are included to comparatively assess the proportion of Fe(II) versus Fe(III), respectively, in samples. Vertical dashed lines correspond to (i) 708, (ii) 710, (iii) 721, and (iv) 723 eV. .... 179
- Figure 4.10: Calcium L-edge NEXAFS spectra for all permafrost soils, along with previously published reference standards for Ca sorbed to extracellular polymer structures, CaCl<sub>2</sub>, and calcite (Chen et al., 2014a). Vertical dashed lines correspond to (i) 348.2, (ii) 349.3, (iii) 351.4, and (iv) 352.6 eV. .... 180
- Figure 4.11: Aluminum L-edge NEXAFS spectra for soils PT\_A, PT\_C, and AT, along with a muscovite reference standard. Vertical dashed lines correspond to (i) 1565.6, (ii) 1567.7, and (iii) 1570.0 eV. .... 181

Figure 4.12: Silicon L-edge NEXAFS spectra for soils PT\_A, PT\_C, and AT, along with quartz and muscovite as reference standards. Vertical dashed lines correspond to (i) 1846.5, (ii) 1850.4, (iii) 1854.6 eV, and (iv) 1857.0. .... 182

## ABSTRACT

Sequestration of organic matter (OM) in environmental systems is critical to mitigating climate change. Organo-mineral associations, especially those with iron (Fe) oxides, drive the chemistry of OM sequestration and stability in soils. In the past 20 years, research exploring the sequestration of OM to Fe oxides has intensified. Poorly crystalline Fe oxides, such as ferrihydrite, demonstrate a high affinity for OM in binary systems. Calcium commonly co-associates with OM and Fe oxides in soils, though the bonding mechanism (e.g., cation bridging) and implications of the co-association for OM sequestration remain unresolved. The biogeochemical cycling of OM in systems containing biogenically-produced Fe oxides and in permafrost conditions is also poorly understood. In an effort to gain an environmentally comprehensive understanding of C cycling in chemically heterogeneous systems, we explored the effect of calcium ( $\text{Ca}^{2+}$ ), biogenic Fe oxides, and permafrost conditions on the cycling of OM.

Extensive batch and advanced spectroscopic experiments were used to investigate the occurrence and importance of Fe, Ca, OM ternary associations. Sorption experiments conducted at pH 4 to 9 at varying initial C/Fe molar ratios and  $\text{Ca}^{2+}$  concentrations were completed to determine the effects of  $\text{Ca}^{2+}$  on leaf litter-extractable OC sequestration to ferrihydrite. OC sorption extent to ferrihydrite in the

presence of  $\text{Ca}^{2+}$  increased across all tested pH values, especially at  $\text{pH} > 7$ . Sorbed OC concentration at pH 9 increased from 8.72 to 13.30 mmol OC  $\text{g}^{-1}$  ferrihydrite between treatments of no added  $\text{Ca}^{2+}$  and 30 mM  $\text{Ca}^{2+}$  addition. Batch experiments were paired with spectroscopic studies to probe sorbed OC speciation and mechanism of sorption complexes. ATR-FTIR spectroscopy analysis revealed that carboxylic functional moieties were the primary sorbed OC species and suggested an increase in Fe-carboxylate ligand exchange in the presence of Ca at pH 9. STXM-NEXAFS was used to spatially resolve Fe, Ca, and OC relationships and to probe the effect of Ca on sorbed OC speciation. Organic carbon was found to highly associate with Ca ( $R^2 = 0.91$ ). Carboxylic acid moieties were dominantly sequestered; however, Ca facilitated the additional sequestration of aromatic and phenolic moieties. Also, C NEXAFS revealed polyvalent metal ion complexation. Results from batch and spectroscopic experiments provide significant evidence for the enhancement of dissolved OC sequestration to 2-line ferrihydrite and suggest the formation of Fe-Ca-OC ternary complexes.

Bacteriogenic iron (oxyhydr)oxides (BIOs), common to quiescent waterways and soil redox transitions, possess a high affinity for oxyanions (i.e., arsenate and chromate); therefore, we investigated BIOs reactivity for OM due to similar interactions with carboxylic acids. Using adsorption and desorption batch reactions, paired with Fourier transform infrared spectroscopy and Fourier transform ion cyclotron resonance mass spectrometry, this work demonstrates that BIOs are capable of sorbing leaf litter-extracted DOM and Suwannee River Humic/Fulvic Acid

(SRHA/SRFA) and have sorptive preference for distinct organic carbon compound classes at the biomineral interface. BIOs were found to sorb DOM and SRFA to half the extent of 2-line ferrihydrite per mass of sorbent and were resilient to desorption at high ionic strength and in the presence of a competitive ligand. We observed the preferential sorption of aromatic and carboxylic-containing species and concurrent solution enrichment of aliphatic groups unassociated with carboxylic acids. These findings suggest that DOM cycling may be significantly affected by BIOs, which may impact nutrient and contaminant transport in circumneutral environments.

Similarly, we performed advanced spectroscopic experiments for permafrost collected across a chronosequence gradient in Fairbanks Alaska. Using STXM-NEXAFS spectroscopy, we found high correlations of C and Fe across all permafrost samples, suggesting that global climate change, with accompanying temperature increases facilitating thawing conditions, may create redox conditions that directly impact the stability of C-Fe organo-mineral associations. We also observed spatially heterogeneous OM speciation in permafrost OM that ranges in age from 19,000 to 36,000 years old. Permafrost stores approximately 50% of global soil carbon and this research indicates that modeling Fe cycling with fluctuating global temperatures may greatly dictate the transfer of terrestrial OM. Ongoing investigations by me, our research group, and others are needed to elucidate the impacts of OM stability when exposed to oscillating redox conditions created by newfound freeze-thaw conditions.

## Chapter 1

# ORGANO-MINERAL ASSOCIATIONS AS A DRIVER OF OM CHEMISTRY IN TERRESTRIAL AND AQUATIC SYSTEMS

### 1.1 Introduction

Globally, soil organic matter (OM) sequesters more carbon (C) than the atmosphere and above-ground vegetation combined (Amundson, 2001; Schmidt et al., 2011). Soil OM acts a reservoir for C, making OM a vital component to ensuring soil health and productivity (Amundson, 2001; Davidson et al., 2000; Riley et al., 2014; Schmidt et al., 2011). Further, the sequestration of C as OM prevents additional C transfer to the atmosphere (Schmidt et al., 2011; Sparks, 2003b). Instability of OM may lead to increased atmospheric C inputs, a primary mechanism of climate change (Amundson, 2001; Schmidt et al., 2011; von Lützow and Kögel-Knabner, 2009). Recent research has suggested that OM stability is controlled by complex interactions with environmental media (Kaiser and Guggenberger, 2003; von Lützow et al., 2008). Minerals, such as iron (Fe) oxides, have a profound effect on OM stability and have been studied extensively in the past 20 years (Gu et al., 1995; Lalonde et al., 2012; Wagai and Mayer, 2007). However, there remains a lack of knowledge concerning the mechanisms of organo-mineral associations and how these associations may behave

uniquely in terrestrial and aquatic systems with diverse Fe phases. Therefore, **this research sought to investigate the potential for Fe-Ca-OM ternary complex formation through Ca-bridging, to determine the potential for streamwater-collected bacteriogenic Fe oxides to sequester OM, and to explore the C cycling processes occurring across a consequence gradient in a permafrost soil system.** Exploring the impact of organo-mineral processes on the C cycle in these unique systems has the potential to lead to advances in climate change mitigation, soil fertility, stream water nutrient management, and organic contaminant mobility.

## **1.2 The Importance of Soils in the Carbon Cycle**

Soil OM stores approximately two to three times the quantity of C that is found in the atmosphere (Davidson et al., 2000; Schmidt et al., 2011). Mobilization of C to the atmosphere has far-reaching implications that most notably can impact climate and soil productivity (Meehl et al., 2007; Post and Kwon, 2000; Sparks, 2003a), making it critical to fully understand the processes controlling C transformation one of the world's largest C reservoirs (soil OM). Climate change, whether it be anthropogenically or naturally-driven, is occurring and there are major uncertainties as to how OM will respond (Riley et al., 2014; Schmidt et al., 2011). A primary concern is that increasing global temperatures may facilitate the degradation of soil OM (von Lützow and Kögel-Knabner, 2009; von Lützow et al., 2008), ultimately leading to transfer of C to the

atmosphere (Amundson, 2001; Riley et al., 2014; Schmidt et al., 2011; von Lützow and Kögel-Knabner, 2009). Also, variations in redox state, potentially facilitated by climate change-induced sea level rise, may add to this transfer as OM degradation is facilitated (Riley et al., 2014; Schmidt et al., 2011; von Lützow et al., 2008). Loss of C from terrestrial systems may significantly exacerbate the issue of climate change due to the high concentration of C added as CO<sub>2</sub> and/or CH<sub>4</sub>, leading to a range of effects that impact on a global scale. Two major consequences of atmospheric C loading are the intensification of global warming and ocean acidification (Cox et al., 2000; Kleypas et al., 1999; Lal, 2004; Meehl et al., 2007). CO<sub>2</sub> is a greenhouse gas; therefore, increased atmospheric loading of CO<sub>2</sub> will result in increased warming (Solomon et al., 2009). This has major implications on a range of environmental conditions, one of which is increased sea level rise (Galbraith et al., 2002; Meehl et al., 2007). Ocean acidification is also occurring as a result of increased atmospheric CO<sub>2</sub> concentration dissolving into the ocean, resulting in decreased pH (Meehl et al., 2007). This phenomenon has the potential to decrease the biodiversity of ocean organisms (Kleypas et al., 1999; Meehl et al., 2007), resulting in both biological and economic repercussions.

Although OM plays a major role in mediating climate change, soil OM is also critical to soil productivity. Soils with high OM content have the potential to be excellent for crop production due to high porosity, cation exchange capacity, and microbial diversity (Sparks, 2003b); however, changing environmental conditions

pose a threat to the productivity of these farming systems. Climate change is expected to be influencing soil OM stability because of changes in soil temperature and water (Davidson et al., 2000; Post and Kwon, 2000; von Lützow and Kögel-Knabner, 2009), which may diminish soil fertility. Further, land use may alter soil OM stability, as soils typically used for cultivating crops are highly susceptible to C mobilization (Mann, 1986; Schlesinger, 1986). However, the coupled impacts of land use and changing environmental conditions on the stability of OM associated with common soil metal oxide minerals are unknown. These uncertainties have the potential to not only adversely affect the livelihoods of farmers but will also negatively affect consumers of agricultural products. Increased understanding of C cycling in stream water systems is also critically important.

As a result of the far-reaching consequences of environmental OM stability, research focusing on the biogeochemical cycling of C has intensified over the past 20 years (Davidson et al., 2000; Gu et al., 1995; Lalonde et al., 2012; Post and Kwon, 2000; Six et al., 2002). However, major gaps remain in current C cycling models due to poorly understood C interactions between OM and minerals exposed to varying biogeochemical conditions. The proposed research aims to significantly contribute to filling these knowledge gaps to expand scientific understanding of environmental C cycling. Conducting research that addresses the stability and accumulation of OM in

variable environments and biogeochemical conditions will provide insights that positively impact anthropogenic well-being.

### **1.3 Metal Oxide-Mediated Sequestration of Organic Matter**

Metal oxide minerals are critical to the sequestration of C in environmental systems (Mikutta et al., 2007; Post and Kwon, 2000; Six et al., 2002). Extensive research has shown that metal oxide minerals may form a protective sorption complex with OM (Gu et al., 1995; Kaiser and Guggenberger, 2000; Kaiser and Guggenberger, 2003; Lalonde et al., 2012; Mikutta et al., 2007; Shaker et al., 2012; Wagai and Mayer, 2007). Fe, Mn, and Al oxide minerals are primary OM-stabilizing soil constituents (Mikutta et al., 2007; Schneider et al., 2010; Wagai and Mayer, 2007); however, Fe(III) oxide minerals are of particular environmental importance as these minerals are found ubiquitously in terrestrial systems and possess high reactivity for OM (Cismasu et al., 2011; Cornell and Schwertmann, 2003; Jambor and Dutrizac, 1998; Kaiser and Guggenberger, 2003). Although aluminosilicate clay minerals, a major soil constituent, also sequester organic carbon (OC), the extent of sorption is lower than that of Fe(III) oxide minerals by approximately an order of magnitude (Chorover and Amistadi, 2001). Short-range-ordered Fe(III) mineral phases, such as 2-line ferrihydrite, are of primary importance as these phases have the highest surface area and reactivity compared to more crystalline phases (Cornell and Schwertmann, 2003; Duckworth et al., 2009; Gu

et al., 1995; Michel et al., 2007; Waychunas et al., 1993). For example, 2-line ferrihydrite has been reported to sorb approximately 225 mg OC g<sup>-1</sup> mineral (Chen et al., 2014b; Kaiser and Guggenberger, 2003; Wagai and Mayer, 2007). Also, sorbed OM has been found to have a strong hysteresis effect (Gu et al., 1995; Kaiser and Guggenberger, 2000); therefore, the Fe-OM sorption complexes are resilient to desorption. Organic matter sorption to Fe(III) (oxyhydr)oxides has been found to dominantly occur through ligand exchange mechanisms (Feng et al., 2005; Gu et al., 1995; Mikutta et al., 2007). These inner-sphere sorption mechanisms largely occur through exchange of OM carboxyl functional moieties with hydroxyl groups (Chen et al., 2014a; Chen et al., 2014b; Gu et al., 1995; Mikutta et al., 2007; Post and Kwon, 2000; Wagai and Mayer, 2007). Aromatic groups have also been found to be associated with Fe, though potentially through carboxyl attachment to aromatic rings (Chen et al., 2014b). OM sorption to Fe(III) (oxyhydr)oxides in environmental systems is an essential C sequestration process (Amundson, 2001; Schmidt et al., 2011; Six et al., 2002); however, coprecipitation is also important.

The formation of Fe-OM complexes through sorption reactions has been studied extensively; however, Fe-OM complexes formed through coprecipitation are an equally important, less researched OC sequestration mechanism in environmental systems (Chen et al., 2014a; Chen et al., 2014b; Eusterhues et al., 2008; Lalonde et al., 2012). Fe-OM coprecipitation commonly occurs in the environment as a result of flux pH

and/or redox conditions (Chen et al., 2014b; Henneberry et al., 2012; Pokrovsky and Schott, 2002; Riedel et al., 2013). Recent research suggests that Fe-OM complexes formed through coprecipitation promotes higher OC sequestration extent than complexes formed through adsorption (Chen et al., 2014b). Also, coprecipitates have been observed to be of higher stability (approximately 10%) than adsorbed complexes during desorption experiments (Chen et al., 2014b; Chen et al., 2015). As both Fe-OM coprecipitates and adsorption complexes occur readily in environmental soil systems (Henneberry et al., 2012; Pokrovsky and Schott, 2002), a complete understanding of the biogeochemical processes controlling the formation of both complexes is needed to accurately predict environmental C cycling.

#### **1.4 Limited Investigation of Fe-Ca-OM Ternary Complexation**

Fe-OM sorption complexes and coprecipitates have been shown to have a large impact on C retention/stability; however, the importance of cations, such as  $\text{Ca}^{2+}$ , has been understudied (Kloster and Avena, 2015).  $\text{Ca}^{2+}$  likely forms a bridging complexes between environmental minerals and OM (Mikutta et al., 2007) but significant direct evidence of the occurrence and stability of these complexes in soil systems is lacking. Recent synchrotron-based techniques have found significant correlation of Ca and C in clay soil samples, of high Fe content, in the absence of carbonate minerals (Chen et al., 2014a). It has also been recently reported that Ca facilitated the sorption of humic acid,

a component of organic matter, to Fe(III) oxide minerals (Kloster and Avena, 2015). These results in conjunction with the known association of Fe and OM suggests that Ca may be an important factor determining OC stability that is in need of further investigation.

### **1.5 Natural Bacteriogenic Iron Oxides as a Reactive Sorbent**

Although abiotically synthesized ferrihydrite is often used as an experimental surrogate for short-ranged-ordered Fe(III) (oxyhydr)oxide minerals that are environmentally ubiquitous (Jambor and Dutrizac, 1998), there is a growing recognition that bacteriogenic Fe oxides (BIOs) are common in natural waters and sediments, forming specifically at redox gradients (e.g., circumneutral Fe(II)-rich groundwater discharges into quiescent aerobic surface water) (Duckworth et al., 2009; Emerson and Weiss, 2004; Ferris, 2005; Gault et al., 2011; Roden et al., 2012). BIOs typically have important structural differences (decreased crystallinity, reduced crystal domain size, and lower surface area) compared to synthetic ferrihydrite and have been observed to have unique affinity for metal cations and oxyanions of arsenic and chromium (Cismasu et al., 2011; Galbraith et al., 2002; Hohmann et al., 2009; Posth et al., 2010; Sowers et al., 2017; Whitaker et al., 2018; Whitaker and Duckworth, 2018). Cell-derived organic matter is incorporated into the BIO mineral and been shown to typically contain approximately 2 to 5 % OC (Hao et al., 2016;

Muehe et al., 2013; Schmid et al., 2014; Sowers et al., 2017); however, little is known concerning the nature of the OC present upon formation and how BIOs will influence the cycling of aqueous OC. Chan et al. performed soft X-ray spectroscopic analysis on BIOs to evaluate the chemical composition of morphologically different components of a BIOs sample (Chan et al., 2009). For stalk, sheath, and filament morphologies, C speciation for all were observed to consist of primarily carboxylic C, with a significant contribution of what was inferred to be extracellular polysaccharides. It is unknown how BIOs C speciation, or C to Fe ratios, will vary with BIOs synthesis location and age. Preliminary near-edge X-ray absorption fine structure (NEXAFS) spectroscopy by our group confirmed the presence of carboxylic C as the dominant OC species in BIOs. The sorptive capacity for additional OC, and the stability of OC associated with BIOs, is also unknown. OC is expected to sorb to BIOs due to high reactivity observed for oxyanions, which may impact how the C cycle is modeled in environmental systems.

## **1.6 Organo-mineral Associations of Permafrost Systems**

Permafrost soils contain vast stocks of OC (~1500 Pg), with 800 Pg OC perennially frozen, that are increasingly susceptible to microbial decomposition, emission to the atmosphere, and export to aquatic systems as permafrost regions warm (Hugelius et al., 2014). Recent studies suggest this substantial reservoir of C is easily

decomposable (Waldrop et al., 2010); however, the extent and rate of release is dependent on both the chemical composition of stored C (Drake et al., 2015) and geochemical stabilization mechanisms, such as complexation with highly-reactive iron (Fe)-bearing mineral surfaces (Gu et al., 1994; Lalonde et al., 2012; Schmidt et al., 2011). Formation of organo-mineral complexes in temperate and tropical soil systems, particularly with semi-crystalline Fe species, has been found to stabilize C over decadal to century timescales (Kaiser and Guggenberger, 2000; Sollins et al., 1996; Trumbore, 1993), but the mobility and sequestration mechanisms of these complexes in discontinuous permafrost soils, exposed to rapidly changing climatic conditions, remains unknown.

## **1.7 Knowledge Gaps and Motivation**

Investigations of organo-mineral interactions in soil and water systems are of current intense focus; however, there is currently a deficit of knowledge and investigations exploring the unique C chemistry of Fe oxides in biogeochemically unique terrestrial and aquatic systems. Therefore, we have conducted a series of projects that probe novel OM sorption mechanisms, biogenic sorbents, and climate-sensitive permafrost soils to provide new insight into Fe oxide organo-mineral interactions in the environment. This collection of research is expected to provide new explanations and revised estimations of C sequestration and stability by Fe oxides in terrestrial and

aquatic systems, which will inform climate change mitigation strategies and advance the current standing of terrestrial and aquatic nutrient cycling.

## **1.8 Research Questions and Hypotheses**

Research Question 1: What is the impact of calcium on the sequestration and stability of OC in Fe-(Ca-)OM adsorption complexes?

*Hypothesis 1: Calcium enhances the sorption extent and stability of OC through the formation of bridging structures between Fe and C.*

Research Question 2: Can Fe-Ca-OM ternary adsorption complexes form and what is the mechanism of adsorption, if so?

*Hypothesis 2: Fe-Ca-OM ternary complexes will form at circumneutral pH and will sorb primarily to DOM carboxylic acid groups.*

Research Question 3: What is the reactivity of BIOs for DOM and which OC moieties are preferentially sequestered?

*Hypothesis 3a: BIOs will sequester a similar quantity of OC compared to synthetic 2-line ferrihydrite.*

*Hypothesis 3b: OC sorbed to BIOs will have greater stability than OC sorbed to synthetic 2-line ferrihydrite.*

*Hypothesis 3c: Fe, Ca, and OC will be closely associated in BIOs samples.*

Research Question 4: How do Fe oxide and clay minerals affect the sequestration of OC across a thaw gradient of permafrost soils in Fairbanks, Alaska?

*Hypothesis 4: Fe will highly co-associate with OC species for all permafrost soils tested, which will dominantly consist of inner-sphere complexed carboxylic and aromatic moieties.*

## REFERENCES

- Amundson, R. (2001). The carbon budget in soils. *Annual Review of Earth and Planetary Sciences* **29**, 535-562.
- Chan, C. S., Fakra, S. C., Edwards, D. C., Emerson, D., and Banfield, J. F. (2009). Iron oxyhydroxide mineralization on microbial extracellular polysaccharides. *Geochimica et Cosmochimica Acta* **73**, 3807-3818.
- Chen, C., Dynes, J. J., Wang, J., Karunakaran, C., and Sparks, D. L. (2014a). Soft X-ray spectromicroscopy study of mineral-organic matter associations in pasture soil clay fractions. *Environmental science & technology* **48**, 6678-6686.
- Chen, C., Dynes, J. J., Wang, J., and Sparks, D. L. (2014b). Properties of Fe-organic matter associations via coprecipitation versus adsorption. *Environmental science & technology* **48**, 13751-13759.
- Chen, C., Kukkadapu, R., and Sparks, D. L. (2015). Influence of Coprecipitated Organic Matter on Fe<sup>2+</sup> (aq)-Catalyzed Transformation of Ferrihydrite: Implications for Carbon Dynamics. *Environmental science & technology* **49**, 10927-10936.
- Chorover, J., and Amistadi, M. K. (2001). Reaction of forest floor organic matter at goethite, birnessite and smectite surfaces. *Geochimica et Cosmochimica Acta* **65**, 95-109.
- Cismasu, A. C., Michel, F. M., Tcaciuc, A. P., Tyliczszak, T., and Brown Jr, G. E. (2011). Composition and structural aspects of naturally occurring ferrihydrite. *Comptes Rendus Geoscience* **343**, 210-218.
- Cornell, R. M., and Schwertmann, U. (2003). "The iron oxides: structure, properties, reactions, occurrences and uses," John Wiley & Sons.
- Cox, P. M., Betts, R. A., Jones, C. D., Spall, S. A., and Totterdell, I. J. (2000). Acceleration of global warming due to carbon-cycle feedbacks in a coupled climate model. *Nature* **408**, 184-187.

- Davidson, E. A., Trumbore, S. E., and Amundson, R. (2000). Biogeochemistry: soil warming and organic carbon content. *Nature* **408**, 789-790.
- Drake, T. W., Wickland, K. P., Spencer, R. G., McKnight, D. M., and Striegl, R. G. (2015). Ancient low-molecular-weight organic acids in permafrost fuel rapid carbon dioxide production upon thaw. *Proceedings of the National Academy of Sciences* **112**, 13946-13951.
- Duckworth, O. W., Holmström, S. J., Peña, J., and Sposito, G. (2009). Biogeochemistry of iron oxidation in a circumneutral freshwater habitat. *Chemical Geology* **260**, 149-158.
- Emerson, D., and Weiss, J. V. (2004). Bacterial iron oxidation in circumneutral freshwater habitats: findings from the field and the laboratory. *Geomicrobiology Journal* **21**, 405-414.
- Eusterhues, K., Wagner, F. E., Häusler, W., Hanzlik, M., Knicker, H., Totsche, K. U., Kögel-Knabner, I., and Schwertmann, U. (2008). Characterization of ferrihydrite-soil organic matter coprecipitates by X-ray diffraction and Mossbauer spectroscopy. *Environmental science & technology* **42**, 7891-7897.
- Feng, X., Simpson, A. J., and Simpson, M. J. (2005). Chemical and mineralogical controls on humic acid sorption to clay mineral surfaces. *Organic Geochemistry* **36**, 1553-1566.
- Ferris, F. G. (2005). Biogeochemical Properties of Bacteriogenic Iron Oxides. *Geomicrobiology Journal* **22**, 79-85.
- Galbraith, H., Jones, R., Park, R., Clough, J., Herrod-Julius, S., Harrington, B., and Page, G. (2002). Global climate change and sea level rise: potential losses of intertidal habitat for shorebirds. *Waterbirds* **25**, 173-183.
- Gault, A. G., Ibrahim, A., Langley, S., Renaud, R., Takahashi, Y., Boothman, C., Lloyd, J. R., Clark, I. D., Ferris, F. G., and Fortin, D. (2011). Microbial and geochemical features suggest iron redox cycling within bacteriogenic iron oxide-rich sediments. *Chemical Geology* **281**, 41-51.
- Gu, B., Schmitt, J., Chen, Z., Liang, L., and McCarthy, J. F. (1994). Adsorption and desorption of natural organic matter on iron oxide: mechanisms and models. *Environmental Science & Technology* **28**, 38-46.

- Gu, B., Schmitt, J., Chen, Z., Liang, L., and McCarthy, J. F. (1995). Adsorption and desorption of different organic matter fractions on iron oxide. *Geochimica et Cosmochimica Acta* **59**, 219-229.
- Hao, L., Guo, Y., Byrne, J. M., Zeitvogel, F., Schmid, G., Ingino, P., Li, J., Neu, T. R., Swanner, E. D., and Kappler, A. (2016). Binding of heavy metal ions in aggregates of microbial cells, EPS and biogenic iron minerals measured in-situ using metal-and glycoconjugates-specific fluorophores. *Geochimica et Cosmochimica Acta* **180**, 66-96.
- Henneberry, Y. K., Kraus, T. E., Nico, P. S., and Horwath, W. R. (2012). Structural stability of coprecipitated natural organic matter and ferric iron under reducing conditions. *Organic geochemistry* **48**, 81-89.
- Hohmann, C., Winkler, E., Morin, G., and Kappler, A. (2009). Anaerobic Fe (II)-oxidizing bacteria show As resistance and immobilize As during Fe (III) mineral precipitation. *Environmental science & technology* **44**, 94-101.
- Hugelius, G., Strauss, J., Zubrzycki, S., Harden, J. W., Schuur, E., Ping, C.-L., Schirmer, L., Grosse, G., Michaelson, G. J., and Koven, C. D. (2014). Estimated stocks of circumpolar permafrost carbon with quantified uncertainty ranges and identified data gaps. *Biogeosciences (Online)* **11**.
- Jambor, J. L., and Dutrizac, J. E. (1998). Occurrence and constitution of natural and synthetic ferrihydrite, a widespread iron oxyhydroxide. *Chemical Reviews* **98**, 2549-2586.
- Kaiser, K., and Guggenberger, G. (2000). The role of DOM sorption to mineral surfaces in the preservation of organic matter in soils. *Organic geochemistry* **31**, 711-725.
- Kaiser, K., and Guggenberger, G. (2003). Mineral surfaces and soil organic matter. *European Journal of Soil Science* **54**, 219-236.
- Kleypas, J. A., Buddemeier, R. W., Archer, D., Gattuso, J.-P., Langdon, C., and Opdyke, B. N. (1999). Geochemical consequences of increased atmospheric carbon dioxide on coral reefs. *science* **284**, 118-120.
- Kloster, N., and Avena, M. (2015). Interaction of humic acids with soil minerals: adsorption and surface aggregation induced by Ca<sup>2+</sup>. *Environmental Chemistry* **12**, 731-738.

- Lal, R. (2004). Soil carbon sequestration impacts on global climate change and food security. *science* **304**, 1623-1627.
- Lalonde, K., Mucci, A., Ouellet, A., and G elinas, Y. (2012). Preservation of organic matter in sediments promoted by iron. *Nature* **483**, 198-200.
- Mann, L. (1986). Changes in soil carbon storage after cultivation. *Soil Science* **142**, 279-288.
- Meehl, G. A., Stocker, T. F., Collins, W. D., Friedlingstein, P., Gaye, A. T., Gregory, J. M., Kitoh, A., Knutti, R., Murphy, J. M., and Noda, A. (2007). Global climate projections. *Climate change* **3495**, 747-845.
- Michel, F. M., Ehm, L., Antao, S. M., Lee, P. L., Chupas, P. J., Liu, G., Strongin, D. R., Schoonen, M. A., Phillips, B. L., and Parise, J. B. (2007). The structure of ferrihydrite, a nanocrystalline material. *Science* **316**, 1726-1729.
- Mikutta, R., Mikutta, C., Kalbitz, K., Scheel, T., Kaiser, K., and Jahn, R. (2007). Biodegradation of forest floor organic matter bound to minerals via different binding mechanisms. *Geochimica et Cosmochimica Acta* **71**, 2569-2590.
- Muehe, E. M., Scheer, L., Daus, B., and Kappler, A. (2013). Fate of Arsenic during Microbial Reduction of Biogenic versus Abiogenic As-Fe(III)-Mineral Coprecipitates. *Environmental Science & Technology* **47**, 8297-8307.
- Pokrovsky, O., and Schott, J. (2002). Iron colloids/organic matter associated transport of major and trace elements in small boreal rivers and their estuaries (NW Russia). *Chemical Geology* **190**, 141-179.
- Post, W. M., and Kwon, K. C. (2000). Soil carbon sequestration and land use change: processes and potential. *Global change biology* **6**, 317-327.
- Posth, N. R., Huelin, S., Konhauser, K. O., and Kappler, A. (2010). Size, density and composition of cell-mineral aggregates formed during anoxygenic phototrophic Fe(II) oxidation: Impact on modern and ancient environments. *Geochimica et Cosmochimica Acta* **74**, 3476-3493.
- Riedel, T., Zak, D., Biester, H., and Dittmar, T. (2013). Iron traps terrestrially derived dissolved organic matter at redox interfaces. *Proceedings of the National Academy of Sciences* **110**, 10101-10105.

- Riley, W., Maggi, F., Kleber, M., Torn, M., Tang, J., Dwivedi, D., and Guerry, N. (2014). Long residence times of rapidly decomposable soil organic matter: application of a multi-phase, multi-component, and vertically resolved model (BAMS1) to soil carbon dynamics.
- Roden, E. E., McBeth, J. M., Blöthe, M., Percak-Dennett, E. M., Fleming, E. J., Holyoke, R. R., Luther III, G. W., Emerson, D., and Schieber, J. (2012). The microbial ferrous wheel in a neutral pH groundwater seep. *The microbial ferrous wheel: iron cycling in terrestrial, freshwater, and marine environments*, 199.
- Schlesinger, W. H. (1986). Changes in soil carbon storage and associated properties with disturbance and recovery. In "The Changing Carbon Cycle", pp. 194-220. Springer.
- Schmid, G., Zeitvogel, F., Hao, L., Ingino, P., Floetenmeyer, M., Stierhof, Y. D., Schroepel, B., Burkhardt, C., Kappler, A., and Obst, M. (2014). 3D analysis of bacterial cell(iron) mineral aggregates formed during Fe (II) oxidation by the nitrate-reducing *Acidovorax* sp. strain BoFeN1 using complementary microscopy tomography approaches. *Geobiology* **12**, 340-361.
- Schmidt, M. W., Torn, M. S., Abiven, S., Dittmar, T., Guggenberger, G., Janssens, I. A., Kleber, M., Kögel-Knabner, I., Lehmann, J., and Manning, D. A. (2011). Persistence of soil organic matter as an ecosystem property. *Nature* **478**, 49-56.
- Schneider, M., Scheel, T., Mikutta, R., Van Hees, P., Kaiser, K., and Kalbitz, K. (2010). Sorptive stabilization of organic matter by amorphous Al hydroxide. *Geochimica et Cosmochimica Acta* **74**, 1606-1619.
- Shaker, A. M., Komy, Z. R., Heggy, S. E., and El-Sayed, M. E. (2012). Kinetic study for adsorption humic acid on soil minerals. *The Journal of Physical Chemistry A* **116**, 10889-10896.
- Six, J., Conant, R., Paul, E. A., and Paustian, K. (2002). Stabilization mechanisms of soil organic matter: implications for C-saturation of soils. *Plant and soil* **241**, 155-176.
- Sollins, P., Homann, P., and Caldwell, B. A. (1996). Stabilization and destabilization of soil organic matter: mechanisms and controls. *Geoderma* **74**, 65-105.

- Solomon, S., Plattner, G.-K., Knutti, R., and Friedlingstein, P. (2009). Irreversible climate change due to carbon dioxide emissions. *Proceedings of the national academy of sciences*, pnas. 0812721106.
- Sowers, T. D., Harrington, J. M., Polizzotto, M. L., and Duckworth, O. W. (2017). Sorption of arsenic to biogenic iron (oxyhydr) oxides produced in circumneutral environments. *Geochimica et Cosmochimica Acta* **198**, 194-207.
- Sparks, D. L. (2003a). "Environmental soil chemistry," Academic press.
- Sparks, D. L. (2003b). Environmental soil chemistry.
- Trumbore, S. E. (1993). Comparison of carbon dynamics in tropical and temperate soils using radiocarbon measurements. *Global Biogeochemical Cycles* **7**, 275-290.
- von Lützow, M., and Kögel-Knabner, I. (2009). Temperature sensitivity of soil organic matter decomposition—what do we know? *Biology and Fertility of Soils* **46**, 1-15.
- von Lützow, M., Kögel-Knabner, I., Ludwig, B., Matzner, E., Flessa, H., Ekschmitt, K., Guggenberger, G., Marschner, B., and Kalbitz, K. (2008). Stabilization mechanisms of organic matter in four temperate soils: Development and application of a conceptual model. *Journal of Plant Nutrition and Soil Science* **171**, 111-124.
- Wagai, R., and Mayer, L. M. (2007). Sorptive stabilization of organic matter in soils by hydrous iron oxides. *Geochimica et Cosmochimica Acta* **71**, 25-35.
- Waldrop, M. P., Wickland, K. P., White Iii, R., Berhe, A. A., Harden, J. W., and Romanovsky, V. E. (2010). Molecular investigations into a globally important carbon pool: Permafrost-protected carbon in Alaskan soils. *Global change biology* **16**, 2543-2554.
- Waychunas, G., Rea, B., Fuller, C., and Davis, J. (1993). Surface chemistry of ferrihydrite: Part 1. EXAFS studies of the geometry of coprecipitated and adsorbed arsenate. *Geochimica et Cosmochimica Acta* **57**, 2251-2269.
- Whitaker, A. H., Amor, M., Pena, J., and Duckworth, O. W. (2018). Cr (VI) Uptake and Reduction by Biogenic Iron (Oxyhydr) oxides. *Environmental Science: Processes & Impacts*.

Whitaker, A. H., and Duckworth, O. W. (2018). Cu, Pb, and Zn Sorption to Biogenic Iron (Oxyhydr) Oxides Formed in Circumneutral Environments. *Soil Systems* **2**, 18.

## Chapter 2

### PROBING THE OCCURRENCE AND ORGANO-MINERAL ASSOCIATIONS OF IRON, CALCIUM, AND ORGANIC MATTER TERNARY COMPLEXES

#### 2.1 Introduction

Metal oxides immobilize OC in soils by forming protective sorption complexes with OM (Gu et al., 1995; Kaiser and Guggenberger, 2000; Lalonde et al., 2012; Mikutta et al., 2007; Shaker et al., 2012; Wagai and Mayer, 2007). Iron, Mn, and Al oxide minerals are primary OM-stabilizing soil constituents (Gu et al., 1994; Mikutta et al., 2007; Schneider et al., 2010; Wagai and Mayer, 2007); however, Fe(III) oxide minerals are of particular environmental importance. Compared to Mn and Al oxides, Fe(III) oxides may sequester OM to a higher extent and may provide increased stability of sorbed OM (Cismasu et al., 2012; Cornell and Schwertmann, 2003; Jambor and Dutrizac, 1998; Kalbitz et al., 2000; Stuckey et al., 2018; Tessier et al., 1996). Although phyllosilicates also sequester OM, the degree of sorption is lower than that of Fe(III) oxide minerals by approximately an order of magnitude (Chorover and Amistadi, 2001). Short-range-ordered Fe(III) mineral phases, such as 2-line ferrihydrite, are of primary importance as these phases have the highest surface area and reactivity compared to more crystalline phases (Cornell and Schwertmann, 2003;

Michel et al., 2007; Waychunas et al., 1993). Also, sorption of dissolved OC to 2-line ferrihydrite has been found to be resistant to desorption (Chen et al., 2014b; Gu et al., 1995; Kaiser and Guggenberger, 2000). The binding mechanism facilitating OM sorption to Fe(III) oxides has long been investigated using a variety of spectroscopic methods including attenuated total reflectance-Fourier transform infrared spectroscopy (ATR-FTIR), diffuse reflectance infrared Fourier transform spectroscopy (DRIFT), X-ray photoelectron spectroscopy (XPS), and X-ray absorption spectroscopy (XAS) (Kleber et al., 2015). Many of these studies suggest the sorption of OM to Fe(III) metal oxides occurs through a ligand exchange mechanism with the potential for additional outer-sphere complexation varying based on solution pH and ionic strength (Feng et al., 2005; Gu et al., 1994; Kleber et al., 2015). Ligand exchange occurs primarily through exchange of OC carboxyl functional moieties with hydroxyl groups (Chen et al., 2014a; Chen et al., 2014b; Post and Kwon, 2000). Aromatic groups are associated with Fe, though potentially through carboxyl attachment to aromatic rings (Chen et al., 2014b; Kleber et al., 2015). However, the mechanism of OM sorption to metal oxides is still an area of intense research due to wide-ranging results concerning the reactivity of soil sorbents, arising from the complexity of OM and technical difficulty in analyzing mechanisms dictating OC sequestration. Therefore, there is a need for further exploration of the organo-mineral associations controlling environmental C cycling. An important step forward in improving the current soil C

cycling knowledgebase is to investigate the cycling of OM in chemically complex ternary systems.

Much of the current understanding of OM sequestration in environmental systems has focused solely on binary systems of OC and Fe (Chen et al., 2014b; Wagai and Mayer, 2007); however, the prevalence of divalent cations such as calcium (Ca) and magnesium (Mg) may affect the environmental cycling of C via ternary complex formation. The formation of bridging complexes between metal oxides and OM has been briefly discussed in the literature (Mikutta et al., 2007) but significant evidence of the occurrence and sorption behavior of these complexes in environmental systems is scarce. Recent research on ternary complex formation in systems containing Fe oxides have been found to play a role in arsenate and phosphate sequestration. Antelo et al. found increasing Ca concentration in ferrihydrite and arsenate/phosphate systems resulted in increased arsenate/phosphate sequestration at  $\text{pH} \geq 8$  along with a corresponding decrease in aqueous Ca concentration (Antelo et al., 2015). The results observed in this study provide a promising analogue to research probing the sequestration of OM as Fe-Ca-OM ternary complexes. Weng et al., for example, suggests that OC sorption to metal oxides may exhibit behavior similar to polyvalent ions such as phosphate (Weng et al., 2005), which implies that potential ternary complexation behavior for ferrihydrite, Ca, and OM may occur similarly to reported ferrihydrite, Ca, and phosphate ternary complexes (Antelo et al., 2015). Preliminary

evidence exists for the presence of Ca associations with Fe and OM in environmental systems. The use of synchrotron-based scanning transmission X-ray microscopy (STXM) has shown significant correlation between Ca and C in the clay fraction of soils that contain high Fe content but are absent of detectable carbonate minerals (Chen et al., 2014a). Additionally, humic acid sorption to Fe(III) minerals has been found to be promoted by the presence of Ca (Kloster and Avena, 2015; Kloster et al., 2013). These results, in conjunction with the known association of Fe and OM, suggest that Ca may be an important factor determining OM sequestration and is in need of further investigation.

Research probing the mechanism and sequestration extent of OC sequestration to Fe oxide is needed to reliably model C cycling in environmental systems. Examining the effect of polyvalent ions such as Ca on OM sequestration could have major impacts on how OM cycling is modeled in natural systems and could have implications on the sorption of (in)organic contaminants by Fe(III) oxides (Kleber et al., 2015; Redman et al., 2002). To explore the effect of Ca on OM sorption to Fe(III) oxides, we (1) assessed the impact of Ca on the sorption of dissolved organic matter (DOM) or citric acid to 2-line ferrihydrite, (2) determined spatially correlated Fe, Ca, and C relationships for ferrihydrite samples loaded with DOM or citric acid in the presence or absence of Ca, (3) compared C 1s NEXAFS spectra at localized clusters identified via principal component analysis (PCA) for complexes synthesized in the

presence or absence of Ca, and (4) probed changes in sorbed C speciation and sorption mechanism in the presence or absence of Ca using C 1s NEXAFS and ATR-FTIR spectroscopy.

## **2.2 Materials and Methods**

### **2.2.1 Natural and Laboratory Sources of OM**

Both natural and model (citric acid) organic carbon sources were tested to determine the effect of Ca on OM sorption to synthetic 2-line ferrihydrite. Water-extractable dissolved organic matter (DOM) was used as a natural source of OM. Leaf litter used for the DOM extraction was obtained from the Stroud Water Research Center (Avondale, PA). Samples were collected from the top 10 cm of leaf litter from a forest soil O<sub>a</sub> horizon (Typic Hapludult). Using a method adapted from Chen et al. and Stuckey et al. (Chen et al., 2014b; Stuckey et al., 2018), soil-organic materials were mixed with DI water for 90 hours (1:2 fresh leaf litter:DI water [w/w]) while being vigorously stirred (200 rpm) on a rotary shaker. After a 90-hour equilibration time, the resulting solution was centrifuged (20,000 g for one hour) and sequentially vacuum filtered through polyethersulfone filters of 0.8 μm, 0.45 μm, and 0.2 μm pore size. Sequential filtration was performed due to the large range in particle size of the leaf litter extract. The filtered DI-extractable DOM solution was then analyzed using a

Total Organic Carbon (TOC) analyzer (Apollo 9000 series) to determine OC concentration (Table 2.1). A metal/metalloid elemental analysis of the DOM solution was performed using inductively coupled plasma- atomic emission (ICP-AES) (Table 2.2). Citric acid was chosen as a model OC compound analogue for our study. Citric acid (Sigma Aldrich) is a tricarboxylic acid and was chosen due to the high reactivity of the carboxylic acid moiety, high concentration of carboxylic acid from DOM extracted from the same leaf litter site (Chen et al., 2014b), and the favorable sorption of carboxylic acid to iron oxides (Gu et al., 1994; Wagai and Mayer, 2007). Attenuated total reflectance-Fourier transform infrared spectroscopy (ATR-FTIR) analysis of the DOM (Table 2.3) confirmed that carboxylic acid is the dominant C moiety present (assignment), with aromatic ( $1585\text{ cm}^{-1}$ ), phenolic ( $1270\text{ cm}^{-1}$ ), and polysaccharide ( $1120$ ,  $1080$ , and  $1040\text{ cm}^{-1}$ ) groups present to a lesser degree.

### **2.2.2 Synthetic 2-line Ferrihydrite Synthesis**

Two-line ferrihydrite, a ubiquitously found Fe(III) oxide, was synthesized according to procedures established in Cornell and Schwertmann (23). 40 g of  $\text{Fe}(\text{NO}_3)_3 \cdot 9\text{H}_2\text{O}$  was dissolved in 500 mL of deionized (DI) water. In order to bring the pH to a range of 7-8, 330 mL of 1 M KOH was added, while stirring, to a  $\text{Fe}(\text{NO}_3)_3 \cdot 9\text{H}_2\text{O}$  solution. The pH of the solution was continuously monitored during

the addition of the final 20 mL of 1 M KOH. Upon reaching this pH range, the solution was centrifuged and dialyzed, yielding 10 g of 2-line ferrihydrite.

### **2.2.3 Sorption Isotherms**

Multiple adsorption isotherm experiments were performed to test the effect of increasing OC concentration and/or increasing Ca concentration on OM sorption to synthetic 2-line ferrihydrite. The previously discussed DOM stock was used as a source of OM for all adsorption experiments. Prior to beginning sorption experiments, the DOM stock was determined to have an OC concentration of approximately 2028 mg OC L<sup>-1</sup> and a Ca concentration of approximately 4 mM Ca. Each reactor received 43 mg of 2-line ferrihydrite as a wet paste and was suspended with 40 mL of DOM stock diluted with Type 1 deionized (DI) water to achieve a series of initial OC concentrations, such that the C/Fe molar ratio ranged from 0.3 to 16.9. Initial Ca concentration increased as initial DOM concentration increased due to the inherent Ca concentration present in the DOM stock, resulting in Ca concentration increasing up to 4 mM Ca for the most concentrated DOM sample (initial C/Fe molar ratio of 16.9). The pH of the suspensions was adjusted to  $6.25 \pm 0.10$  using NaOH and/or HCl in order to perform reactions at an environmentally relevant pH. All samples were covered and mixed via a rotary shaker (50 rpm) in the dark for 24 hours after pH adjustment. The 24-hour equilibration time was determined by performing preliminary

sorption experiments, in which maximum OC sorption was reached within 24 hours. Sample pH was monitored intermittently throughout the equilibration time to ensure that the pH remained at  $6.25 \pm 0.10$ . Upon completion of the 24-hour equilibration, samples were centrifuged (20,000 g) and the supernatant was collected for TOC and ICP-AES analysis. Solid samples were washed at least twice with DI water and stored moist in a freezer at approximately  $-4^{\circ}\text{C}$  until further analysis. Analogous control experiments were performed with citric acid as the C source rather than natural DOM. All sorption isotherm experiments here and throughout were performed in at least duplicate.

For the next series of sorption isotherm experiments, the previously detailed procedure was repeated, except  $\text{CaCl}_2$  was added to each reactor such that the final Ca concentration was equal to the Ca concentration of the sample receiving the greatest concentration of DOM solution ( $\sim 4$  mM Ca). For citric acid experiments, which contain no native Ca concentration,  $\text{CaCl}_2$  was added to match the Ca concentration of the DOM experiments. Lastly, separate sorption isotherms testing the effect of increasing Ca concentrations were performed for C/Fe molar ratios of 4.7 and 12.5. Calcium chloride was added to each sample such that the initial Ca concentration ranged from approximately 1 mM Ca to 60 mM Ca. All other steps were carried out as described for the 4 mM Ca sorption experiments. Prior to performing experiments with increasing Ca concentration, a subsample of stock DOM solution was

equilibrated with 100 mM Ca (via  $\text{CaCl}_2$ ) to ensure no precipitates formed. No precipitates were formed after shaking for a 24-hour equilibration time.

TOC analysis was performed before and after sorption of DOM to 2-line ferrihydrite for all experiments. The quantity of OC sorbed was calculated by measuring the difference between the OC concentrations before and after sorption. Sorption isotherm data were processed and fit to the Langmuir equation using a preprogrammed Excel sheet (Bolster and Hornberger, 2007).

#### **2.2.4 Sorption Envelopes**

The effect of pH and Ca concentration at an initial C/Fe molar ratio of 4.7 was determined by conducting sorption envelope experiments with DOM and 2-line ferrihydrite. The experimental setup was equivalent to what was performed for sorption isotherm reactions discussed previously; however, initial OC concentration was consistent across all samples and pH was the singular variable being changed. All samples contained 43 mg of 2-line ferrihydrite and were suspended in the DOM stock solution such that the initial C/Fe molar ratio equaled 4.7. Subsequently, sample pH was adjusted with HCl and NaOH (accounted for <1% of total solution volume) from pH 4 to 9. All envelope experiments were then shaken in the dark for 24 hours and then sampled according to the sorption isotherm procedure discussed earlier. Separate envelope experiments were performed at different Ca concentrations (via  $\text{CaCl}_2$

addition), which consisted of approximately 1 (background DOM concentration), 10, or 30 mM Ca in order to capture typical behavior at high soil porewater Ca concentrations (Antelo et al., 2015; Lock et al., 2007). Control sorption envelope experiments were performed with only Ca and 2-line ferrihydrite to evaluate Ca sorption to ferrihydrite without DOM. Aqueous and solid samples from the sorption envelope experiments were collected after 24 hours of reaction time and analyzed similarly to what was described earlier for sorption isotherm experiments. Before beginning envelope experiments, subsamples of DOM stock were adjusted from pH 4 to 9 to determine if any precipitates formed. No precipitates were observed after 24 hours.

### **2.2.5 Scanning Transmission X-ray Microscopy**

STXM-NEXAFS data was collected at beamline 10ID-1 at the Canadian Light Source (Saskatoon, Saskatchewan) for all DOM-bearing and citric acid-bearing sample synthesized earlier at initial C/Fe molar ratios of 4.7. A subsample of ferrihydrite wet-paste was suspended in DI water such that approximately 0.5 mg of sample was suspended with 1 mL DI water (Chen et al., 2014a; Chen et al., 2014b). Approximately 3  $\mu$ L of the well-mixed suspension was applied to a Si<sub>3</sub>N<sub>4</sub> window such that the window was covered. Prior to analysis, the sample was allowed to air-dry for approximately 30 minutes and then placed on the STXM sample holder. The

STXM chamber was pumped to rough vacuum and then backfilled with 1/6 atmosphere He for the measurements. A maximum spatial resolution of approximately 30 nm was achieved using a Fresnel zone plate. Dwell time equaled 1 ms with a pixel size of approximately 40 nm for all measurements taken.

C 1s, Ca 2p, and Fe 2p data was obtained by raster scanning from 280 to 735 eV at specific regions of interest identified at low magnification (up to approximately 2500  $\mu\text{m}^2$ ) at the C K-edge (288 eV). Image stacks were generated for each element across the aforementioned eV range and averages of these stacks at specific eV ranges were then used when processing collected STXM-NEXAFS data.

#### **2.2.6 Processing of STXM-NEXAFS Data**

All data stacks were aligned using Stack Analyze (Stony Brook, V2.7) and processed using the aXis2000 software package (Hitchcock; Jacobsen et al., 2000). PCA and cluster analysis was performed using PCA GUI 1.1.1 software (Lerotic et al., 2005). After alignment and identifying  $I_0$  (incident flux), aXis2000 was used to convert aligned and stacked image data to optical density using the following equation:  $OD = \ln(I_0/I)$ , where  $I$  is equal to the flux transmitted through the sample. Generated images up to  $\pm 0.5$  eV of the resonance energy for each element were averaged for chemical mapping. The averaged images at each element's resonance

energies were subtracted with averaged images at the elements' specific pre-edge range (Table 2.4) in order to obtain chemical maps.

Optical density is correlated to element thickness (Lambert-Beer's law) and was calculated for all elements analyzed (Table 2.4 and 2.5). Thickness estimates were made using methods described in Wan et al. (2007) and Chen et al. (2014a) For C, the product of  $RE \cdot \mu \cdot f \cdot \rho$  was used to calculate the conversion factor for optical density to C thickness (Table 5). RE is a dimensionless resonance enhancement factor,  $\mu$  ( $\text{cm}^2 \text{g}^{-1}$ ) is the mass absorption coefficient above the C absorption edge minus the mass absorption coefficient below the C edge,  $f$  ( $\text{g g}^{-1}$ ) is the fraction of C in the solid phase (mass basis), and  $\rho$  ( $\text{g cm}^{-3}$ ) is the density of the solid phase (Table 2.5) (Wan et al., 2007).  $f$  and  $\rho$  were calculated using values published in Stevenson et al. (1994) Scaling factors for Ca and Fe were taken from Chen et al. (Chen et al., 2014a) and used for optical density to thickness conversions in our study. Optical density correlations between elements were obtained by aligning optical density maps for each element (images averaged from the edge energy stack range minus corresponding images averaged from the pre-edge energy stack range, Table 2.4) and then comparing the maps on a per pixel basis.

PCA and cluster analysis were performed to identify regions of statistically unique spectra. Three to four components were typically used when searching for significant components and then lowered if significant features between two

components were congruent. An eigenimage scaling factor of 0.3 was used for all cluster analyses and singular value decomposition was performed when analyzing cluster spectra.

### **2.2.7 ATR-FTIR Spectroscopy**

Freeze-dried DOM and ferrihydrite samples were analyzed using a Bruker ATR-FTIR. Spectra were scanned from 4000 to 600  $\text{cm}^{-1}$  at a spectra resolution of 2  $\text{cm}^{-1}$ . 2-line ferrihydrite spectra was subtracted from all OC-bearing ferrihydrite samples to remove contributions from ferrihydrite and focus on the chemical composition of the bound OC. Automatic baseline correction and normalization was applied to all spectra. All samples were dried and analyzed soon after to avoid the effects of moisture uptake on sample spectra. The OPUS Version 7.2 spectroscopy software suite (Bruker) was used to process all collected spectra.

## **2.3 Results and Discussion**

### **2.3.1 Effect of Ca on the on DOM and Citric Acid Sorption to Ferrihydrite**

All isotherm data was well described by the Langmuir equation with OC sorbed concentrations increasing rapidly at low solution OC concentrations, with decreasing slope at high equilibrium concentrations (Figure 2.1, Table 2.6). This sorption phenomenon is consistent with the L-type isotherm; therefore, the Langmuir

equation was chosen over the Freundlich to fit all sorption isotherm data as the Langmuir equation was found to have a superior goodness of fit (Sparks, 2003; Sposito, 2008). All Langmuir fitting parameters ( $S = (S_{max}KC)/(1 + KC)$  where  $S$  is the sorbed concentration,  $S_{max}$  is the predicted maximum sorbed concentration,  $K$  is a sorption constant, and  $C$  is the equilibrium sorbate concentration) are shown in Table 2.6.

In Figure 2.1A, DOM sorption to 2-line ferrihydrite data was fit using the Langmuir equation with a high model efficiency for the data sets with and without Ca control (0.978 and 0.989, respectively). The Langmuir parameters for the non-Ca controlled and Ca controlled data sets were similar. Two differing sets of isotherms, one where DOM was reacted with 2-line ferrihydrite without the addition of  $\text{CaCl}_2$  and the other where  $\text{CaCl}_2$  was added such that Ca concentration was constant across all initial C/Fe concentrations, were performed to determine the effect of Ca control on DOM sorption on 2-line ferrihydrite. The maximum sorbed OC concentration for both data sets was observed to be 23.13 mmol OC  $\text{g}^{-1}$  ferrihydrite for the most concentrated DOM sample (initial C/Fe molar ratio of 16.9). The observed sorption maximum is mostly consistent with what Chen et al. observed at pH 7, although our experiments resulted in approximately 10% higher sorption relative to a system without exogenous calcium (Chen et al., 2014b). Although the Langmuir fitting parameters for the data sets were similar, the sorbed OC concentration from 25 to 75 mM equilibrium OC for

the Ca controlled isotherm was found to differ by approximately 10% to 15%. The difference in sorption at the 25 to 75 mM equilibrium OC concentration range was attributed to differences in Ca concentration (~1 mM Ca for non-Ca controlled isotherm samples versus ~4 mM Ca for Ca-controlled isotherm samples) (Figure 2.1).

Analogous sorption isotherm experiments, with and without fixed Ca concentration, were conducted using citric acid as an OC source. The sorption extent of citric acid to 2-line ferrihydrite was significantly less than that of DOM ( $S_{\max} = 11.32 \text{ mmol OC g}^{-1} \text{ ferrihydrite}$ ). The decreased affinity of citric acid to iron oxides compared to natural DOM is supported by the literature, although the observed sorption maximum for citric acid experiments was approximately an order of magnitude greater than that of citric acid sorption to goethite experiments (Lackovic et al., 2003). The lesser reactivity and surface area of goethite compared to 2-line ferrihydrite is the most likely reason for the observed disparity in sorption maximum. Unlike what was observed for DOM experiments, no significant differences in sorption extent were observed between data sets of no Ca addition and 4 mM Ca addition. These results suggest that Ca does not have an effect on the sorption of OC as citric acid to 2-line ferrihydrite. The DOM source has been found to consist of predominately carboxylic functional moieties through ATR-FTIR (Figure 2.12) and past studies (Chen et al., 2014b); therefore, it is surprising that citric acid sorption behavior differs from DOM. Chemical heterogeneity of natural DOM compared to a

simple model compound such as citric acid is a probable reason for the observed difference and suggests that citric acid may not be a representative analogue when modeling OC cycling in natural systems.

### **2.3.2 Effect of pH and Ca Concentration on DOM Sorption**

Sorption envelope experiments were performed to determine the concentration of sorbed OC, as DOM, to 2-line ferrihydrite from pH 4-9 at differing initial Ca concentrations (Figure 2.2). An initial C/Fe molar ratio of 4.7 was used for all sorption envelope experiments and zero Ca (native concentration of ~1 mM Ca from DOM), 10 mM Ca, or 30 mM Ca were added. The sorption data for the zero added Ca treatment decreased from a maximum of  $13.03 \pm 0.12$  mmol OC g<sup>-1</sup> 2-line ferrihydrite as pH increased, with a major decrease near the 2-line ferrihydrite point of zero charge (PZC = ~7.5) (Cornell and Schwertmann, 2003). The lowest sorbed OC concentration was found to be  $8.72 \pm 0.16$  mmol OC g<sup>-1</sup> 2-line ferrihydrite at pH 9. The decrease in sorbed OC concentration is best explained by the effects of pH on the variable charge of 2-line ferrihydrite. The 2-line ferrihydrite mineral surface should become less positively charged with increasing pH until the PZC is reached, after which the mineral surface becomes increasingly negatively charged (Cornell and Schwertmann, 2003; Sparks, 2003; Sposito, 2008). However, the addition of Ca to the system resulted in major differences in sorbed OC concentration, especially at pH > PZC.

The addition of  $\geq 10$  mM Ca simultaneously with DOM to the 2-line ferrihydrite system resulted in increased sorbed OC concentration across all tested pHs. The 10 mM Ca treatment resulted in approximately 2 mmol OC g<sup>-1</sup> 2-line ferrihydrite more sorption from pH 4 through 7 compared to the data set with no Ca treatment. The 30 mM Ca treatment resulted in similar sorbed OC concentration compared to the 10 mM Ca treatment from pH 4 through 7, with approximately 0.5 mmol OC g<sup>-1</sup> 2-line ferrihydrite increased sorption at pH 6 and 7. At pH  $\geq 7$  however, all sorbed OC concentration data significantly differed between data sets. Sorbed OC concentration differed greatest between sets at pH 9, with observed OC sorbed concentrations of  $8.72 \pm 0.16$ ,  $11.05 \pm 0.19$ , and  $13.3 \pm 0.20$  mmol OC g<sup>-1</sup> 2-line ferrihydrite for the no Ca, 10 mM Ca, and 30 mM Ca treatments, respectively. Another important feature in Figure 2.2 is that the 30 mM Ca data set was found to vary only slightly across the pH 5-9 range. Sorbed OC concentration of samples at pH 4 and 5 varied by approximately  $0.6 \pm 0.2$  mmol OC g<sup>-1</sup> 2-line ferrihydrite, whereas samples at pH 7-9 varied by only approximately  $0.15 \pm 0.044$  mmol OC g<sup>-1</sup> 2-line ferrihydrite.

The higher sorption of OC with Ca addition and the lower variation in sorbed OC from pH 5-9 for the 30 mM Ca data set suggests that Ca enhances sequestration of OC to 2-line ferrihydrite. Trends similar to those observed in Figure 2.2 were observed in systems studying the effect of initial Ca concentration on phosphate/arsenate

sorption to 2-line ferrihydrite (Antelo et al., 2015). Antelo et al. observed high disparity in phosphate sorption concentration at  $\text{pH} \geq 7$  with increasing Ca concentration, the same trend observed in our study for OC sorption concentration (Antelo et al., 2015). Also, the rate of phosphate sorption decrease declined dramatically with increasing pH at 6 mM Ca; therefore, the effect of Ca on phosphate sorption to ferrihydrite appears to be similar to the ferrihydrite-Ca-OM system. The similarity in behavior between phosphate and OM sorption to Fe oxide has been shown in prior research as well (Weng et al., 2005), suggesting that ferrihydrite-Ca-phosphate systems may be an appropriate analogue when examining ferrihydrite-Ca-OM systems. The most likely explanation for the observed synergistic effect of Ca on OM sorption is due to the potential formation of Ca-bridging between ferrihydrite and OC. The high concentration of a divalent cation such as  $\text{Ca}^{2+}$  in a system containing negatively charged DOM and ferrihydrite surfaces at  $\text{pH} \geq 7$  may facilitate the bridging process and would explain the consistent OC sorption concentration from pH 5-9 of the 30 mM Ca data set. It was unexpected that OC sorption concentration would be affected by Ca concentration at pH 4 and 5 due to the system being electrostatically unfavorable for the formation of outer sphere complexes, making ligand exchange processes a likely controlling mechanism by which Ca effects OM sorption.

### 2.3.3 Coupled Ca Decrease with Increasing pH in Batch Reactor Systems

Initial Ca concentrations of 1 mM Ca (baseline Ca concentration from DOM), 10 mM Ca, and 30 mM Ca were tested in 2-line ferrihydrite systems where DOM was added simultaneously with Ca (Figure 2.3). Calcium concentration remained insignificantly changed in the absence of DOM at pH 4-6 for Figures 2.3A and 2.3B. Above pH 6, aqueous Ca concentration decreased until aqueous Ca concentrations of approximately 28.5 mM Ca and 9.25 mM Ca (for Figure 2.3A and 2.3B, respectively) at pH 9. Antelo et al. also observed no significant change in aqueous Ca concentration in systems equilibrated with 2-line ferrihydrite at acidic pH and a decrease in aqueous Ca concentration as pH increased (Antelo et al., 2015). However, Antelo et al. determined a significant decrease in aqueous Ca concentration began at approximately pH 8.5, which deviates from our observation of aqueous Ca concentration decreasing beginning at approximately pH 7. The disparity is most likely due to differences in experimental setup and potentially differences in mineral charge. The PZC of 2-line ferrihydrite supports our observations as the 2-line ferrihydrite should become negative at pH higher than approximately 7-7.5. In the presence of DOM, a similar trend was observed for Figures 2.3A and 2.3B; however, aqueous Ca concentration was lower for a majority of the tested pH range. In Figure 2.3A, aqueous Ca concentration was similar at pH 4 for the data sets with and without DOM but the data set with DOM began to decrease to a more significant extent (up to ~0.6 mM Ca

difference) than the data set without DOM. A similar trend was observed for Figure 2.3B; however, the difference between data sets was within standard error from pH 4-6. Differences in aqueous Ca concentration between the data sets with and without DOM increased up to 0.45 mM Ca at pH 9. Aqueous Ca concentration data in Figure 2.3C was performed at the baseline Ca concentration (~1 mM Ca) that was present in all sorption experiments (with no added Ca) at an initial C/Fe molar ratio of 4.7. Aqueous Ca concentration decreased at the greatest rate from pH 6-8 and at pH 9, reaching an aqueous Ca concentration minimum of 0.64 mM Ca.

Aqueous Ca data from Figure 2.3 correlate trends observed in Figure 2.2. Aqueous Ca concentration decreased to a greater extent than the Ca-ferrihydrate control for Figures 2.3A and 2.3B, which coincides with increased sorption of DOM at high pH and increasing Ca concentration observed in Figure 2.2. Decrease in aqueous Ca concentration is expected with increasing pH due to the 2-line ferrihydrate mineral surface becoming increasingly positively charged. However, the observed lower aqueous Ca concentration in the presence of DOM suggests that Ca may be interacting with both the DOM and 2-line ferrihydrate.

#### **2.3.4 Increased DOM Sequestration with Increasing Ca Concentration**

The effect of initial Ca concentration was further explored by performing separate DOM sorption experiments for initial C/Fe molar ratios of 4.7 and 12.5 with

increasing Ca concentration (Figure 2.4). Both the 4.7 and 12.5 C/Fe data sets were observed to have similar trends in sorbed OC concentration with initial Ca concentration ranging up to 60 mM Ca. Sorbed OC concentration increased linearly with increasing Ca concentration until an initial Ca concentration of 20 mM and then began to plateau at approximately 4.5 mmol OC g<sup>-1</sup> 2-line ferrihydrite greater than samples receiving zero initial Ca. Initial Ca concentrations greater than 60 mM Ca are expected to continue to increase sorbed OC concentration but to a lesser extent than what is observed from 0 to 60 mM Ca. Figure 2.4 provides further evidence that Ca is enhancing the sequestration of OM to 2-line ferrihydrite.

### **2.3.5 Elemental Mapping of Fe, Ca, and C**

All ferrihydrite samples reacted with either DOM or citric acid in the presence or absence of Ca were analyzed for spatial Fe, Ca, and C distribution using STXM mapping (Figure 2.5). For all STXM color-coded composite RGB maps, the presence of red, green, and blue are represented by C, Ca, and Fe, respectively. The intensity of the color correlates to optical density and represents the relative concentration of each respective element per unit area (Wan et al., 2007). Co-associations between C, Ca, and Fe may be identified by observing the colors produced by mixtures of red, green, and blue (RGB) and looking at the relative contributions of RGB values at regions of interest. For Figures 2.5A, 2.5C, and 2.5D, cyan-blue regions represent areas of poor

transmission and were identified as too thick (optical density > 2.25);<sup>29</sup> therefore, these regions were excluded from all further analyses. For Figure 2.5A (ferrihydrite-DOM, no Ca addition), the purple region represents a strong co-association of C and Fe. Similar C and Fe co-association was seen for ferrihydrite-OC adsorption complexes synthesized in similar experimental conditions (Chen et al., 2014a). A drastic difference in element co-association may be observed when ferrihydrite was reacted with DOM in the presence of Ca (Figure 2.5B). The purple regions observed in Figure 2.5A are mostly absent and predominately replaced by a pervasive network of white, grey and yellow, with hot spots of pink. The presence of white and grey regions represent areas at which Fe, Ca, and C are well associated, suggesting potential ternary relationships or homogenous distribution of C and Ca sorption sites. Yellow regions are found throughout the sample and indicate co-association of C and Ca. A high correlation between C and Ca has also been found for natural samples in similar STXM studies and will be discussed further (Chen et al., 2014a; Solomon et al., 2012; Wan et al., 2007). No separate C phases were observed in the DOM system, contrasting what was observed in Henneberry et al. (2012) in Fe-OM coprecipitate systems but similar to Chen et al. (2014b).

Differences in RGB maps for citric acid reacted samples were much less marked, as shown in Figure 2.5C and 2.5D. These particles possess a strong intensity of purple except the particle in the center of Fig. 2.5C, suggesting a strong association

of Fe and C. Unlike Figure 2.5B, no white, grey or, yellow regions were observed in Figure 2.5D; therefore, Figure 2.5D lacks the suggested Fe-Ca-C ternary associations observed in Figure 2.5B. Although the RGB elemental distribution maps allow for a qualitative analysis of Fe, Ca, C co-association, a more quantitative approach to identifying correlations between elements of interest may be performed by comparing elemental optical density.

### **2.3.6 Optical Density Correlation Between Elements**

Spatial correlations of Fe, Ca, and C are presented in elemental optical density correlation plots (Figure 2.6). The Fe/C optical density plot for the DOM-bearing ferrihydrite sample shown in Figure 2.6A showed a strong C/Fe correlation (0.9464) and C thickness ranging up to 135 nm. The high correlation is congruent with C/Fe relationship Chen et al.(2014) observed for DOM-ferrihydrite adsorption complexes. Compared to C STXM analysis of soils, the observed maximum C thickness of our samples was approximately 100 nm less; however, this disparity is suspected to be due to soil C microaggregate formation (Lehmann et al., 2007; Wan et al., 2007). Average C thickness was approximately 65 nm which is comparable to the 68 nm C thickness observed in Ultisols taken from oxic environments (Chen et al., 2014a). DOM sorption to ferrihydrite in the presence of 30 mM Ca resulted in a significant decrease in C/Fe correlation ( $R^2 = 0.6242$ , Figure 1B) with a concurrent strong correlation between C

and Ca ( $R^2 = 0.9144$ , Figure 2.5C), implying that different associations between Fe-C and Fe-Ca-C may exist. Ca/Fe was also found to have a strong positive correlation of 0.7373 (Figure 2.7A). Although the C/Fe correlation is lower in the system containing Ca, the optical density relationship for C/Fe, C/Ca, and Ca/Fe are positively correlated, indicating a high ternary association between Fe, Ca, and C. The 0.9144 correlation coefficient between C and Ca in Figure 2.5C demonstrates the potential importance of Ca content when modeling C cycling in environmental systems. The strong relationship between C and Ca has been observed in other STXM studies of natural soil samples. Phaeozem (Wan et al., 2007) (naturally high in Ca) and Ultisol (Chen et al., 2014a) (pasture soil receiving Ca from liming amendments) soils were found to have C/Ca optical density correlations of 0.767 and 0.870, respectively. Ca in both soils was also found to be well correlated to Fe ( $R^2 > 0.75$ ). With this in mind, STXM investigation of natural soils yielded similar results to what was seen in our ferrihydrite, Ca, and natural DOM systems; therefore, our results may be applicable to soil systems containing Fe oxides and Ca when investigating soil C cycling. Another interesting phenomenon is the decrease in C/Fe correlation by approximately a third when Ca and DOM were concurrently added to a ferrihydrite suspension. High correlation between C and Ca relative to the significant decrease in C/Fe correlation suggests that C is more closely associated with Ca in ternary systems containing Fe,

Ca, and C, potentially signifying that Ca is important to the complexation of C to Fe as a bridging element.

Calcium had a large effect on the optical density correlation plots in the DOM system; however, the effect of Ca on the citric acid system was observed to be less significant. The C/Fe optical density plot for citric acid-bearing ferrihydrite (Figure 2.6D) was found to have a low correlation between C and Fe. The poor correlation between C and Fe in this system is most likely attributable to poor transmission due to sample thickness throughout a large portion of citric acid-ferrihydrite STXM map. Sample thickness was not a major issue for the citric acid-bearing ferrihydrite sample reacted in the presence of Ca (Figure 2.6E, F). A strong correlation coefficient of 0.7636 was found between C and Fe, suggesting a strong relationship between C and Fe. This is expected to be the case as citric acid is a tricarboxylic acid that is known to form inner sphere complexes with iron oxides (Kleber et al., 2015; Lackovic et al., 2003). Unlike the DOM system in Figure 2.6C, Figure 2.6F shows a much lower correlation between C and Ca in the citric acid system. From this observation, it may be suggested that citric acid is less associated with Ca than natural DOM. This may be due to the heterogeneity of OC functional moieties in the DOM solution versus the singular carboxylic species present in citric acid (tricarboxylic acid). Interestingly, Ca is highly associated with Fe in the citric acid system (2.7B) compared to the DOM system. C/Ca and Ca/Fe correlations in the citric acid system, in conjunction with the

analysis of Figure 2.6D, are likely best explained by both Ca and C being sorbed separately to the ferrihydrite surface such that Ca and C are not highly associated.

### **2.3.7 2.3.7 C K-edge STXM-NEXAFS of DOM**

STXM-NEXAFS analysis was used to spatially investigate the chemical speciation of sequestered OC to ferrihydrite in the absence and presence of Ca (Figure 2.8 and 2.9, respectively). Optical density of the averaged stack images (Figures 2.8A and 2.9A) increase with the intensity of white and decreases with the degree of black. The pre-edge averaged image was subtracted from the averaged stack image on the C K-edge in order to focus on areas representing sequestered C and to identify areas affected by sample thickness (Figure 2.8B and 2.9B). Principal component analysis (PCA) was used to identify unique clusters of pixels within each STXM stack that represent regions of statistically different C 1s NEXAFS spectra (Figure 2.8C and 2.9C) (Lerotic et al., 2005). The red cluster in Figure 2.8C is a region identified as having poor sample transmission and was excluded from the analysis; however, all regions in Figure 2.9C were found to be of appropriate thickness. Corresponding C 1s NEXAFS for the whole sample, all clusters of interest identified through PCA, and a DOM standard were collected (Figures 2.8D and 2.9D). Resonance energies taken from the C 1s NEXAFS data may be used to identify functional groups present in the sample (Table 2.7) which was then used to characterize OC species present for all

samples tested (Armbruster et al., 2009; Chen et al., 2014a; Henneberry et al., 2012; Plaschke et al., 2005; Solomon et al., 2012; Wan et al., 2007).

For the DOM-bearing ferrihydrite sample reacted in the absence of Ca, three unique clusters were observed from the PCA (Figure 2.8C and 2.8D). Cluster 1 (yellow) was found to be the most predominant within the DOM-ferrihydrite adsorption complex and corresponded well to the spectra of the whole sample. Both of the spectra are dominated by a peak at 288.5 eV representing carboxylic C (Lehmann et al., 2007; Solomon et al., 2012; Wan et al., 2007). Compared to the DOM standard, the carboxylic peak for the whole sample and Cluster 1 spectra is diminished and significantly broader. This feature is indicative of carboxylate complexation to Fe oxide, likely through ligand exchange processes (Chen et al., 2014a; Plaschke et al., 2005). Slight features at 285.6 eV and 286.7 eV were also observed, representing the presence of aromatic and phenolic C functional moieties. These features are severely diminished compared to the DOM standard, suggesting that aromatic and phenolic groups in the DOM are not preferentially sequestered to ferrihydrite (Chen and Sparks, 2015; Wan et al., 2007). Cluster 2 (green) and 3 (purple) were found at the edge of the particle and were found to have sharper peaks at 288.5 eV than those observed for the whole sample and Cluster 1. The strong, thin peak at resonance energy 288.5 eV suggests that carboxylic C is still the most predominant resonance feature but is largely representative of the DOM standard and thus may not be as strongly

complexed to ferrihydrite compared to the Cluster 1 region (Chen et al., 2014a; Lehmann et al., 2007). For Cluster 2 and 3, the phenolic peak at approximately 286.8 eV was heightened, indicating that there may be localized areas on ferrihydrite that preferentially sequester phenolic C from DOM. Aromatic groups for both Cluster 2 and 3 were found to be comparable to the whole sample spectra and Cluster 1.

Carbon 1s NEXAFS spectra collected for ferrihydrite-Ca-DOM (Figure 2.9D) were found to have predominant dissimilarities to the spectra from the ferrihydrite-DOM system (Figure 2.8D). Compared to Figure 3D, the most predominant feature change promoted by the presence of Ca was the extreme diminishment of the carboxylic C peak at 288.5 eV (~30% decrease in relative peak area compared to the DOM standard) and the emergence of a shoulder at 287.3-287.6 eV. This feature was observed for all cluster spectra shown in Figure 4D. Plaschke et al. (2005) and Armbruster et al. (2009) saw congruent features in C 1s NEXAFS spectra of humic sorption to various polyvalent metal ions. Polyvalent metal ion complexation with humic acid resulted in a decrease in the carboxylic C resonance intensity with concomitant emergence of a shoulder approximately 1 eV below the carboxylic peak (Armbruster et al., 2009; Plaschke et al., 2005). The sharp decrease in our sample spectra in Figure 2.9D with the emergence of the aforementioned shoulder strongly suggests that Ca is may be interacting with DOM carboxylic C groups. The absence of shoulder formation at 287.3-287.6 eV and the high intensity carboxylic C resonance

energy at 288.5 eV in Figure 2.8D suggests that the ferrihydrite-Ca-DOM system is uniquely binding carboxylic C compared to the relatively simpler spectra observed for the ferrihydrite-DOM system; therefore, the feature changes at 288.5 eV and 287.3-287.6 eV are suggestive that the presence of Ca affects the binding of DOM to ferrihydrite. We expect this feature would be promoted further for ferrihydrite-Ca-DOM samples synthesized at increasing pH, which will be analyzed further in future research.

Resonance energies representative of aromatic C (285.3-285.6 eV) in the ferrihydrite-Ca-DOM system (Figure 2.9D) are also found to significantly differ from the ferrihydrite-DOM system (Figure 2.8D). All clusters in Figure 2.9D show a higher intensity, developed aromatic peak at 285.6 eV compared to Figure 2.8D. Chen et al. (2014b) inferred that increases in aromatic C peak intensity is associated with increased aromatic C complexation to ferrihydrite complexes; therefore, the spectra suggest that the Ca-containing system may be facilitating increased association of aromatic C to ferrihydrite. Phenolic groups were also identified in the sample spectra at 286.7-286.9 eV; however, there were no noticeable differences between Figure 2.8D and 2.9D.

Although all ferrihydrite-Ca-DOM C 1s NEXAFS spectra in Figure 2.9D were found to have similar peak locations/features, Cluster 2Ca (green) was found to possess the most distinguishable features. This region represents a large continuous

region on the ferrihydrite particle shown in Figure 2.9C. A clear shoulder can be observed at approximately 287.3 eV, along with the diminishment of the carboxylic C peak at 288.5 eV. Also, a distinct, relatively high intensity aromatic peak at 285.6 eV was observed. In conjunction with this unique spectra, the Cluster 2Ca region was also observed in Figure 2.5B. High intensity optical density contributions from C (red), Ca (green), and Fe (blue) were observed in almost equal proportions from the same region represented by Cluster 2Ca in Figure 2.9C, resulting in this region appearing white. Due to the presence of unique C NEXAFS features that differ greatly from the system receiving no Ca inputs and the high degree of association between Fe, Ca, and C observed in Figure 2.5B, Cluster 2Ca is expected to be a region of Fe-Ca-C ternary complexation, potentially through Ca-bridging structures.

### **2.3.8 C K-edge STXM-NEXAFS Analysis of Citric Acid**

PCA revealed only one unique cluster shown in yellow for the ferrihydrite-citric acid (Figure 2.10A) and red for the ferrihydrite-Ca-citric acid. The contrasting color (red and yellow, respectively) represent regions that were identified as too thick for further analysis. Ferrihydrite-citric acid and ferrihydrite-Ca-citric acid spectra (Figure 2.10C) were found to have similar features. Both spectra were dominated by a broad carboxylic C peak at 288.5 eV with no other significant features. The broad carboxylic C peak for both samples suggest that both citric acid-treated samples are

complexing strongly to ferrihydrite, similar to the feature seen for the ferrihydrite-DOM spectra (Figure 2.10C). No major differences in the C 1s NEXAFS spectra were observed when citric acid was reacted with ferrihydrite in the presence of Ca; therefore, we expect that Ca has little to no effect on the complexation of OC derived from citric acid.

### **2.3.9 Ca L-edge STXM-NEXAFS Analysis**

Ca 2p NEXAFS spectra were collected for both ferrihydrite-Ca-DOM and ferrihydrite-Ca-citric acid samples. For both, PCA revealed only one unique spectra (Figure 2.11). Four Ca reference spectra were used: Ca-bearing ferrihydrite, sorbed Ca to extracellular polymeric substance (EPS), CaCl<sub>2</sub>, and calcite (Chen et al., 2014a; Obst et al., 2009). For both DOM and citric samples, four total peaks were observed. L<sub>3</sub> 2P<sub>3/2</sub> and L<sub>2</sub> 2P<sub>1/2</sub> peaks were observed at 349.2 and 352.6 eV, respectively. These two major peaks are characteristic of Ca spin-orbital partners found in Ca L-edge NEXAFS (Cody et al., 1995). A smaller peak precedes each previously mentioned larger peak at 348.2 and 351.4, respectively, and gives an indication of the crystallinity of present Ca structures (Politi et al., 2008).

When comparing both ferrihydrite-Ca-DOM (Fh\_Ca\_DOM) and ferrihydrite-Ca-citric acid (Fh\_Ca\_Citric Acid) Ca 2p NEXAFS spectra to reference spectra (Figure 2.11), both samples corresponded poorly to calcite and CaCl<sub>2</sub> and well to the

Ca-bearing ferrihydrite (Fh\_Ca) and Ca-containing organic compound (Sorbed Ca\_EPS). The calcite spectra poorly agrees with our samples and CaCl<sub>2</sub> was found to have higher intensity peaks at the two small L<sub>3</sub> 2P<sub>3/2</sub> and L<sub>2</sub> 2P<sub>1/2</sub> with all four peaks shifted to a slightly lower eV (349.2 and 352.4 eV for the two major peaks at (ii) and (iv); 348 and 351.3 eV for two smaller peaks at (i) and (iii) (Figure 2.11) characteristic of Ca L-edge NEXAFS for CaCl<sub>2</sub> (Araújo et al., 2015). Therefore, we conclude that present Ca species are not present in the form of calcite nor CaCl<sub>2</sub>. The sorbed Ca\_EPS and Fh\_Ca reference standards were found to correspond well to our samples, mostly due to similar nature of the low intensity L<sub>3</sub> 2P<sub>3/2</sub> and L<sub>2</sub> 2P<sub>1/2</sub> peaks at 348.2 and 351.4 eV, respectively. This suggests that Ca incorporated into ferrihydrite-Ca-OC samples are of poorly crystalline or amorphous nature (Politi et al., 2008). Fh\_Ca was observed to have higher peak intensity at the L<sub>3</sub> 2P<sub>3/2</sub> (349.2 eV) and L<sub>2</sub> 2P<sub>1/2</sub> (352.6 eV) peaks compared to the sample spectra, especially for the Fh\_Ca\_DOM sample, suggesting that the concurrent presence of ferrihydrite and DOM may have a unique impact on the coordination of Ca; however, the role of Ca as a bridging cation needs to further explored in future spectroscopic analysis.

### **2.3.10 ATR-FTIR**

In conjunction with C 1s NEXAFS, ATR-FTIR data was collected for ferrihydrite samples reacted with DOM or citric acid in the absence or presence of Ca

in order to probe C speciation and mechanism of sorption (Figure 2.12). In addition to the molar C/Fe ratio used for STXM samples (4.7 C/Fe), a lower molar ratio of 2.5 C/Fe was also tested in order to probe features that otherwise would be undistinguishable (Chen et al., 2014b). An absorbance band at  $1585\text{ cm}^{-1}$  was observed for the DOM stock and for 2.5 C/Fe DOM\_ 30 mM Ca, with every other sample, except, having a band at approximately  $1570\text{ cm}^{-1}$ . Absorbance band formation from  $1585$  to  $1570\text{ cm}^{-1}$  is associated with the presence of asymmetric carboxyl C groups (Table 2.3). All bands, excluding 2.5 C/Fe DOM\_ 30 mM Ca, were found to shift from  $1585$  to  $1570\text{ cm}^{-1}$  and have decreased intensity compared to the DOM standard. The shift and depression of the asymmetric carboxyl C band suggests that asymmetric carboxyl C may be strongly bound to ferrihydrite (Chen et al., 2014b; Heckman et al., 2011; Lackovic et al., 2003). In conjunction with the asymmetric carboxyl C band, a symmetric carboxyl band may be found from  $1400$  to  $1380\text{ cm}^{-1}$  for all samples. The DOM standard has a high intensity absorbance band at  $1400\text{ cm}^{-1}$ , but all other C-reacted ferrihydrite samples were found to shift to  $1384$  or  $1380\text{ cm}^{-1}$ . Shifting of the symmetric carboxyl C group from  $1400$  to  $1384\text{ cm}^{-1}$  is a well-documented characteristic of OC sorption to ferrihydrite through ligand exchange processes (Chen et al., 2014b; Fu and Quan, 2006; Lackovic et al., 2003), suggesting that ligand exchange of OC to ferrihydrite through symmetric carboxyl C groups is a predominant mechanism of sorption for both citric acid and DOM samples.

Interestingly, the 2.5 C/Fe DOM\_ 30 mM Ca was found to have different absorbance band features compared to all other samples. The asymmetric carboxyl C band was significantly decreased similar to other samples but did not shift from 1585 to 1570  $\text{cm}^{-1}$ . The decreased intensity of this peak compared to the DOM stock suggests that asymmetric carboxyl C is associating with ferrihydrite in sample 2.5 C/Fe DOM\_ 30 mM Ca; however, the lack of a shift suggests that asymmetric carboxyl C is binding weakly to ferrihydrite in this system (Gu et al., 1994; Heckman et al., 2011). Also, the symmetric carboxyl C peak was found to shift to 1380  $\text{cm}^{-1}$  rather than 1384  $\text{cm}^{-1}$  and had a higher peak intensity compared to sample 2.5 C/Fe DOM\_No Ca. The increased shift and intensity of the symmetric carboxyl C band for 2.5 C/Fe DOM\_30 mM Ca compared to 2.5 C/Fe DOM\_No Ca suggests that Ca is playing a role in the binding of symmetric carboxyl C, likely through ligand exchange processes (Fu and Quan, 2006; Heckman et al., 2011). Changes in aromatic and phenolic absorbance bands were indistinguishable from the collected ATR-FTIR spectra, likely due to the strong absorbance bands of carboxyl C. Polysaccharide peaks (Table 2.3) were also observed in spectra for the DOM systems, indicating the presence of sequestered DOM polysaccharide functional groups (Artz et al., 2008; Heckman et al., 2011), but to a lesser degree compared to carboxyl C functional groups.

## 2.4 Evidence for Fe-Ca-OC Ternary Complex Formation

Through a combination of batch experiments, spatial associations, and C NEXAFS spectra obtained primarily via STXM-NEXAFS, we have investigated potential ternary interactions of Fe, Ca, and OM in systems containing ferrihydrite, Ca, and either DOM or citric acid (Sowers et al., 2018a; Sowers et al., 2018b). Results from batch reactions were shown to synergistically influence OM sorption to ferrihydrite for all pH values tested (pH 4-9). Evenly-proportioned mixtures of C, Ca, and Fe in color-coded RGB maps, high correlation ( $R^2 = 0.91$ ) between C and Ca in optical density correlation plots, and the polyvalent metal ion complexation C 1s NEXAFS feature (decrease of the carboxyl C peak at 288.5 eV paired with the emergence of a shoulder at 287.5 eV) all provide significant evidence that Fe-Ca-OC complexes are forming in systems containing ferrihydrite, Ca, and natural DOM, likely through cation-bridging of carboxylic C to the ferrihydrite surface. Additionally, for the DOM system, the optical density correlation of the C/Fe plot was found to decrease from  $R^2 = 0.95$  to  $R^2 = 0.62$  when Ca was added, along with high C/Ca and Ca/Fe correlation ( $R^2 = 0.91$  and  $0.74$ , respectively). This indicates that Ca is well associated to both C and Fe whereas C is significantly more associated with Ca than Fe; therefore, we suggest that Ca is significantly involved in the complexation of C to Fe, most likely through Ca-bridging structures. ATR-IR data supports this conclusion, as features indicative of ligand exchange of symmetric carboxyl C were observed and

enhanced with the addition of Ca. These findings relate well to the work of others that have observed high correlation of C, Ca, and Fe in iron oxide and soil systems (Chen et al., 2014a; Chen et al., 2014b; Mikutta et al., 2007; Wan et al., 2007). Citric acid and Fe were found to well-related; however, none of the ternary features observed for DOM were observed for the citric acid systems. This is likely due to the chemical heterogeneity of natural DOM; however, this needs to be further explored using other model OC compounds.

Overall, the proposed occurrence of Fe-Ca-OC ternary complexes has the potential to significantly impact how organo-mineral associations are modeled in current environmental C cycling models and the development of potential C sequestration management strategies in soil systems containing Fe oxides. We expect this phenomenon, measured currently at slightly acidic pH conditions, to occur to a greater extent in basic, calcareous soils, which is in need of further examination. Also, we have observed that increasing Ca concentration from 1 mM Ca up to 30 mM Ca resulted in increased OC sorption for samples equilibrated at initial molar C/Fe ratios of 4.7 and 12.5. Therefore, we expect that ternary complexation may be occurring in a wide range of systems, which warrants further spectroscopic investigation. Additional work needs to be performed to understand the stability of proposed Fe-Ca-OC ternary complexes with changing environmental conditions (redox, temperature, etc.). Increased spectroscopic work is also needed to elucidate the proposed Ca-bridging

mechanism of Fe-Ca-OC ternary complexes, which may be accomplished using chemically similar polyvalent cations of greater atomic mass (e.g., strontium).

Table 2.1: Aqueous carbon concentrations of DOM stock solution.

<b>Total Inorganic C</b>	<b>Total C</b>	<b>Total Organic Carbon</b>
<b>(mg/L)</b>	<b>(mg/L)</b>	<b>(mg/L)</b>
1.58	2029.98	2028.40

Table 2.2: Aqueous elemental composition of DOM stock solution.

<b>Al</b>	<b>Ca</b>	<b>Cu</b>	<b>Fe</b>	<b>K</b>	<b>Mg</b>	<b>Na</b>	<b>P</b>	<b>S</b>	<b>Zn</b>	<b>As</b>	<b>Pb</b>
<b>(mg/l)</b>											
4.470	152.461	2.340	7.123	30.359	57.734	3.849	43.804	18.956	2.148	0.045	0.154

Table 2.3: Observed peak positions for ATR-FTIR spectra. Peak assignments and references supporting assignment are included.

Peak Position (cm <sup>-1</sup> )	Peak Assignment	References
1585-1570	Asymmetric COO <sup>-</sup> Stretch	Heckman et al., 2011; Lackovic et al., 2003
1530-1520	Aromatic C=C Stretch	Chen et al., 2014; Gu et al., 1994
1400	Symmetric COO- Stretch	Gu et al., 1994; Fu and Quan 2006; Heckman et al., 2011; Lackovic et al., 2003
1384	COO-Fe stretch	Chen et al., 2014; Fu and Quan, 2006; Lackovic et al., 2003
1270	Stretching of phenolic OH	Gu et al., 1994; Artz et al., 2008; Chen et al., 2014
1250	OH deformation of COOH	Gu et al., 1994; Heckman et al., 2011
1120	Polysaccharides: C-O stretch	Chen et al., 2014; Heckman et al, 2011
1080	Polysaccharides: C-O stretch	Artz et al., 2008; Chen et al., 2014; Heckman et al., 2011
1040	Polysaccharides: C-O stretch	Chorover and Amistadi, 2001; Grube et al., 2006

Table 2.4: Pre-edge energy and edge-energy ranges used for average stack maps, along with optical density conversion factors used to convert optical density to elemental thickness.

Element	Absorption Edge	Pre-edge Energy Stack Range (eV)	Edge Energy Stack Range (ev)	Optical Density to Element Thickness Conversion Factor (nm/OD)
C	K	280-282	287.7-288.8	239.60
Ca	L <sub>2</sub>	350.3-350.7	352.3-352.9	40.00
Fe	L <sub>3</sub>	700-703	709.5-710.5	66.67

Table 2.5: Values used to convert the C optical density to C thickness.

$\mu(\text{cm}^2 \text{g}^{-1})$	Resonance Enhancements	$\rho (\text{g cm}^{-3})^*$	$f(\text{g g}^{-1})^*$
51400	1	1.4	0.58

\*Values derived from Stevenson et al., 1994.

Table 2.6: Langmuir parameters used to model sorption of DOM and citric acid to 2-line ferrihydrite.

<b>Organic C Source</b>	<b>Calcium Treatment</b>	<b>S<sub>max</sub> (mmol OC g<sup>-1</sup> ferrihydrite)</b>	<b>K</b>	<b>E</b>
DOM	No Ca Control	23.13 +/- 0.7455	0.004 +/- 0.001	0.978
	4 mM Ca	23.41 +/- 0.5125	0.006 +/- 0.001	0.989
Citric Acid	No Calcium	11.32 +/- 0.4690	0.005 +/- 0.001	0.967
	4 mM Ca	10.89 +/- 0.6903	0.008 +/- 0.002	0.906

S<sub>max</sub> = predicted maximum sorbed concentration; K = sorption constant; E = model efficiency.

Table 2.7: C 1s NEXAFS peak energies with C functional group interpretation.

Peak Number	Peak Energies (eV)	C Functional Groups	Transition	References
i, ii	285.2-285.6	Aromatic (C <sub>aromatic</sub> =C <sub>aromatic</sub> )	1s- $\pi^*$	Henneberry et al., 2009; Solomon et al., 2012; Chen et al., 2014
iii	286.7-286.9	Phenolic C <sub>aromatic</sub> -OH	1s- $\pi^*$	Wan et al., 2007; Solomon et al., 2012; Chen et al., 2014
iv	287.5	Aliphatic (C-H)	1s-3p/ $\sigma^*$	Wan et al., 2007; Solomon et al., 2013
Boxed Region	287.2-287.6	Polyvalent metal ion complexation to COOH	NA	Plaschke et al., 2005; Armbruster et al., 2009
v	288.5	Carboxylic Acid (COOH)	1s- $\pi^*$	Wan et al., 2007; Solomon et al., 2012; Chen et al., 2014

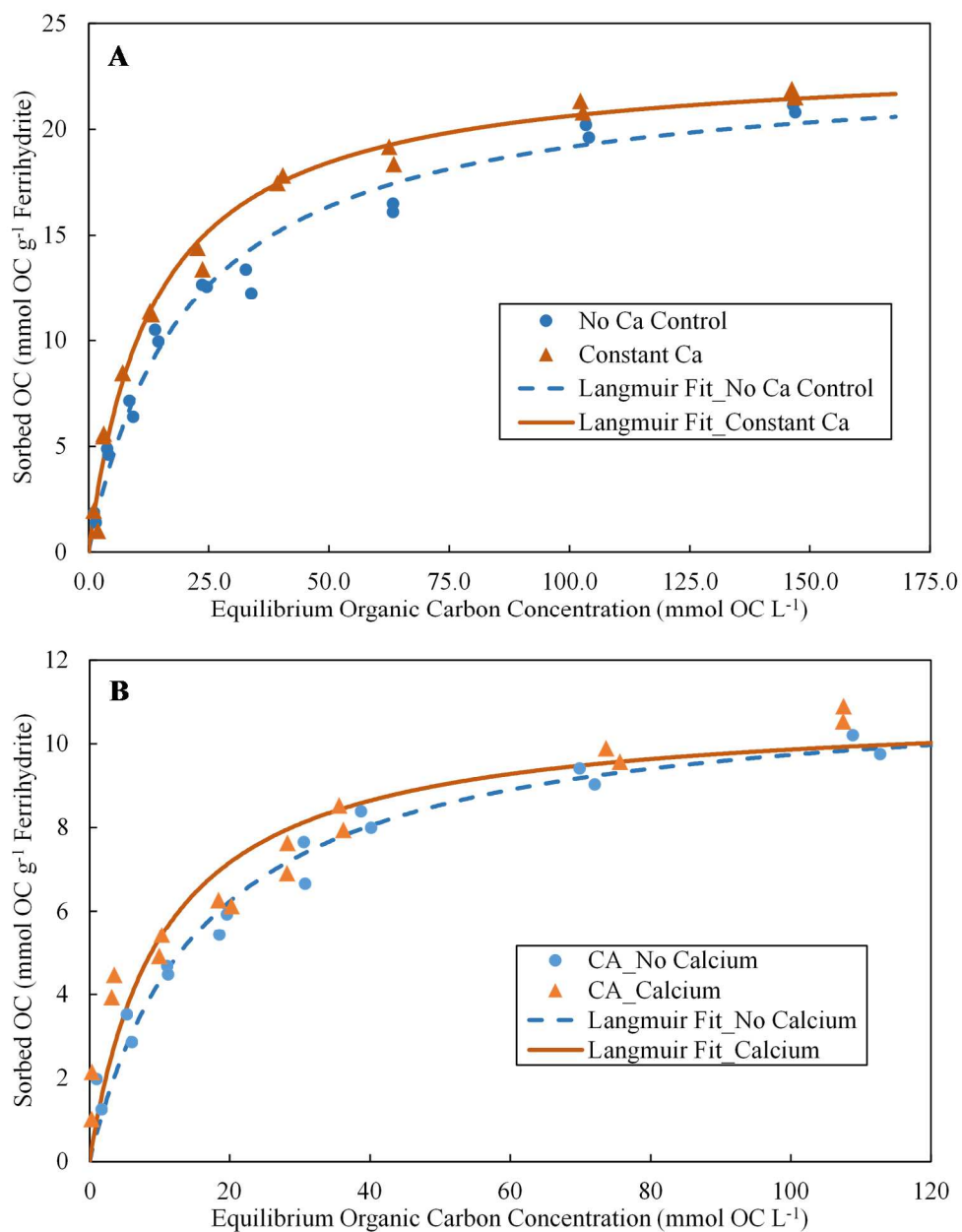


Figure 2.1: DOM (a) and citric acid (b) were reacted with ferrihydrite at  $\text{pH } 6.25 \pm 0.10$  in duplicate. Samples were treated with and without Ca addition. Sample receiving Ca had a total Ca concentration of 4 mM Ca (152 mg Ca L<sup>-1</sup>).

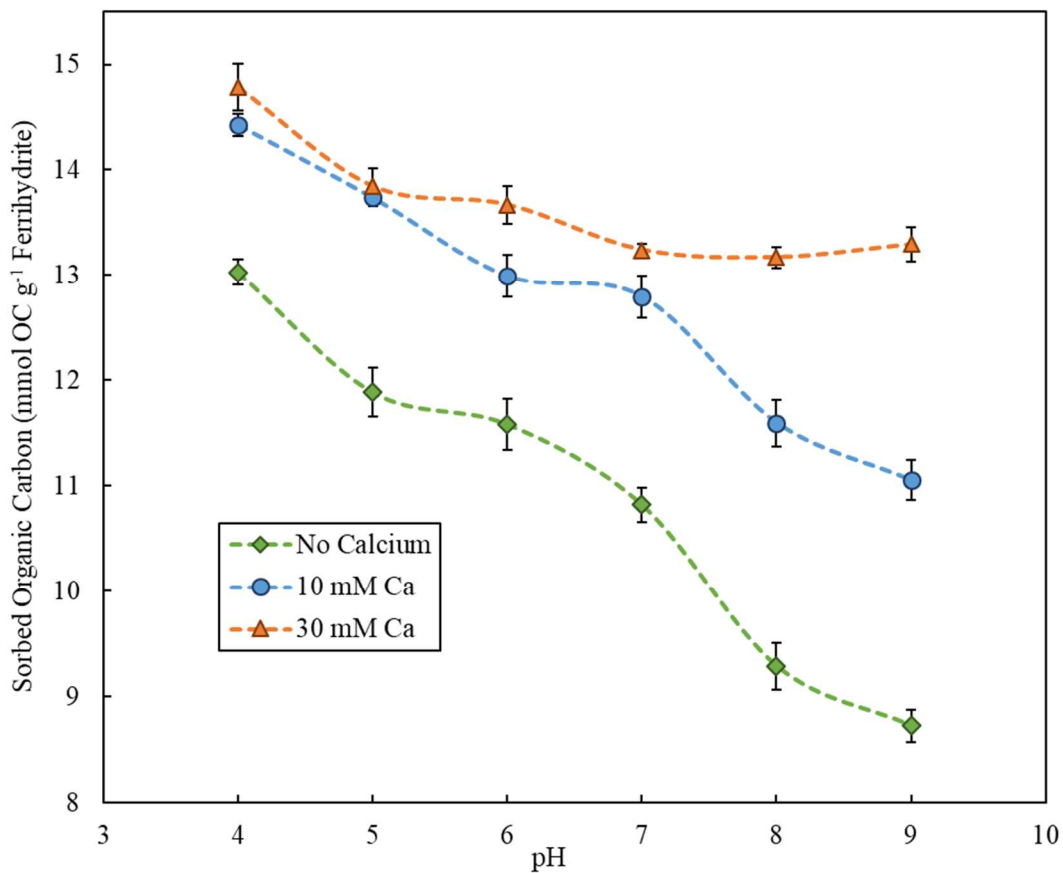


Figure 2.2: Sorption envelopes of DOM sorption to ferrihydrate at pH 4 to 9 in the presence of no added Ca (a), 10 mM Ca (b), or 30 mM Ca (c). An initial C/Fe ratio of 4.7 was used for all samples and experiments were performed in triplicate.

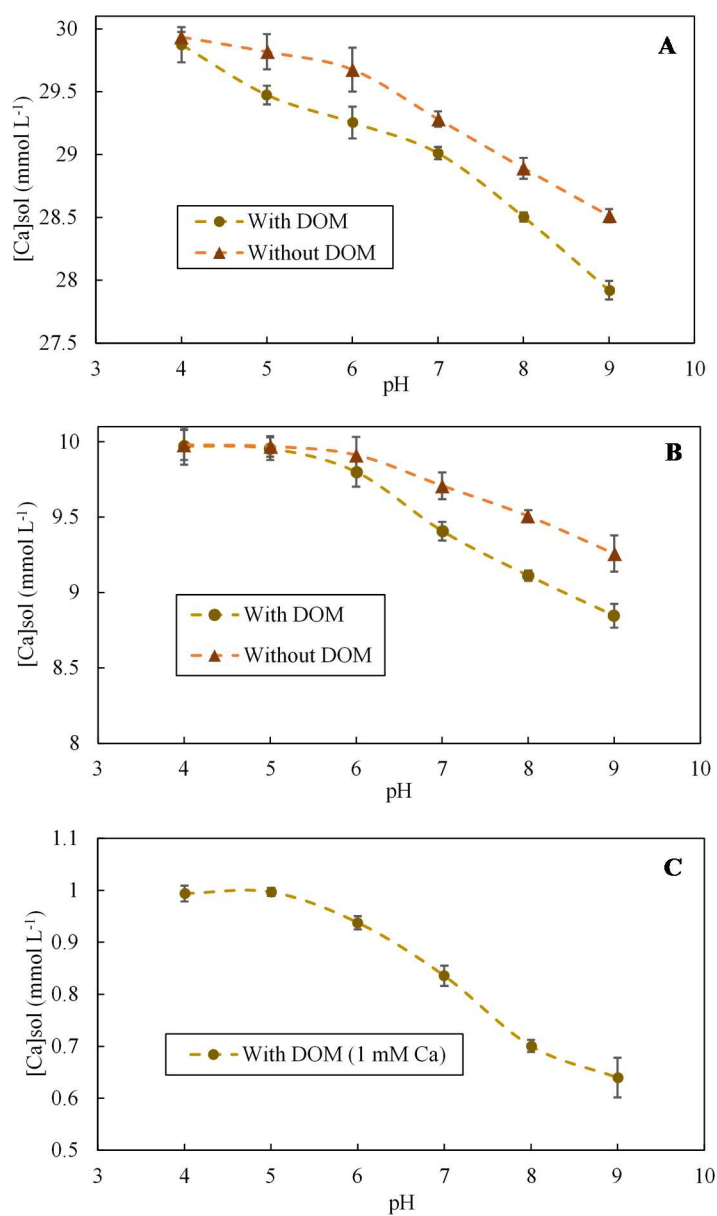


Figure 2.3: Aqueous Ca data from sorption envelope experiments conducted from pH 4 to 9. The multicomponent systems consisted of Ca and ferrihydrite or Ca, ferrihydrite, and DOM. The greater decrease in aqueous Ca in the DOM multicomponent system compared to the system without DOM is thought to occur due to ternary interactions of ferrihydrite, Ca, and DOM.

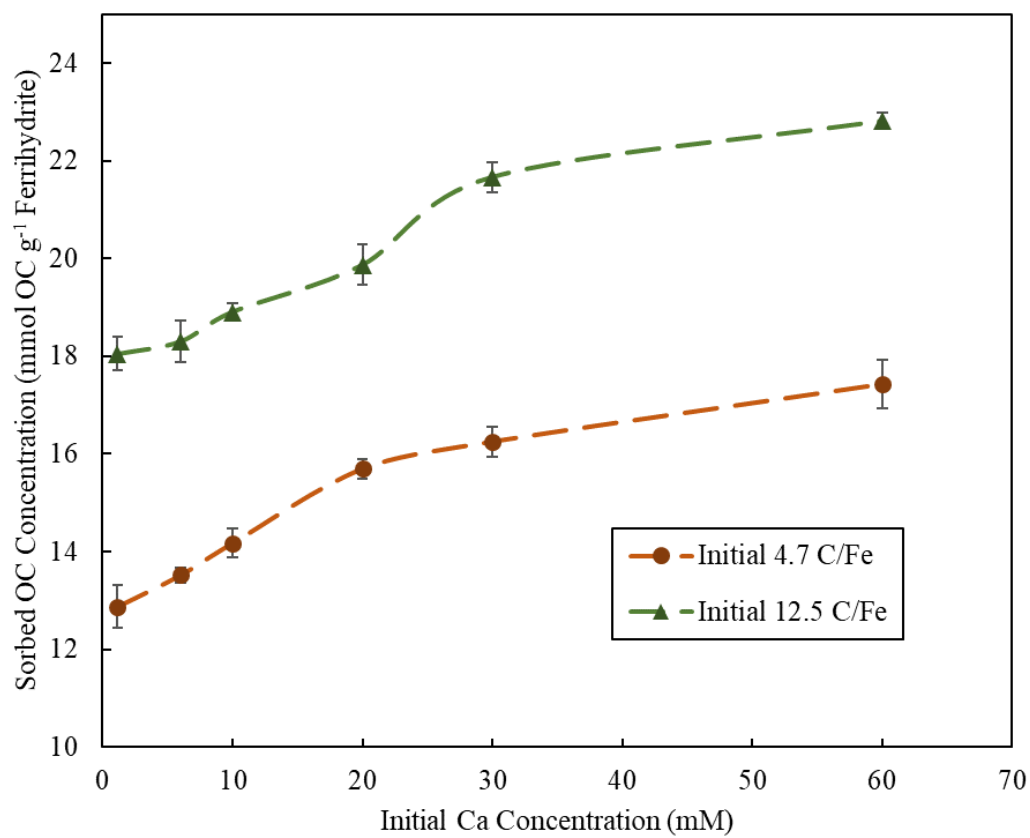


Figure 2.4: Sorption of DOM to 2-line ferrihydrite at 4.7 and 12.5 initial C/Fe molar ratios with increasing calcium concentration (up to 60 mM Ca) at pH  $6.25 \pm 0.10$ .

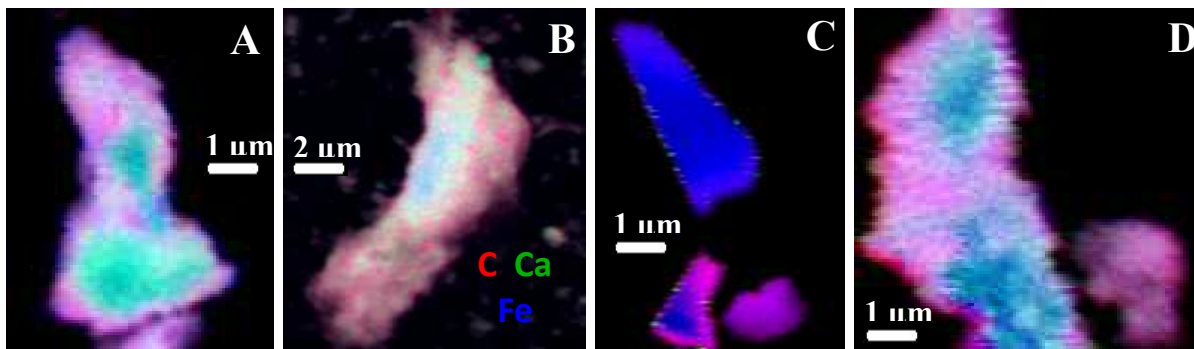


Figure 2.5: Color-coded composite RGB optical density maps created from STXM-NEXAFS data. Red, green, and blue represent carbon, calcium, and iron, respectively. RGB maps are shown for ferrihydrite-DOM (A), ferrihydrite-Ca-DOM (B), ferrihydrite-citric acid (C), and ferrihydrite-Ca-citric acid samples (D). Cyan regions in Figure 1A and Figure 1D were identified as regions too thick for transmission.

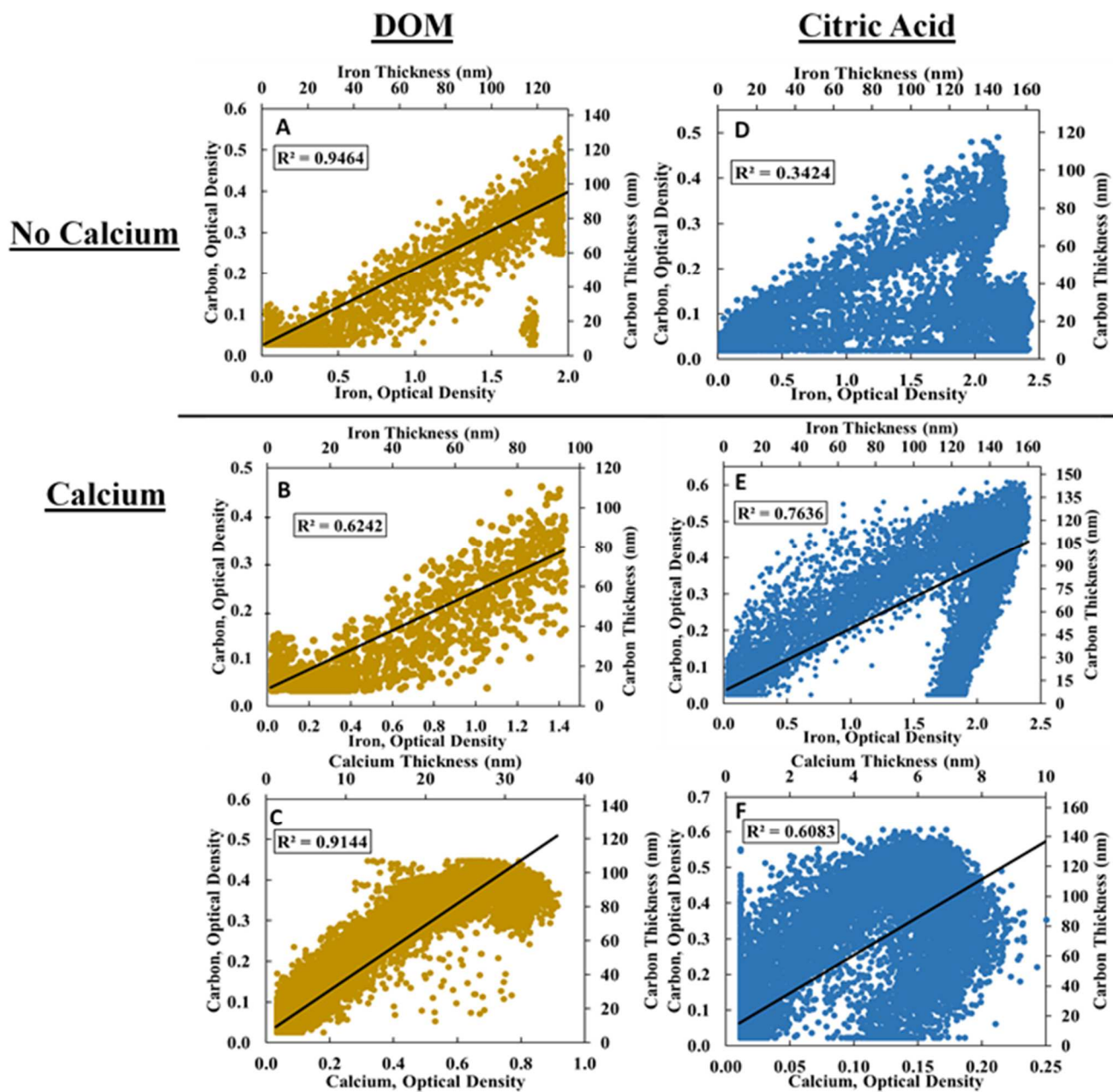


Figure 2.6: Elemental optical density correlation plots between C, Ca, and Fe for DOM-bearing (A-C) and citric acid-bearing (D-F) ferrihydrite. Linear correlation coefficients are provided for each plot. Thickness values for each element are also provided (calculated using SI Table S3).

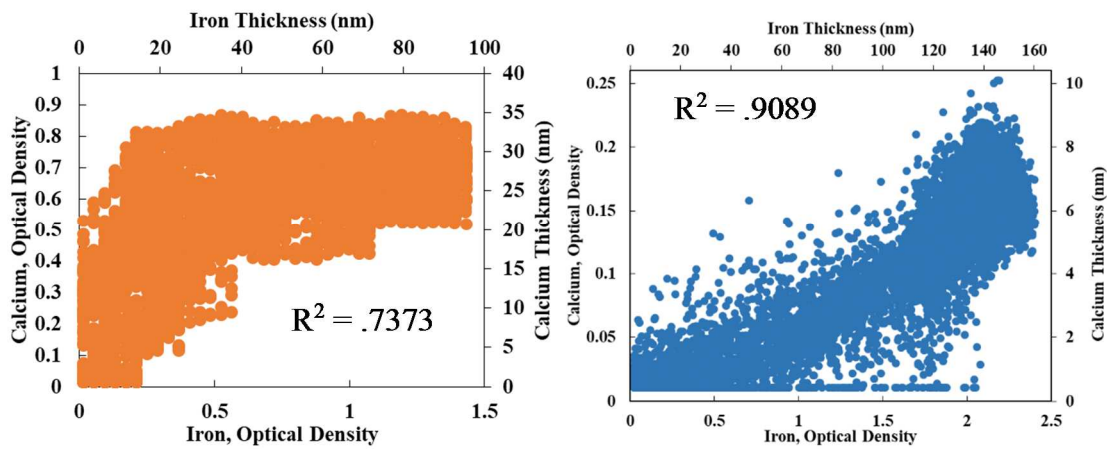


Figure 2.7: Optical density correlation plots of Ca versus Fe for ferrihydrite samples reacted with DOM (left) or citric acid (right) in the presence of Ca.

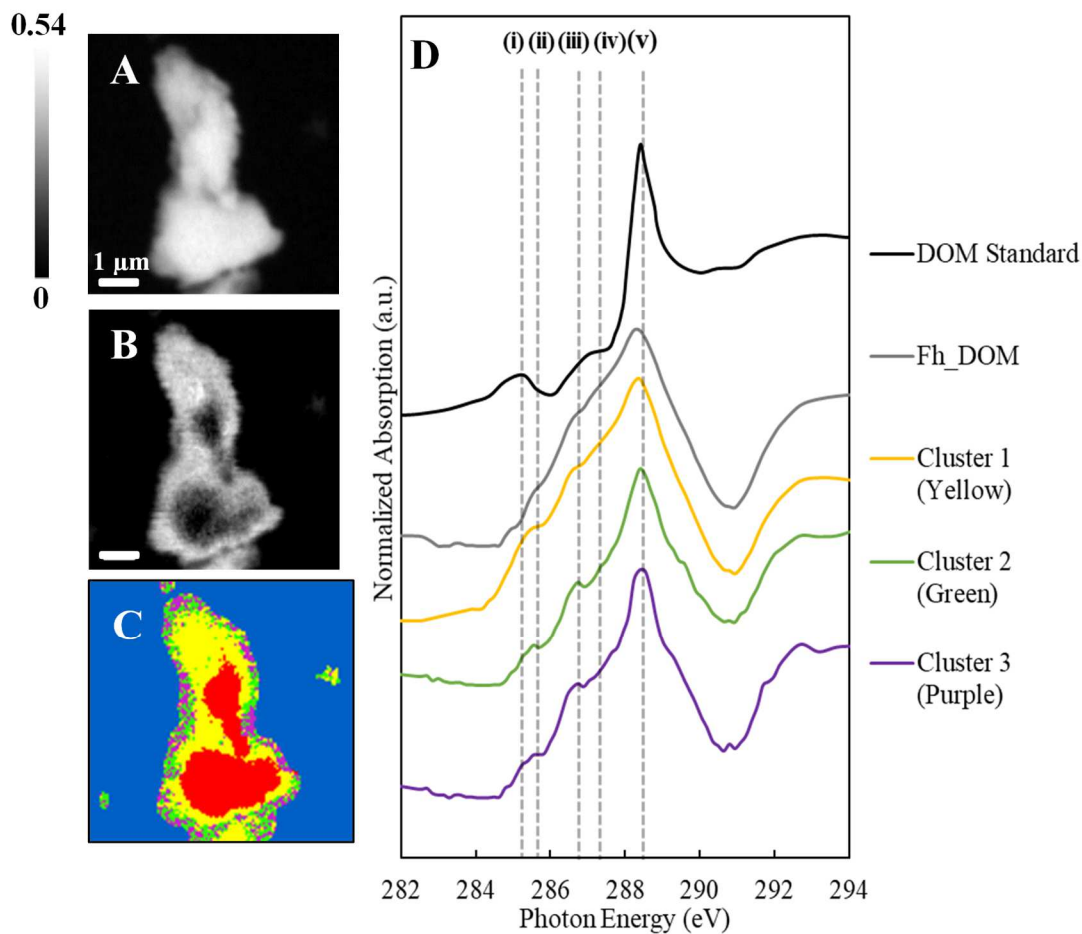


Figure 2.8: C K-edge STXM average stack optical density map for ferrihydrite-DOM of the C K-edge (287.7-288.8 eV) and the C K-edge minus C pre-edge (287.7-288.8 eV minus 280-282 eV) difference map are shown in A and B, respectively. PCA of the C K-edge stack is shown in C and respective C 1s STXM-NEXAFS spectra for the whole sample and each of the 3 clusters identified through PCA are shown in D. A standard of the DOM stock is also included. Peak assignments are located in Table 7.

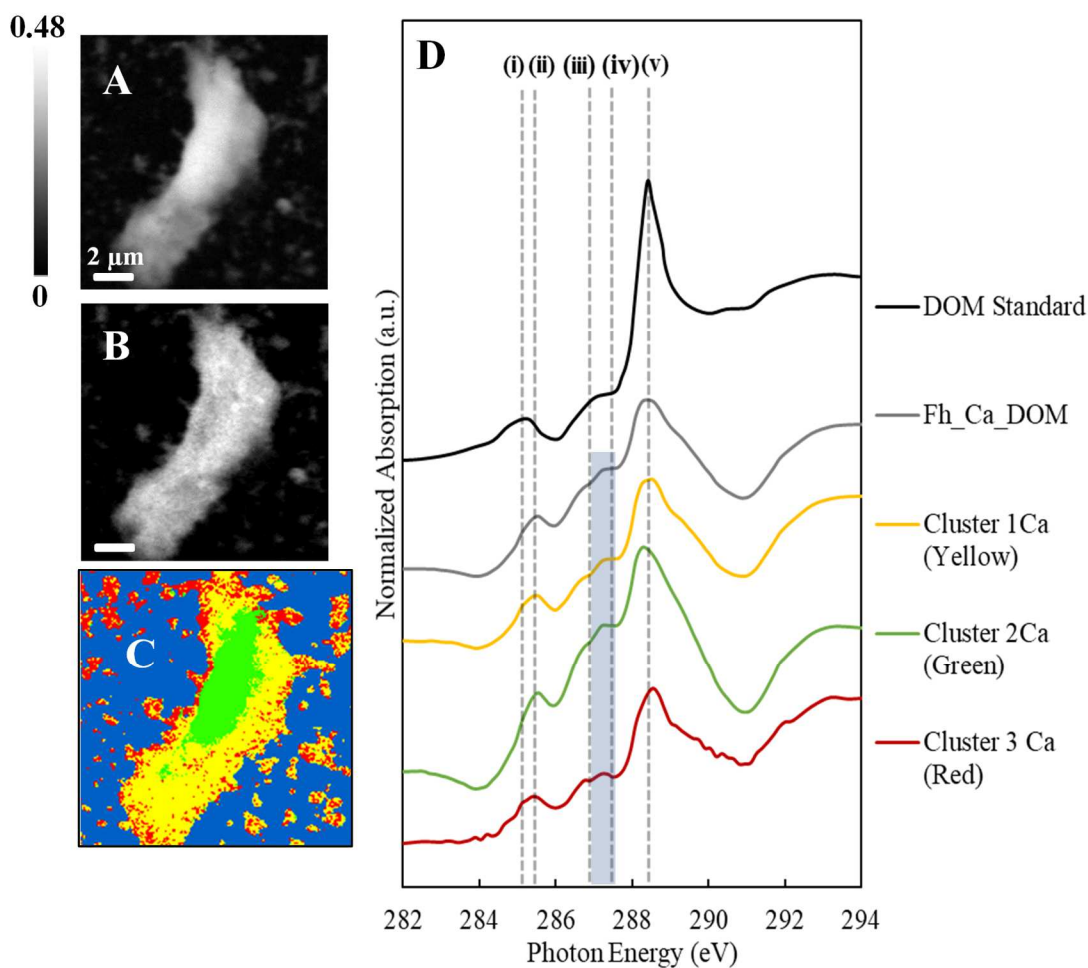


Figure 2.9: C K-edge STXM average stack optical density map for ferrihydrite-Ca-DOM of the C K-edge (287.7-288.8 eV) and the C K-edge minus C pre-edge (287.7-288.8 eV minus 280-282 eV) difference map are shown in A and B, respectively. PCA of the C K-edge stack is shown in C and respective C 1s STXM-NEXAFS spectra for the whole sample and each of the 3 clusters identified through PCA are shown in D. A standard of the DOM stock is also included.<sup>9</sup> Peak assignments are located in Table 7.

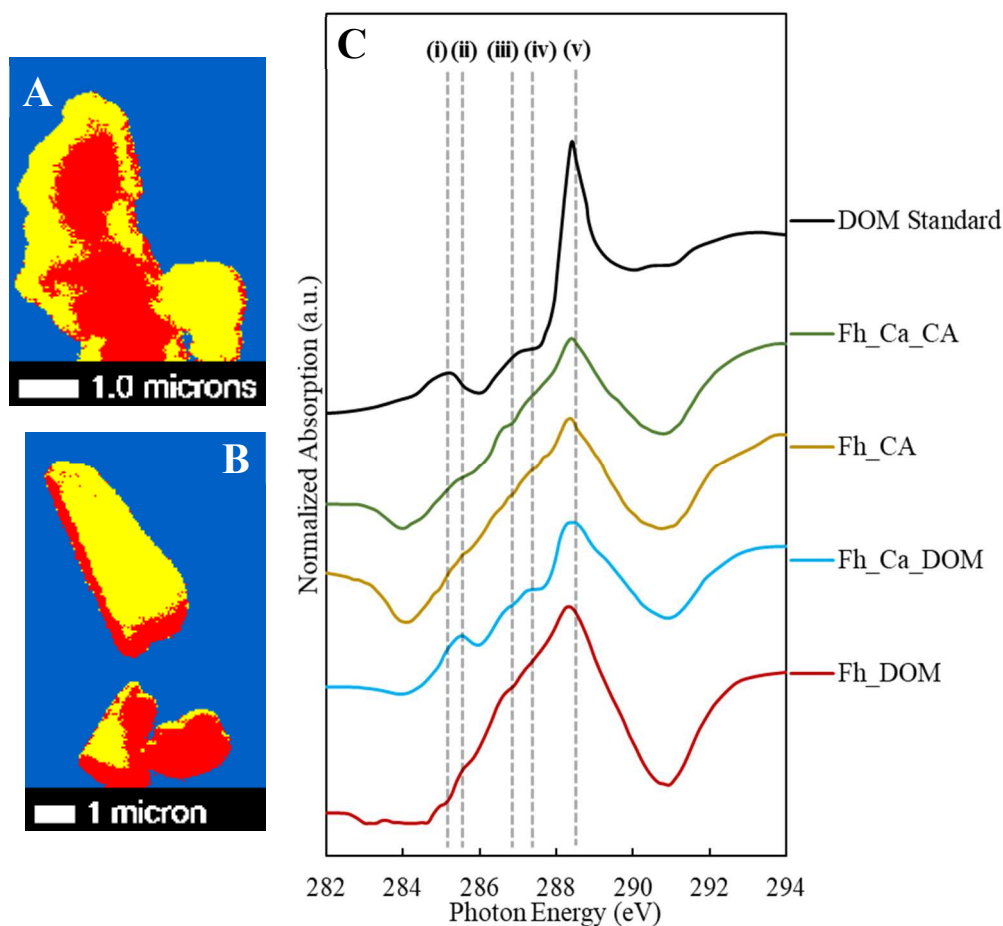


Figure 2.10: C K-edge STXM PCA for ferrihydrite-citric acid and ferrihydrite-Ca-citric acid samples is shown in A and B, respectively. Only one unique cluster was identified for each sample. The region of interest is highlight in yellow in A and in red in B. The contrasting color represent areas of too much sample thickness and were not used in analysis. Corresponding C 1s NEXAFS spectra for A and B are shown in C. Whole sample regions for ferrihydrite-DOM and ferrihydrite-Ca-DOM samples are included as a comparison to citric acid spectra, along with a DOM standard. Peak assignments are located in Table 7.

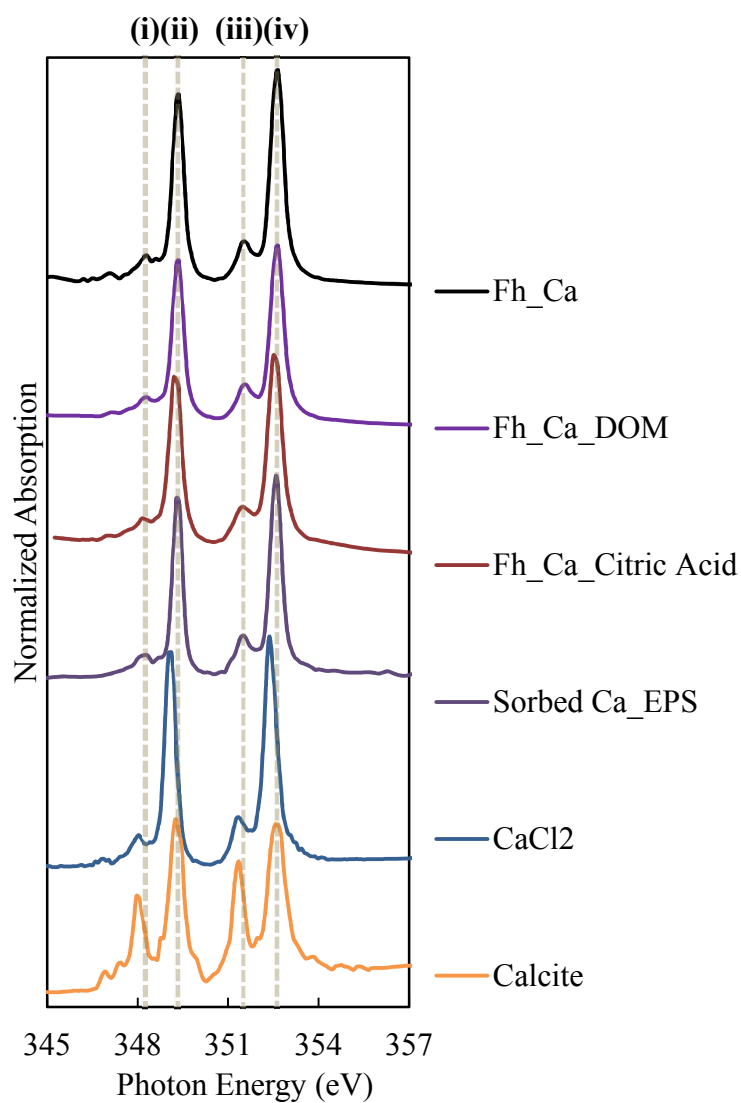


Figure 2.11: Ca 2p NEXAFS spectra for DOM and citric acid samples that were reacted with ferrihydrite in the presence of 30 mM Ca. The samples were compared to a Ca-bearing ferrihydrite standard (Fh\_Ca) synthesized similarly to Fh\_Ca\_DOM and Fh\_Ca\_Citric acid, but in the absence of DOM. Previously published reference standards for Ca sorbed to extracellular polymer structures, CaCl<sub>2</sub>, and calcite are also included.

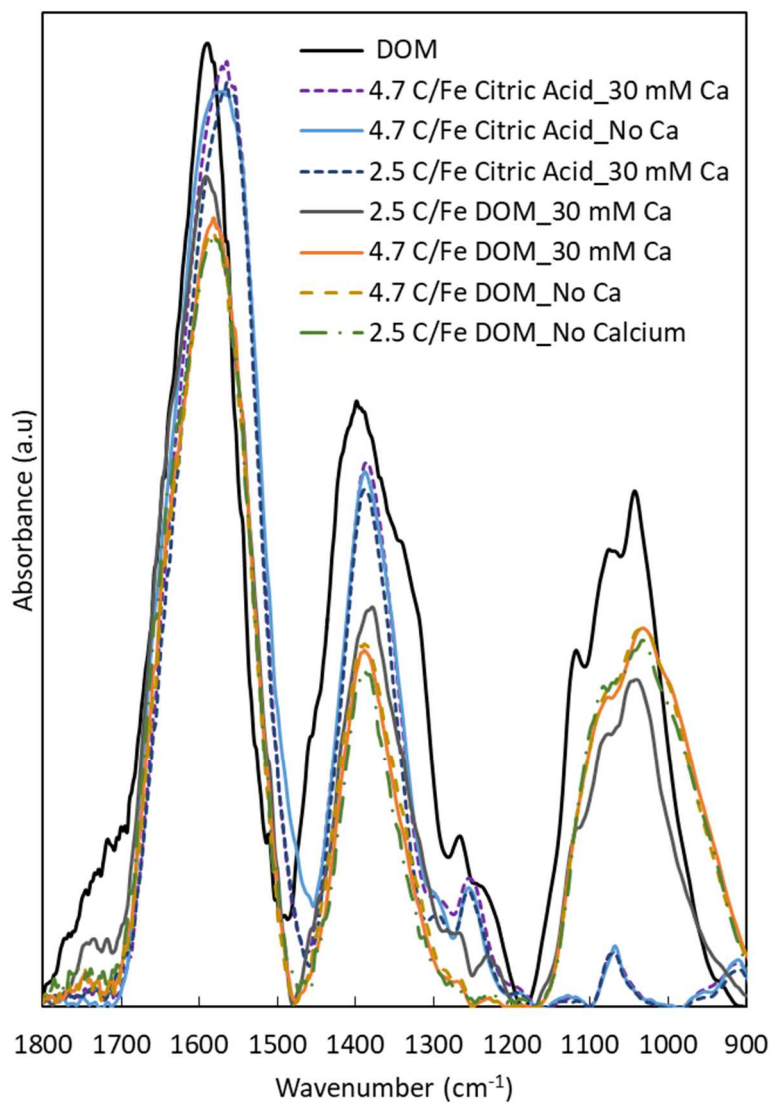


Figure 2.12: ATR-FTIR spectra for ferrihydrate samples reacted with either DOM or citric acid in the absence or presence of Ca. A molar C/Fe ratio of 2.5 or 4.7 was used for DOM samples in order to reveal spectra features that may be difficult to distinguish at high molar C/Fe ratios. A reference standard for the stock DOM used for DOM reactions is also included.

## REFERENCES

- Antelo, J., Arce, F., and Fiol, S. (2015). Arsenate and phosphate adsorption on ferrihydrite nanoparticles. Synergetic interaction with calcium ions. *Chemical Geology* **410**, 53-62.
- Araújo, A., Correia, J., and Soares, C. M. (2015). STXM investigation into effects of CaCl<sub>2</sub> on the hydration of tricalcium silicate and tricalcium aluminate.
- Armbruster, M., Schimmelpfennig, B., Plaschke, M., Rothe, J., Denecke, M., and Klenze, R. (2009). Metal-ion complexation effects in C 1s-NEXAFS spectra of carboxylic acids—evidence by quantum chemical calculations. *Journal of Electron Spectroscopy and Related Phenomena* **169**, 51-56.
- Artz, R. R., Chapman, S. J., Robertson, A. J., Potts, J. M., Laggoun-Défarge, F., Gogo, S., Comont, L., Disnar, J.-R., and Francez, A.-J. (2008). FTIR spectroscopy can be used as a screening tool for organic matter quality in regenerating cutover peatlands. *Soil Biology and Biochemistry* **40**, 515-527.
- Bolster, C. H., and Hornberger, G. M. (2007). On the Use of Linearized Langmuir Equations All rights reserved. No part of this periodical may be reproduced or transmitted in any form or by any means, electronic or mechanical, including photocopying, recording, or any information storage and retrieval system, without permission in writing from the publisher. Permission for printing and for reprinting the material contained herein has been obtained by the publisher. *Soil Science Society of America Journal* **71**.
- Chen, C., Dynes, J. J., Wang, J., Karunakaran, C., and Sparks, D. L. (2014a). Soft X-ray spectromicroscopy study of mineral-organic matter associations in pasture soil clay fractions. *Environmental science & technology* **48**, 6678-6686.
- Chen, C., Dynes, J. J., Wang, J., and Sparks, D. L. (2014b). Properties of Fe-organic matter associations via coprecipitation versus adsorption. *Environmental science & technology* **48**, 13751-13759.

- Chen, C., and Sparks, D. L. (2015). Multi-elemental scanning transmission X-ray microscopy–near edge X-ray absorption fine structure spectroscopy assessment of organo–mineral associations in soils from reduced environments. *Environmental Chemistry* **12**, 64-73.
- Chorover, J., and Amistadi, M. K. (2001). Reaction of forest floor organic matter at goethite, birnessite and smectite surfaces. *Geochimica et Cosmochimica Acta* **65**, 95-109.
- Cismasu, A. C., Michel, F. M., Stebbins, J. F., Levard, C., and Brown, G. E. (2012). Properties of impurity-bearing ferrihydrite I. Effects of Al content and precipitation rate on the structure of 2-line ferrihydrite. *Geochimica et Cosmochimica Acta* **92**, 275-291.
- Cody, G. D., Botto, R. E., Ade, H., Behal, S., Disko, M., and Wirick, S. (1995). Inner-shell spectroscopy and imaging of a subbituminous coal: In-situ analysis of organic and inorganic microstructure using C (1s)-, Ca (2p)-, and Cl (2s)-NEXAFS. *Energy & Fuels* **9**, 525-533.
- Cornell, R. M., and Schwertmann, U. (2003). "The iron oxides: structure, properties, reactions, occurrences and uses," John Wiley & Sons.
- Feng, X., Simpson, A. J., and Simpson, M. J. (2005). Chemical and mineralogical controls on humic acid sorption to clay mineral surfaces. *Organic Geochemistry* **36**, 1553-1566.
- Fu, H., and Quan, X. (2006). Complexes of fulvic acid on the surface of hematite, goethite, and akaganeite: FTIR observation. *Chemosphere* **63**, 403-410.
- Gu, B., Schmitt, J., Chen, Z., Liang, L., and McCarthy, J. F. (1994). Adsorption and desorption of natural organic matter on iron oxide: mechanisms and models. *Environmental Science & Technology* **28**, 38-46.
- Gu, B., Schmitt, J., Chen, Z., Liang, L., and McCarthy, J. F. (1995). Adsorption and desorption of different organic matter fractions on iron oxide. *Geochimica et Cosmochimica Acta* **59**, 219-229.
- Heckman, K., Vazquez-Ortega, A., Gao, X., Chorover, J., and Rasmussen, C. (2011). Changes in water extractable organic matter during incubation of forest floor material in the presence of quartz, goethite and gibbsite surfaces. *Geochimica et Cosmochimica Acta* **75**, 4295-4309.

- Henneberry, Y. K., Kraus, T. E., Nico, P. S., and Horwath, W. R. (2012). Structural stability of coprecipitated natural organic matter and ferric iron under reducing conditions. *Organic geochemistry* **48**, 81-89.
- Hitchcock, A. aXis-2000 is an IDL-based analytical package 2000.
- Jacobsen, C., Wirick, S., Flynn, G., and Zimba, C. (2000). Soft X-ray spectroscopy from image sequences with sub-100 nm spatial resolution. *Journal of Microscopy* **197**, 173-184.
- Jambor, J. L., and Dutrizac, J. E. (1998). Occurrence and constitution of natural and synthetic ferrihydrite, a widespread iron oxyhydroxide. *Chemical Reviews* **98**, 2549-2586.
- Kaiser, K., and Guggenberger, G. (2000). The role of DOM sorption to mineral surfaces in the preservation of organic matter in soils. *Organic geochemistry* **31**, 711-725.
- Kalbitz, K., Solinger, S., Park, J.-H., Michalzik, B., and Matzner, E. (2000). Controls on the dynamics of dissolved organic matter in soils: a review. *Soil science* **165**, 277-304.
- Kleber, M., Eusterhues, K., Keiluweit, M., Mikutta, C., Mikutta, R., and Nico, P. S. (2015). Chapter one-mineral-organic associations: formation, properties, and relevance in soil environments. *Advances in agronomy* **130**, 1-140.
- Kloster, N., and Avena, M. (2015). Interaction of humic acids with soil minerals: adsorption and surface aggregation induced by Ca<sup>2+</sup>. *Environmental Chemistry* **12**, 731-738.
- Kloster, N., Brigante, M., Zanini, G., and Avena, M. (2013). Aggregation kinetics of humic acids in the presence of calcium ions. *Colloids and Surfaces A: Physicochemical and Engineering Aspects* **427**, 76-82.
- Lackovic, K., Johnson, B. B., Angove, M. J., and Wells, J. D. (2003). Modeling the adsorption of citric acid onto Muloorina illite and related clay minerals. *Journal of Colloid and Interface Science* **267**, 49-59.
- Lalonde, K., Mucci, A., Ouellet, A., and G elinas, Y. (2012). Preservation of organic matter in sediments promoted by iron. *Nature* **483**, 198-200.

- Lehmann, J., Kinyangi, J., and Solomon, D. (2007). Organic matter stabilization in soil microaggregates: implications from spatial heterogeneity of organic carbon contents and carbon forms. *Biogeochemistry* **85**, 45-57.
- Lerotic, M., Jacobsen, C., Gillow, J., Francis, A., Wirick, S., Vogt, S., and Maser, J. (2005). Cluster analysis in soft X-ray spectromicroscopy: finding the patterns in complex specimens. *Journal of Electron Spectroscopy and Related Phenomena* **144**, 1137-1143.
- Lock, K., Criel, P., De Schampelaere, K., Van Eeckhout, H., and Janssen, C. (2007). Influence of calcium, magnesium, sodium, potassium and pH on copper toxicity to barley (*Hordeum vulgare*). *Ecotoxicology and environmental safety* **68**, 299-304.
- Michel, F. M., Ehm, L., Antao, S. M., Lee, P. L., Chupas, P. J., Liu, G., Strongin, D. R., Schoonen, M. A., Phillips, B. L., and Parise, J. B. (2007). The structure of ferrihydrite, a nanocrystalline material. *Science* **316**, 1726-1729.
- Mikutta, R., Mikutta, C., Kalbitz, K., Scheel, T., Kaiser, K., and Jahn, R. (2007). Biodegradation of forest floor organic matter bound to minerals via different binding mechanisms. *Geochimica et Cosmochimica Acta* **71**, 2569-2590.
- Obst, M., Dynes, J., Lawrence, J., Swerhone, G., Benzerara, K., Karunakaran, C., Kaznatcheev, K., Tyliszczak, T., and Hitchcock, A. (2009). Precipitation of amorphous CaCO<sub>3</sub> (aragonite-like) by cyanobacteria: a STXM study of the influence of EPS on the nucleation process. *Geochimica et Cosmochimica Acta* **73**, 4180-4198.
- Plaschke, M., Rothe, J., Altmaier, M., Denecke, M. A., and Fanghänel, T. (2005). Near edge X-ray absorption fine structure (NEXAFS) of model compounds for the humic acid/actinide ion interaction. *Journal of electron spectroscopy and related phenomena* **148**, 151-157.
- Politi, Y., Metzler, R. A., Abrecht, M., Gilbert, B., Wilt, F. H., Sagi, I., Addadi, L., Weiner, S., and Gilbert, P. (2008). Transformation mechanism of amorphous calcium carbonate into calcite in the sea urchin larval spicule. *Proceedings of the National Academy of Sciences* **105**, 17362-17366.
- Post, W. M., and Kwon, K. C. (2000). Soil carbon sequestration and land use change: processes and potential. *Global change biology* **6**, 317-327.

- Redman, A. D., Macalady, D. L., and Ahmann, D. (2002). Natural organic matter affects arsenic speciation and sorption onto hematite. *Environmental Science & Technology* **36**, 2889-2896.
- Schneider, M., Scheel, T., Mikutta, R., Van Hees, P., Kaiser, K., and Kalbitz, K. (2010). Sorptive stabilization of organic matter by amorphous Al hydroxide. *Geochimica et Cosmochimica Acta* **74**, 1606-1619.
- Shaker, A. M., Komy, Z. R., Heggy, S. E., and El-Sayed, M. E. (2012). Kinetic study for adsorption humic acid on soil minerals. *The Journal of Physical Chemistry A* **116**, 10889-10896.
- Solomon, D., Lehmann, J., Harden, J., Wang, J., Kinyangi, J., Heymann, K., Karunakaran, C., Lu, Y., Wirick, S., and Jacobsen, C. (2012). Micro-and nano-environments of carbon sequestration: Multi-element STXM–NEXAFS spectromicroscopy assessment of microbial carbon and mineral associations. *Chemical geology* **329**, 53-73.
- Sowers, T., Adhikari, D., Wang, J., Yang, Y., and Sparks, D. L. (2018a). Spatial associations and chemical composition of organic carbon sequestered in Fe, Ca, and organic carbon ternary systems. *Environmental science & technology*.
- Sowers, T. D., Stuckey, J. W., and Sparks, D. L. (2018b). The synergistic effect of calcium on organic carbon sequestration to ferrihydrite. *Geochemical transactions* **19**, 4.
- Sparks, D. L. (2003). "Environmental soil chemistry," Academic press.
- Sposito, G. (2008). "The chemistry of soils," Oxford university press.
- Stevenson, F. J. (1994). "Humus chemistry: genesis, composition, reactions," John Wiley & Sons.
- Stuckey, J. W., Goodwin, C., Wang, J., Kaplan, L. A., Vidal-Esquivel, P., Beebe, T. P., and Sparks, D. L. (2018). Impacts of hydrous manganese oxide on the retention and lability of dissolved organic matter. *Geochemical transactions* **19**, 6.

- Tessier, A., Fortin, D., Belzile, N., DeVitre, R., and Leppard, G. (1996). Metal sorption to diagenetic iron and manganese oxyhydroxides and associated organic matter: narrowing the gap between field and laboratory measurements. *Geochimica et Cosmochimica Acta* **60**, 387-404.
- Wagai, R., and Mayer, L. M. (2007). Sorptive stabilization of organic matter in soils by hydrous iron oxides. *Geochimica et Cosmochimica Acta* **71**, 25-35.
- Wan, J., Tyliszczak, T., and Tokunaga, T. K. (2007). Organic carbon distribution, speciation, and elemental correlations within soil microaggregates: applications of STXM and NEXAFS spectroscopy. *Geochimica et Cosmochimica Acta* **71**, 5439-5449.
- Waychunas, G., Rea, B., Fuller, C., and Davis, J. (1993). Surface chemistry of ferrihydrite: Part 1. EXAFS studies of the geometry of coprecipitated and adsorbed arsenate. *Geochimica et Cosmochimica Acta* **57**, 2251-2269.
- Weng, L. P., Koopal, L. K., Hiemstra, T., Meeussen, J. C., and Van Riemsdijk, W. H. (2005). Interactions of calcium and fulvic acid at the goethite-water interface. *Geochimica et Cosmochimica Acta* **69**, 325-339.

## Chapter 3

### NATURALLY-OCCURRING BACTERIOGENIC IRON OXIDES: AN UNDERSTUDIED, UNIQUE ORGANIC MATTER SINK

#### 3.1 Introduction

Among terrestrial and aquatic systems, iron (Fe) (oxyhydr)oxides play a primary role in driving the chemical processes mediating organic matter (OM) cycling (Davis, 1982; Gu et al., 1994; Jambor and Dutrizac, 1998; Schmidt et al., 2011). Iron (oxyhydr)oxides, especially those of poor crystallinity and high surface area (i.e., 2-line ferrihydrite), are environmentally ubiquitous sorbents of OM typically having a maximum sorption capacity exceeding other major sorbents (i.e., clay aluminosilicates) (Chorover and Amistadi, 2001; Kaiser and Guggenberger, 2000; Meier et al., 1999). Sequestration of OM in Fe (oxyhydr)oxide sorption complexes and coprecipitates increases stability of OC moieties (Chen et al., 2014b; Davis, 1982; Kleber et al., 2015), impacting nutrient cycling of surrounding biota, mitigation of C release to the atmosphere as greenhouse gases (i.e., CO<sub>2</sub>), and metal(loid) contaminant mobility (Amundson, 2001; Bolan et al., 2011; Chakraborty et al., 2014; Grafe et al., 2001; Schmidt et al., 2011). Dissolved organic matter (DOM) represents a chemically active fraction of OM that contains diverse organic carbon (OC) functional moieties that are instrumental to OM-stabilizing organo-mineral associations in soil and water systems. However, research investigating Fe oxide-mediated DOM cycling has

largely focused on synthetically-produced analogues or abiotically-derived phases (Chen et al., 2014b; Gu et al., 1994; Gu et al., 1995; Kaiser and Guggenberger, 2000; Kaiser and Guggenberger, 2003; Mikutta et al., 2007). Currently, limited research exists on naturally-occurring Fe (oxyhydr)oxides formed in stream water systems, with one study focusing on Fe mineral precipitation at the confluence of an acidic and pristine stream (McKnight et al., 1992), likely driven by abiogenic processes. Bacteriogenic Fe (oxyhydr)oxides (BIOs) possess an unknown potential to participate in the biogeochemical cycling of DOM due to their high surface reactivity for oxyanions, unique morphological characteristics, and inherently surface-aggregated and/or incorporated OM from biogenic-facilitated coprecipitation. Therefore, we investigated the role of naturally-occurring BIOs, formed in suboxic interfaces at circumneutral pH, on DOM cycling.

Bacteriogenic Fe (oxyhydr)oxides are commonly found in quiescent waterways and oxygen-limited sediments, forming typically as an Fe-dominated biogenic Fe-OM coprecipitate at the suboxic interface at which Fe(II)-rich groundwater meets aerobic, circumneutral surface water systems (Figure 3.1A) (Duckworth et al., 2009; Emerson and Weiss, 2004; Ferris, 2005). A variety of Fe-oxidizing bacteria (FeOB) may proliferate at this suboxic zone and oxidize Fe(II) to derive chemical energy via chemolithotrophy (Duckworth et al., 2009; Emerson and Moyer, 1997; Emerson and Weiss, 2004). Microbial mats and a corresponding Fe(III)-mineral sheen overlaying the water's surface form as a byproduct of this oxidative process (Figure 3.2), consisting primarily of biomass rich with BIOs morphologically unique to the respective FeOB (Figure 3.3) (Chan et al., 2009; Emerson et al., 2010).

Rhizosphere and wetland systems have also been found to commonly promote BIO formation (Emerson et al., 2010), and may represent an important contributor to the biogeochemistry of poorly crystalline Fe (oxyhydr)oxides in soils and sediments; however, the proportion of BIOs to abiogenic phases is currently unknown.

Bacteriogenic Fe (oxyhydr)oxide phases possess lower crystallinity, smaller crystal domain size, and lower surface area compared to abiogenic short-range-ordered Fe (oxyhydr)oxides, leading to BIOs having variable sorption affinity for oxyanions such as arsenate, phosphate, and chromate compared to synthetic analogues (Cismasu et al., 2011; Ferris, 2005; Rentz et al., 2009; Sowers et al., 2017; Whitaker et al., 2018). Also, BIOs have been found to adversely affect the efficiency of select arsenic filtration and was attributed to differences in surface charge (Kleinert et al., 2011), signifying the importance of BIO chemical and physical characterization to sorptive reactivity. Cell-derived OM is incorporated into BIOs and surface aggregated to the Fe(III) biomineral upon formation (Muehe et al., 2013) and, in a handful of studies, has been found to dominantly consist of lipid and polysaccharide moieties (Chan et al., 2009; Miot et al., 2009a; Miot et al., 2009b). The incorporation and/or surface aggregation of this “native” OM may have significant impacts on surface area, mineral charge, and ligand availability on the sorbent surface, making BIOs unique from abiogenic Fe mineral phases of short-range-order (i.e., abiogenic 2-line ferrihydrite); however, little is known about OM speciation of naturally-occurring BIOs and the potential of BIOs to sorb DOM.

To begin the first steps towards elucidating the complex sorption interactions of OM and naturally-forming BIOs, we utilize batch, spectroscopic, and spectrometric

experiments to probe the potential for locally-collected stream water BIOs to sorb DOM from a compositionally relevant and well-characterized leaf litter source from Stroud Water Research Center (Chen et al., 2014b; Chen et al., 2015; Sowers et al., 2018; Stuckey et al., 2018), and Suwannee River Fulvic and Humic Acid standards (SRFA and SRHA, respectively). Leaf litter-derived DOM is chemically diverse and widely used DOM source that encompasses a broad range of OC moieties that BIOs may encounter in variable formation environments (Chen et al., 2014b; Sowers et al., 2018; Stuckey et al., 2018). We initially posited that OM would load to an extent that is equivalent or greater than 2-line ferrihydrite, a chemically and physically different abiotic mineral phase that shares similar amorphous structure, and that carboxylic moieties are largely responsible for OM sequestration. Batch reaction data were paired with scanning transmission X-ray microscopy-near edge X-ray absorption fine structure (STXM-NEXAFS) spectroscopy, attenuated total reflectance-Fourier transform infrared (ATR-FTIR) spectroscopy, and Fourier transform ion cyclotron resonance mass spectrometry (FT-ICR-MS) data to provide the first novel insight into OM moiety interactions with a naturally-formed BIO. This investigation introduces the concept of natural BIOs as a sorbent of unique reactivity and has potential implications toward water filtering efficiency, nutrient cycling, and contaminant transport.

## **3.2 Materials and Methods**

### **3.2.1 Dissolved Organic Matter Extraction and Characterization**

A DI water leaf litter extraction was used to collect DOM for all sorption reactions. Environmental DOM is inherently heterogeneous and diverse in composition (Bauer and Bianchi, 2011; Bolan et al., 2011); however, we chose to use a well-characterized DOM source consisting of a range of OC moieties in order to identify an applicable baseline for the potential of BIOs to sorb OM. Leaf litter was collected from the Stroud Water Research Center (Avondale, PA), the same source used in investigations of organo-mineral interactions of Fe (oxyhydr)oxides and DOM by Chen et al. (2014), Stuckey et al. (2018), and Sowers et al (2018). Samples were collected from the top 10 cm of leaf litter from a forest soil O<sub>a</sub> horizon (Typic Hapludult). Using a previously established method by the authors (Chen et al., 2014b; Sowers et al., 2018), leaf litter was mixed with DI water (1:2 fresh leaf litter:DI water [w/w]). The resulting suspension was then placed on an IKA Labortechnik KS501 rotary platform shaker at 200 rpm for 90 hours to extract OC. Upon completion, the resulting solution was centrifuged (20,000 g for one hour) and sequentially vacuum filtered through Sterlitech polyethersulfone (PES) filters of 0.80 μm, 0.45 μm, and 0.20 μm pore size. All sorption reactions were completed after filtration, with remaining DOM stock being stored at -4 °C. The filtered DI-extractable DOM solution was then analyzed using a Total Organic Carbon (TOC) analyzer (Apollo 9000 series) to determine OC concentration (Table 3.1). A metal/metalloid elemental analysis of the DOM solution was performed using inductively coupled plasma-atomic emission (ICP-AES) (Table 3.1). Chemical composition of DOM was also classified

using FT-ICR-MS analyses and discussed in later sections and SI (Table 3.2, 3.3, & 3.4).

### **3.2.2 Collection of Bacteriogenic Iron Oxides**

Submerged biofilm/mineral assemblage mats characteristic of BIOs (Figure 3.2) were all collected at the first sign of formation (16 hours after a rainfall event) in order to limit sorption of allochthonous OM sources and from the same location (39° 41'56"N 75° 45'09"W) at White Clay Creek (Newark, Delaware) (Emerson et al., 2010; Sowers et al., 2017; Whitaker et al., 2018), where BIOs forms perennially at circumneutral pH (~6.5). Collected material was presumed to be BIOs upon collection due to similarities to other BIO mats studied previously (Duckworth et al., 2009; Emerson et al., 2010; Sowers et al., 2017; Whitaker et al., 2018; Whitaker and Duckworth, 2018), but was also expected to contain other components (i.e., quartz) to a minor degree due to the natural condition of the sample. Submerged mineral assemblages in the water column were sampled via methods previously established by the authors (Sowers et al., 2017). Suspended BIOs were collected via syringe and transferred into 1-liter polypropylene containers. Suspensions were immediately taken to the laboratory, transferred to 250 mL polypropylene centrifuge containers and centrifuged (Thermo Scientific Legend XTR) for 15 minutes at ca. 10,000 g (RCF). This process was repeated multiple times until a well-mixed, pooled BIOs stock was obtained and stored as a frozen wet paste at approximately -4°. Three 15 mg subsamples from the BIOs stock were dried at 70°C for approximately 12 hours prior to beginning all batch experiments to determine dry mass percent. This was performed

to ensure consistency when conducting all batch experiments with wet BIOs. Additionally, elemental composition, zeta potential, and surface area were analyzed (Table 3.1). Collected BIOs were not subjected to sterilization techniques prior to sorption or desorption experiments.

### **3.2.3 Characterization of BIOs**

X-ray diffraction (XRD) and Brunauer–Emmett–Teller (BET) analysis were performed to determine BIOs Fe mineral phase and external surface area, respectively. A Bruker D8 Discover diffractometer was used to perform XRD analysis. BIOs was freeze-dried prior to analysis and analyzed from  $10^{\circ}$  to  $80^{\circ}$   $2\theta$  (step size  $0.05^{\circ}$   $2\theta$ ) and subsequently compared to a synthetic 2-line ferrihydrite diffractogram collected previously by the authors. The analysis confirmed BIOs to largely consist of 2-line ferrihydrite, with the minor presence of quartz grains (Figure 3.4) (Sowers et al., 2018). BET analysis was performed for BIOs using a Micromeritics ASAP 2020 (Table 3.1). Zeta potential of BIOs and DOM at pH 6.5 was determined using Malvern: Model Zetasizer Nano ZS in order to determine potential electrostatic differences (Table 3.1). A vario Micro cube CHNS analyzer was used to determine solid phase C and sulfur concentrations. A subsample of BIOs stock (20 mg) were digested using *aqua regia* (3:1 molar ratio of HCl and HNO<sub>3</sub>) and measured for metal and metalloid concentrations (Table 3.1) using ICP-AES.

Bacteriogenic Fe (oxyhydr)oxides collected in natural aqueous systems containing “fluffy” biofilm/mineral assemblage mats (Figure 3.2) has been characterized extensively in the past ten years (Chan et al., 2009; Duckworth et al.,

2009; Ferris, 2005; Fortin and Langley, 2005; Rentz et al., 2009; Sowers et al., 2017). Our reported SEM and STXM-NEXAFS analyses provide convincing evidence that our collected biomass from similar circumneutral waterways is predominately BIOs. Specifically, SEM and STXM-NEXAFS (Figure 3.3 & 3.4) analyses reveals the presence of sheath/rod-like morphologies that are rich in Fe and C (possessing associated cell-derived OM). These microscopic and spectroscopic results compare well to other studies of natural BIOs conducted by Fortin and Langley (2005) and Chan et al. (2009). However, additional elements are expected to present as well due to these being environmentally collected samples, which are reported in Table 3.1. Abiotic Fe(III) (oxyhydr)oxides may be a component of the collected BIOs; however, our microscopic and spectroscopic results, compared to that of others, indicate our samples are dominantly biogenic.

#### **3.2.4 Scanning Transmission X-ray Microscopy**

STXM-NEXAFS data was collected at Beamline 10ID-1 at the Canadian Light Source (Saskatoon, Saskatchewan) was used to collect STXM-NEXAFS data for BIO samples. Samples were prepared accordingly to methodology previously utilized by the authors (Chen et al., 2014a; Sowers et al., 2018). A subsample of BIO wet-paste was suspended in DI water such that approximately 0.5 mg of sample was suspended with 1 mL DI water and mixed well. Approximately 3  $\mu$ L of the suspension was transferred to a Si<sub>3</sub>N<sub>4</sub> window and allowed to air-dry for approximately 30 minutes before being placed on the STXM sample mount. The STXM chamber was pumped to rough vacuum and then backfilled with 1/6 atmosphere He for all measurements. A

maximum spatial resolution of approximately 30 nm was achieved using a Fresnel zone plate. Dwell time equaled 1 ms with a pixel size of approximately 40 nm for all measurements taken.

C 1s and Fe 2p data was obtained by raster scanning from 280 to 735 eV (125 X 125 pixels) at specific regions of interest identified at low magnification (up to approximately 2000  $\mu\text{m}^2$ ) at the C K-edge (288 eV). Image stacks were generated for each element across the aforementioned eV range and averages of these stacks at specific eV ranges (Table 3.5) were then used when processing collected STXM-NEXAFS data.

### **3.2.5 STXM-NEXAFS Data Processing**

All data stacks were aligned using Stack Analyze (Stony Brook, V2.7) and processed using the aXis2000 software package.(Hitchcock et al., 2012; Jacobsen et al., 2000) PCA and cluster analysis was performed using PCA GUI 1.1.1 software (Lerotic et al., 2005). After alignment and identifying  $I_0$  (incident flux), aXis2000 was used to convert aligned and stacked image data to optical density using the following equation:  $OD = \ln(I_0/I)$ , where  $I$  is equal to the flux transmitted through the sample. Generated images up to  $\pm 0.5$  eV of the resonance energy for each element were averaged for chemical mapping. The averaged images at each element's resonance energies were subtracted with averaged images at the elements' specific pre-edge range (Table 3.2) in order to obtain chemical maps.

### **3.2.6 Desorption of Native Organic Carbon**

Desorption experiments using untreated BIOs were performed to elucidate the chemical stability of native OC (cell-derived OM and/or OC already associated with BIOs upon collection; Figure 3.3) present in/on BIOs. Desorbing reagents commonly used when assessing OC sequestration to metal oxide minerals were reacted with BIOs at circumneutral pH and include the following: DI water (control), 0.1 M NaCl, 0.5 M NaCl, 0.1 M NaH<sub>2</sub>PO<sub>4</sub>, and 1.0 M NaH<sub>2</sub>PO<sub>4</sub>. 200±3 mg of BIOs (dry mass basis) were reacted with 200 mL of desorbing reagent at the initiation of the experiment. Samples were placed on an IKA Labortechnik KS501 rotary platform shaker (180 rpm) and reacted in the dark for 24 hours. Upon reaction completion, the suspension was sampled using a 10 mL BD brand syringe with Luer-Lok™ tips to which a 0.20 µm Cole-Parmer PES syringe filter was affixed. Aqueous samples were analyzed using a total organic carbon (TOC) analyzer (Apollo 9000HS) to determine the extent to which native OC was desorbed from BIOs. A vario Micro cube CHNS analyzer was used to measure solid phase C concentration for a subset of reacted samples and confirmed C concentration decrease in the solid phase was equivalent to the concentration of aqueous OC measured.

### **3.2.7 Sorption of Organic Matter and Humic Standards to Bacteriogenic Iron Oxides**

A sorption isotherm was performed to measure the capacity of BIOs for OM sequestration at circumneutral pH. 40.0 ± 1.8 mg (dry mass basis) of BIOs as a wet paste were transferred to 50 mL polypropylene centrifuge tubes and suspended in a mixture of DOM and DI solution such that the final volume equaled 40 mL. DOM and

DI water were mixed such that initial OC concentrations were 0, 25, 50, 100, 200, 300, 400, 600, 800, 1000, or 1200 mg L<sup>-1</sup> performed in triplicate (5 to 20 mg OC L<sup>-1</sup> data provided in SI). Three DI water controls and DOM-only controls (containing only 1200 mg OC L<sup>-1</sup>) were used throughout. Suspensions were adjusted to pH 6.5 ± 0.15 via addition of NaOH and/or HCl. Reactors were mixed on a Fischer Scientific Multi-Purpose Tube Rotator (40 rpm) and reacted for 24 hours (dark) at 25 °C. pH was monitored intermittently to ensure pH remained at approximately 6.5 ± 0.15. After reaction completion, suspensions were filtered through a 0.20 µm PES syringe filter and diluted to a 1:4 ratio. Solutions were then analyzed using a total organic carbon (TOC) analyzer (Apollo 9000HS) analyzer, with quantity of OC sorbed being determined by measuring the difference in aqueous OC concentration before and after sorption. A vario Micro cube CHNS analyzer was used to measure solid phase C concentration for a subset of reacted samples and confirmed C concentration increase on the solid phase was equivalent to the decrease in aqueous OC measured. In addition, no changes in C concentration for DI water controls or DOM controls were detected over the 24 hr reaction. This method was repeated for Suwannee River Fulvic Acid Standard II (SRFA, 2S101F) and Suwannee River Humic Acid Standard II (SRHA, 2S101H), obtained from the International Humic Substances Society (IHSS).

DOM, SRFA, and SRHA complexed with BIOs were reacted with desorbing reagents to determine the chemical stability of sorbed OM. 15 mg of BIOs previously reacted with initial OC concentrations of 100, 300, 600, or 1000 mg OC L<sup>-1</sup> (800 mg OC L<sup>-1</sup> performed instead for SRFA and SRHA) was equilibrated with 10 mL of 0.1 M NaCl or 0.1 M H<sub>2</sub>PO<sub>4</sub> at circumneutral pH for 24 hours (dark). The solutions were

then prepared for TOC and CHNS analysis using methods similar to the procedure outlined for sorption experiments.

### **3.2.8 Fourier Transform-Ion Cyclotron Resonance-Mass Spectrometry Analysis**

DOM stock (initial OC concentration of 200 mg L<sup>-1</sup>) and DOM after reaction with BIOs were analyzed (three analytical replicates analyzed for each) using FT-ICR-MS to elucidate differences in OC molecular composition before and after sorption. A low initial OC concentration, relative to the isotherm experiment, was chosen to increase our ability to discern changes in OC speciation in solution before and after reaction (sorption of 46.1 ± 4.6 mg OC g<sup>-1</sup> BIOs) with BIOs. Samples were prepared according to solid phase extraction (SPE) methods presented in Dittmar et al (2008). Solutions were diluted to approximately 100 mg OC L<sup>-1</sup> with mass spectrometry (MS) grade water and 24 mL was gravity-passed through primed Agilent PPL™ 100 mg resin cartridges, such that 2.4 mg OC were loaded onto 100 mg of resin for all samples. The adsorbed OM was eluted with 1 mL MS grade methanol. The extracts were characterized using negative ion mode electrospray ionization with a 12 T Bruker Daltonics Apex Qe FT-ICR-MS instrument at the COSMIC facility at Old Dominion University. To increase the ionization efficiency, ammonium hydroxide was added immediately prior to ESI to raise the pH to 8. Samples were introduced by a syringe pump providing an infusion rate of 120 µL h<sup>-1</sup> and analyzed in negative ion mode with electrospray voltages optimized for each sample. Ions (in the range of 200–2000 m/z) were accumulated in a hexapole for 1.0 s before being transferred to the ICR cell. Exactly 300 transients, collected with a 4 MWord time domain, were added

for a total run time of ~30 min. The summed free induction decay signal was zero-filled once and Sine-Bell apodized prior to fast Fourier transformation and magnitude calculation using the Bruker Daltonics Data Analysis software. Prior to data analysis, all samples were externally calibrated with a polyethylene glycol standard and internally calibrated with naturally present fatty acids and other compounds containing a +CH<sub>2</sub> homologous series within the sample. Further methodology concerning SPE extraction and spectral post-processing are discussed in detail in the SI, with compound classes being assigned via similar methodology for all samples.

### 3.2.9 Spectral Post-Processing

Data analysis was performed according to methods outlined in Ohno et al. (2014) and Coward et al. (2018). Before assignment, only peaks present in at least two out of the three analytical replicates were selected for further post-processing. For assignments of molecular formulas, only  $m/z$  values with a signal to noise (S/N) ratio above 5 (peak detection and relative peak magnitude highly reproducible when conservative S/N thresholds are used) (Sleighter et al., 2012) were assigned using the formula extension approach (Kujawinski and Behn, 2006; Ohno and Ohno, 2013), using combinations of C (8–50 atoms), H (8–100 atoms), O (1–30 atoms), N (0–5 atoms), S (0–3 atoms), and P (0–2 atoms) as limiting atomic values. All peaks were assigned based on identical  $m/z$ . The resulting list was constrained to chemically feasible organic matter formulae using the following criteria:  $O/C \leq 1.2$ ,  $H/C \leq 2.25$ ,  $H/C \geq 0.3$ ,  $N/C \leq 0.5$ ,  $S/C \leq 0.2$ ,  $P/C \leq 0.1$ ,  $(S + P)/C \leq 0.2$ , double bond equivalency

(DBE)  $\geq 0$ , and must be a whole number. DBE was calculated using the following equation (Koch and Dittmar, 2006a):

$$\text{DBE} = 1 + (2c - h + n)/2$$

where c, h, and n refer to the stoichiometric numbers of carbon, hydrogen, and nitrogen atoms per formula, respectively. The  $^{13}\text{C}$  containing isotopic peaks which would appear exactly 1.0034 m/z units higher and <50 % relative peak magnitude than the  $^{12}\text{C}$ -containing peak were removed from the peak list since they give redundant molecular information.

The Kendrick mass defect (KMD) analysis is a chemically meaningful method to determine appropriate formula assignment (Ohno and Ohno, 2013). Molecules of a homologous series differing only in the number of  $\text{CH}_2$  groups have the same KMD value. If the chemical formula of one molecule in the series can be determined, then the formula for the entire series can be inferred. Thus, if one of the potential formulae for a higher m/z peak shares a KMD value with a peak in the lower m/z region where unique formula assignments are possible, the formula with the shared KMD is the correct assignment. The Kendrick mass and KMD of the feasible molecules were calculated as:

$$\text{Kendrick mass} = \text{IUPAC mass} \times (14.00000/14.01565)$$

$$\text{KMD} = \text{nominal Kendrick mass} - \text{Kendrick mass}$$

where nominal Kendrick mass was the integer value of the observed mass. A MATLAB script was used to select the most appropriate molecular formula by parsing the proposed formulae into two arrays, those with unique formula assignments and those with two or more potential formula assignments. The hierarchy for determining

the correct assignment was selection based on (1) KMD analysis, (2) least number of non-oxygen heteroatoms, and (3) lowest ppm m/z deviation (Kujawinski and Behn, 2006). The script calculated additional descriptors for each formula: O/C ratio, H/C ratio, DBE, and DBE/C. The script also parsed the assigned peaks into the appropriate van Krevelen space which consisted of six discrete regions, relying on the modified aromaticity index ( $AI_{mod}$ ) calculation derived by Koch and Dittmar (Koch and Dittmar, 2006b): (1) polycyclic aromatic (PCA) formulas ( $AI_{mod} > 0.66$ ), (2) aromatic formulas ( $0.66 \geq AI_{mod} > 0.50$ ), (3) lignin/phenolic formulas ( $AI_{mod} \leq 0.50$  and  $H/C < 1.5$ ), (4) nitrogen-less aliphatic (Aliphatic\_No N) compounds ( $2.0 > H/C \geq 1.5$  and  $N=0$ ), (5) nitrogen-containing aliphatic (Aliphatic\_N) compounds ( $2.0 > H/C \geq 1.5$  and  $N > 0$ ) and (6) carbohydrate-like compounds ( $H/C \geq 2.0$  or  $O/C \geq 0.9$ ).

The formula calculations were done sequentially by using the peak list obtained from the instrument and initially assigning formulae for CHO-containing components. The peaks which were assigned as CHO components were then removed from the initial peak list and the resulting reduced peak list was used for calculating formulae containing CHON. The removal of assigned peaks and next sequential assignment calculations were conducted in the order of CHOS, CHOP, CHONS, CHONP, CHOSP, and CHONSP. The removal of peaks that have been assigned ensures the most robust formula assignment since the calculations were constrained to only the selected elements present in the formula. Thus, once assigned the peaks were not subject to reassignment later when calculating molecular formulae containing additional elements.

### 3.2.10 Intensity-Normalized Quantification of Adsorption and Relative Abundance

A relative intensity index approach, previously described in Avneri-Katz et al. (2017) and Coward et al. (2018), was used to categorize sorption of DOM to BIOs into total, partial and no sorption. Post-sorption peak intensity (BIO<sub>200</sub>) was compared to the peak intensity of the unexposed DOM before sorption, expressed as a scale ranging from 0 to 1. Formulae with index values of 1.00 or greater, in which >1 values are likely derived from variation in ionization efficiency, have been deemed unadsorbed. Formulae with values between 1 and 0 were deemed partially adsorbed, with the index value indicative of the degree of adsorption. Formulae with index values of 0 were below the S/N threshold of 5 post-exposure to BIOs and were operatively deemed “completely sorbed”. This relative intensity index was set to a color bar in Figure 3.4B for visual depiction of the degree of sorption.

Changes in relative abundance ( $\Delta$  %) of compound classes (Figure 3.13) were parsed by formulae O content (O#), in which the abundance of post-sorption formulae in each compound class and O# were compared to that observed in initial, unexposed DOM. The relative abundances of formulae within each O number and compound class found for the initial DOM was then subtracted from the BIO<sub>200</sub> normalized relative abundances, resulting in a  $\Delta$  % value. Positive percentages in Figure 3.13 correspond to enrichment as a result of high sorption of other compounds or as release of native OC from BIO. Negative percentages indicate relative sorption to BIOs.

### **3.2.11 Attenuated Total Reflectance-Fourier Transform Infrared Spectroscopy**

Freeze-dried DOM, BIO, and BIO reacted with leaf litter DOM, SRFA, or SRHA were analyzed using a Bruker ATR-FTIR and methodology used by Chen et al. (2014b) and Sowers et al. (2018). All OM-sorbed samples were reacted with the same initial OC concentration (200 mg OC L<sup>-1</sup>). Spectra were scanned from 4000 to 600 cm<sup>-1</sup> at a spectra resolution of 2 cm<sup>-1</sup>. Automatic baseline correction and normalization was applied to all spectra. All samples were dried and analyzed immediately to avoid the effects of moisture uptake on sample spectra. The OPUS Version 7.2 spectroscopy software suite (Bruker) was used to process all collected spectra.

## **3.3 Results and Discussion**

### **3.3.1 Investigating BIO Morphology and Native Organic Carbon Chemistry**

BIOs morphology and elemental composition were analyzed using X-ray diffraction (XRD), scanning electron microscopy (SEM), and STXM-NEXAFS to probe BIOs chemical and physical characteristics. BIO was found to be short-range-ordered via XRD (Figure 3.4), with the beat scattering pattern correlating well to our synthesized synthetic 2-line ferrihydrite standard. Emergence of a broad peak was observed from 20 to 30° 2 $\theta$ , representative of native OM (OM originally present in/to BIOs upon collection; Figure 3.3) associated with BIOs,(Eusterhues et al., 2008) and the diffractogram was similar to data collected for ferrihydrite-DOM coprecipitates with 2.8 and 5.6 C/Fe molar ratios (Chen et al., 2014b). SEM revealed BIOs have sheath morphology surrounded by aggregated native OM (Figure 3.3). Sheath-like morphologies are widely known to be characteristic of BIOs produced by the Fe-

oxidizing bacteria *Leptothrix* (Chan et al., 2009; Emerson and Weiss, 2004).

Investigating these morphological characteristics further using STXM, we observed that BIOs sheaths consisted of a network of highly-correlated C and Fe (with stronger Fe signal), exhibited by a dark shade of purple (C and Fe represented as red and blue, respectively) in a color-coded composite map (Figure 3.5A). Sheaths were found to be outlined in red, suggesting the surface occlusion of C on the Fe-C BIOs sheath. The sheath-like morphology, 2-line ferrihydrite mineral phase, and elemental associations of Fe and C are well related to other studies investigating the occurrence of laboratory-synthesized and natural BIOs (Chan et al., 2009; Fortin and Langley, 2005; Miot et al., 2009a; Miot et al., 2009b), providing significant support that collected samples are Fe(III) biominerals.

We paired STXM with NEXAFS analysis to investigate the spatial heterogeneity of OM chemical moieties of BIOs (Figure 3.5B). For both the exterior of the sheath surface (R1), expected to possess surface aggregated native OM, and the poorly-crystalline Fe-biomineral sheath (R2 & R3), we found that carboxylic (288.5 eV) and aromatic (285.4-285.6 eV) OC moieties (Chen et al., 2014a; Sowers et al., 2018) were the dominant species for all regions. However, aliphatic groups were found to be primarily concentrated in the exterior R1, indicated by shoulder emergence at 287.4 eV and the broadening of the spectra from 287-288.5 eV (Chen et al., 2014a; Solomon et al., 2012), which is representative of carboxylic OC. Both R2 and R3 had thinner carboxylic peaks at this region, suggesting that incorporated native OM is dominantly carboxylic OC, in addition to aromatic OC, whereas the exterior surface region is a combination of aliphatic groups associated with carboxylic

moieties. Polysaccharide-associated aliphatic moieties (289.9 eV) are also more concentrated in R1. The concentration of polysaccharides and carboxylic groups in BIOs has been found in previous STXM-NEXAFS investigations (Chan et al., 2009; Miot et al., 2009b), which was attributed to BIO native OM largely consisting of acidic polysaccharides (Chan et al., 2009). In conclusion, aliphatic moieties are likely surface complexed or occluded to the BIO sheath surface whereas carboxylic and aromatic moieties are expected to be incorporated into the BIO mineral structure, which may have impacts on reactivity for OM.

Native OM was found to be partially chemically stable when reacted with desorbing reagents (Table 3.6). Deionized (DI) water, 0.1 M NaCl, and 0.5 M NaCl all resulted in approximately  $19 \pm 2.0\%$  desorption of OC, signifying that increasing ionic strength had little effect on OC mobilization. However, the desorption of  $20.79\% \pm 0.4\%$  OC in DI suggests that a fraction of native OM was easily desorbed, likely explained by potential weak physical occlusion and/or aggregation of EPS during BIOs formation. 0.1 M and 1.0 M  $\text{Na}_2\text{H}_2\text{PO}_4$  resulted in significantly more desorption ( $35.7 \pm 0.25\%$  and  $55.7 \pm 0.63\%$  desorbed OC, respectively). We infer from these results that a large majority of the native OM associated with BIOs is stable at high ionic strength conditions, suggesting that BIOs actively stabilize OM upon formation. However, sequestration may greatly be affected by the presence of competitive oxyanions (i.e., phosphate) and is likely OC species dependent.<sup>8</sup> Also, native OM desorption extent is likely to be impacted by the age of the BIO mineral (i.e., length of time BIO is in solution after formation), which would likely affect native OM concentration and, potentially, observed percent release. Higher percentages of

desorbed native OM were likely observed because of low initial native OM concentration and the presence of loosely occluded, easily desorbed aliphatic moieties.

### 3.3.2 Sorption of Dissolved Organic Matter to BIOs

To understand the potential for natural BIOs to sequester allochthonous sources of DOM (Figure 3.1A), we conducted BIO sorption experiments using DI water-extractable leaf litter DOM (referred to as DOM throughout), SRFA, and SRHA, followed by desorption experiments to probe the chemical stability of associated OM. Sorption isotherm experiments revealed that BIOs sorbed up to  $103 \pm 4.17$  mg OC  $g^{-1}$  BIO (Figure 3.6A), approximately half of the OC sorption capacity per mass of 2-line ferrihydrite (Figure 3.7) (Chen et al., 2014b; Sowers et al., 2018), despite the Fe phase being 2-line ferrihydrite (Figure 3.4). This result suggests the quantity of OM sorbed by Fe phases formed at redox transitions may potentially be overestimated. The loading extent of SRFA ( $95 \pm 4.52$  mg OC  $g^{-1}$  BIO) was found to be similar to DOM, such that a single Langmuir fit (Table 3.7) was found to be an effective model (model efficiency (E) = 0.965; perfect fit = 1) of sorption behavior for both data sets. Sorption extent for SRHA sorption to BIOs was higher than both DOM and SRFA, with an observed sorption maxima of  $116 \pm 2.90$  mg OC  $g^{-1}$  BIO and a Langmuir fitted sorption maxima approximately 25.9 mg OC  $g^{-1}$  BIO more than DOM and SRFA (Table 3.7). The greater sorption of SRHA to BIOs is likely due to a higher concentration of aromatic moieties in SRHA compared to DOM (Lv et al., 2018; Lv et al., 2016), and suggests that our DOM source is likely best represented by SRFA.

Additionally, sorption data was normalized to surface area as previous research on BIO sorption to arsenate and chromate has shown surface area to significantly dictate BIO reactivity (Sowers et al., 2017; Whitaker et al., 2018), likely due to native OM aggregation on the BIO surface decreasing surface area (Duckworth et al., 2009; Emerson et al., 2010; Emerson and Moyer, 1997; Sowers et al., 2017). Normalization of the sorption data revealed that BIOs have high reactivity for DOM per surface area. Both BIOs and 2-line ferrihydrite (124.1 versus 288.7 m<sup>2</sup> g<sup>-1</sup>, respectively (Table 3.1)) were found to have sorption maxima at 0.88 ± 0.01 mg OC m<sup>-2</sup> sorbent (Figure 3.6B), and modeled well using a singular Langmuir fit (E = 0.931) (Table 3.8) (Bolster and Hornberger, 2007). Normalization of the sorption data to Fe content revealed similarities congruent to trends observed for surface area-normalized data, where sorbed OC concentration was similar for all equilibrium OC concentrations other than those greater than 1000 mg OC L<sup>-1</sup> (Figure 3.8) Therefore, we expect that Fe content is not a factor driving differences in total DOM sorption between BIOs and synthetic 2-line ferrihydrite. Although DOM reactivity of BIOs is similar to synthetic 2-line ferrihydrite per surface area and Fe content, OM sorption to BIOs per mass of sorbent is approximately half of what is observed for 2-line ferrihydrite (Figure 3.7). Therefore, BIOs and synthetic 2-line ferrihydrite may have similar sorption behavior per surface area and Fe content but expected sorption of DOM by BIOs in environmental systems is significantly lower than similar masses of abiogenic, short-range-ordered Fe phases. Observed aliphatic-associated carboxylic moieties from STXM-NEXAFS analysis are likely responsible for decreased OM reactivity per mass of sorbent. Native OM impurities present on the BIO sheath surface may physically

inhibit sorption via aggregation or be chemically resistant to exchange with allochthonous OM sources. Similarities in sorption behavior per surface area suggests that there are similar concentrations of OM reactive domains per surface, which may be explained by potential OC-OC interactions between aggregated native OM and DOM, in addition to Fe-OM interactions, but will require further investigation.

High OM chemical stability for DOM-reacted BIOs was also observed (Figure 3.6C). When exposed to a high ionic strength solution (0.1 M NaCl), a low fraction of desorption was observed, especially for BIOs reacted at 100 or 300 mg OC L<sup>-1</sup> ( $8.72 \pm 0.52\%$  and  $15.83 \pm 0.62\%$ , respectively). The high stability of DOM-reacted BIOs in the presence of 0.1 M NaCl suggests that sorption of OC is likely not significantly mediated by weak electrostatic complexes (Sparks, 2003; Sposito, 2008). Significantly increased desorption (approximately  $30 \pm 1.9\%$  increase over 0.1 M NaCl) was observed when samples with similar loading were reacted with 0.1 M NaH<sub>2</sub>PO<sub>4</sub>, a competitive ligand exchanger. At low equilibrium OC concentrations (5-20 mg OC L<sup>-1</sup>; Figure 3.9) the chemical stability of OC continues to increase, especially for the 0.1 M NaH<sub>2</sub>PO<sub>4</sub> treatment ( $16.20 \pm 2.65\%$ ). Pairing these results with the 0.1 M NaCl treatment, we infer that OM loaded to BIOs is likely dominantly sorbed through inner sphere complexation or hydrogen bonding mechanisms (Kleber et al., 2015; Sparks, 2003). At higher initial DOM concentrations, we suspect that variations in chemical stability are likely attributed to BIO surface saturation, resulting in more easily desorbed DOM that is present due to organic-organic interactions, physical occlusion/aggregation processes, and/or van der Waals forces. Similar desorption experiments conducted by Chen et al. (2014b) for DOM-reacted ferrihydrite at pH 7

found 29.3% of bound OC was desorbed using 0.1 M  $\text{NaH}_2\text{PO}_4$  compared to our results at a similar OC loading ( $48.7 \pm 1.29\%$  at an equilibrium OC concentration of  $300 \text{ mg OC L}^{-1}$ ), suggesting that DOM-loaded BIOs may not be as stable as DOM-loaded ferrihydrite in the presence of a strong ligand exchange reagent. Although synthetic 2-line ferrihydrite may have high chemical stability of bound OM, increased stability at elevated ionic strength and retention of more than 50% of sorbed OC at equilibrium OC concentrations less than  $300 \text{ mg OC L}^{-1}$  indicates that BIOs may act as a chemically resilient OM sink in aqueous systems. Additionally, desorption experiments performed for SRFA and SRHA complexed to BIOs revealed that both humic standards desorbed similar to DOM within approximately 5% (Figure 3.10). This suggests that the humic standards and DOM have similar chemical stability and may be bound via similar mechanisms. Speciation of desorbed DOM, as well the fraction remaining sorbed, will be analyzed in future research to further probe the impacts of DOM molecular composition on sequestration.

### **3.3.3 Solid Phase Organic Matter Speciation**

Preferentially sorbed OC species, binding mechanisms, and BIO native OM speciation were obtained using FTIR spectroscopy (Figure 3.11; Table 3.9) and compared to BIOs samples reacted with humic substances (SRFA and SRHA; Figure 3.12). Peak emergence at  $1620 \text{ cm}^{-1}$  for DOM-reacted BIO (BIO\_DOM) is shifted from the asymmetric carboxylic stretching feature present for DOM ( $1580 \text{ cm}^{-1}$ ) and is also associated with aromatic C=C stretching (Chen et al., 2014b; Eusterhues et al., 2010; Niemeyer et al., 1992; Sowers et al., 2018); therefore, the combination of

increased peak intensity and a shift relative to the initial DOM may be attributable to ligand exchange interactions with carboxylic moieties that are likely associated with aromatic groups (Eusterhues et al., 2010; Gu et al., 1995; Niemeyer et al., 1992). This peak was also heightened for SRFA-reacted BIO (BIO\_SRFA), which is enriched with carboxylic and aromatic moieties (Figure 3.12), and suggests that SRFA is interacting similarly to the leaf litter DOM source. We also observed a slight increase in absorbance at  $1525\text{ cm}^{-1}$ , indicative of aromatic C=C stretching (Baes and Bloom, 1989; Chen et al., 2014b; Gu et al., 1994; Niemeyer et al., 1992), for BIO\_DOM, which provides further evidence that aromatic moieties are likely playing a major role in sorption. This phenomenon was seen to a small extent for BIO\_SRFA, but as a broad peak for BIO\_SHRA that likely consists of peaks at 1620, 1580, and  $1525\text{ cm}^{-1}$ . This feature is different from the feature for BIO\_DOM and BIO\_SRFA (which had similar spectra across this range), suggesting that SRHA is potentially interacting differently with BIOs and may explain differences observed for sorption isotherm experiment. Due to similarities in sorption behavior observed in batch experiments and ATR-FTIR results, we concluded that the leaf litter DOM is comparable to SRFA in its sorption of BIOs.

In addition, shifting of the peak diagnostic of symmetric carboxylic stretching ( $1400\text{ cm}^{-1}$  shifted to  $1390\text{-}1384\text{ cm}^{-1}$ ) is widely linked to carboxylic moiety ligand exchange processes (Chen et al., 2014b; Heckman et al., 2011; Sowers et al., 2018); however, minor shifting or distortion was observed between BIO before and after reaction with DOM, SRFA, or SRHA, signifying that a component of BIO native OM was strongly sequestered via carboxylic moieties. Evidence for the sorption of

carbohydrate ( $1230\text{ cm}^{-1}$ ) moieties were also observed for BIO\_DOM. Lastly, we observe major distortion of the band from  $1030\text{ cm}^{-1}$  to  $1005\text{ cm}^{-1}$  between BIO and BIO\_DOM. This band range represents the deformation of C-O bonds in polysaccharides and the strengthening of signal at  $1030\text{ cm}^{-1}$  has been attributed to carboxylic or -OH enrichment (Fu and Quan, 2006; Gu et al., 1995; Stevenson, 1994), providing evidence that native OM carboxylic associated polysaccharides are critically involved in OC exchange. Native OM was found to be dominated by carboxylic and polysaccharide moieties, which is similar in composition to what was observed at the sheath exterior for the STXM-NEXAFS results (Figure 3.5). These native OM moieties may have competitive effects on DOM sorption, decreasing the potential of BIOs to sorb OM to an extent equivalent to synthetic 2-line ferrihydrite. ATR-FTIR results strongly support carboxyl- (either associated or unassociated with polysaccharides) and aromatic-mediated sorption of OM to BIOs, which was further probed using FT-ICR-MS analysis of DOM pre- and post-sorption.

#### **3.3.4 FT-ICR-MS Analysis of Pre- and Post-sorption DOM**

Using FT-ICR-MS, the molecular composition of  $200\text{ mg OC L}^{-1}$  DOM was characterized before and after exposure to BIOs (Figure 3.13; Figure 3.14) and assigned operationally defined OC compound classes. Pre-sorption DOM stock was found to be compositionally diverse through post-spectral processing (peaks present in at least two of the three analytical replicates), as we observed  $>2,500$  mass spectral peaks ranging from 300 to 900  $m/z$ . Initial DOM largely consisted of lignin-like compounds (64.16%) and aliphatic groups absent of N (Aliphatic\_No N) (24.27%),

with smaller contributions from polycyclic aromatic (PCA) (3.19%), aromatic (3.91%), carbohydrate-like (1.42%), and N-containing aliphatic (Aliphatic\_N) (3.06%) compounds (Figure 3.13; Table 3.2). This distribution correlates well to past FT-ICR-MS spectral analysis for DI-extractable DOM from a forest O horizon (Coward et al., 2018). FT-ICR-MS analysis of SRFA and SRHA before and after reaction with Fe(III) oxides have been previously reported and are similarly dominated by lignin-like compound classes, with SRFA having similar concentration of PCA compounds (Lv et al., 2018); therefore, we chose to focus FT-ICR-MS analyses on leaf litter DOM in following pre- and post-sorption analyses.

Comparing FT-ICR-MS spectral data for DOM with BIO-reacted DOM (BIO\_DOM), we formed a relative intensity index to describe the extent of relative sorption by BIOs (Figure 3.13). This index does not provide an exact degree of OM sorption (may be affected by low signal for a given compound class (Table 3.2, 3.3)) and should only be used to evaluate relative sorption between organic compound classes. We observed high sorption of compounds at low O/C values and across all observed values of H/C, especially at low H/C values, suggesting that PCA, aromatic, were preferentially sorbed. This is supported by SUVA measurements performed pre- and post-sorption. The significant sorption of PCA and aromatic compound classes observed for the DOM system pre- and post-sorption was similar to previous FT-ICR-MS observations for SRFA reacted with hematite (Lv et al., 2018). All compounds identified as carbohydrate-like were found to be completely sorbed; however, this compound class was also marked by low formulae abundances. Extensive partial sorption of lignin-like and Aliphatic\_N groups were observed with increasing O/C

values. This trend indicates that lignin-like and Aliphatic\_N groups may be bound via an O-containing moiety such as carboxylic groups, which suggests that sorbed OM may be strongly bound via exchange of BIOs surface hydroxyl moieties (Chen et al., 2014b; Lv et al., 2016). Aliphatic\_No N compounds increased, suggesting less affinity by BIOs, but may have still sorbed to BIO but to a lesser degree than the other components (aggregate change in pre- and post-sorption DOM composition = 12.65%). The sorptive preference of BIOs for hydrophilic moieties (i.e., aromatic and carboxylic moieties) over hydrophobic moieties (i.e., aliphatic groups) is congruent with the zonal model proposed for abiogenic clay and oxide minerals (Kleber et al., 2007), in which a contact zone of ligand exchange interactions (i.e., potential ligand exchange of BIO sheath surface hydroxyls with carboxylic moieties) and an adjacent zone of hydrophobic interactions is proposed. These results are also in alignment with abundant previous research indicating the preferential adsorption of high O/C, aromatic compounds to iron (oxyhydr)oxides and soils (Avneri-Katz et al., 2017; Lv et al., 2016; Riedel et al., 2012). The application of a strict signal to noise ratio may have affected the proportion of sorbed compound classes; however, compounds classes that were observed as sorbed are supported by FTIR analysis.

### **3.3.5 Effect of Oxygenation on Organic Matter Sorption**

Intensity-normalized relative abundances for each compound class were parsed by formulae oxygen (O)-number (Figure 3.15), which range from 1 to 25, indicating the degree of compound oxygenation. O-number has been used as a proxy for the presence of carboxylic moieties (Avneri-Katz et al., 2017; Coward et al., 2018; Lv et

al., 2016), widely thought to be a primary driver of inner sphere organo-mineral associations (Gu et al., 1995; Kleber et al., 2015; Lalonde et al., 2012). Preferential sorption (negative values) of specific OC compound classes was accompanied by systematic enrichment of contrasting classes, which may be derived from enrichment in the remaining distribution, or potential release and exchange of OM already bound to BIOs (Figure 3.1C, D). Aromatic and PCA compounds were also significantly sorbed at low O-number, suggesting that fractionation may not entirely involve carboxylic moieties or may favor small compound size (Coward et al., 2018). Carbohydrate-like OC formulae were sorbed almost completely at  $O_{\geq 15}$ . We conclude that this feature may signify the high affinity of BIOs for acidic polysaccharides, formed via carboxylic acid-bearing carbohydrates, which was also suggested from previous STXM-near edge X-ray absorption fine structure (NEXAFS) analysis of BIOs (Chan et al., 2009; Miot et al., 2009a; Miot et al., 2009b); however, reactions with DOM sources of higher carbohydrate-like compound concentration are needed to prove this conclusion. Lignin-like groups were found to primarily sorb to BIOs across all O-numbers, signifying the concentration of carboxylic moieties is not an important factor of lignin-like compound sorption.

Aliphatic\_N compounds were found to sorb only at high O-number ( $\geq 21$ ) and were either unaltered or potentially released to solution from BIO at lower O-numbers (Figure 3.15). The sorption of highly-oxygenated, N-containing aliphatic compounds suggests that N-containing organic compounds may strongly compete for BIO surface domains (Kleber et al., 2007; Rillig et al., 2007). Mineral-associated N has recently been proposed as a significant mediator of environmental N cycling (Jilling et al.,

2018); therefore, the affinity of BIOs for N-containing aliphatic groups may be due to high affinity for N. The preferential role of N in mediating adsorption is further evidenced by the observed enrichment of N-less aliphatic compounds, which indicates low sequestration by BIOs.

Further insight into OC speciation was gathered from the double bond equivalency of the formulae, representing the degree of saturation (Lv et al., 2016; Ohno et al., 2014), parsed by O-number (Figure 3.16). Significant sorption of high double bond equivalency (DBE) formulae at low ( $\leq 7$ ) O-number suggests that BIOs may be critical to the sequestration of unsaturated OC. Sorption at O-number  $\geq 15$  has previously been attributed to the interaction of Fe (oxyhydr)oxide with carboxylic acids (Coward et al., 2018; Lv et al., 2016), providing additional evidence that carboxylic moieties are critical to BIO mineral complexation of OC.

### **3.4 BIOs as an Emergent Sorbent of Dissolved Organic Matter**

This work demonstrates that naturally-forming bacteriogenic iron (oxyhydr)oxides are highly reactive sorbents of OM in circumneutral environments that may be largely unaccounted for in organo-mineral investigations. BIOs were found to effectively sorb OM from leaf litter DOM, SRFA, and SRHA. However, this extent is lower than the observed Fe(III) mineral phase (2-line ferrihydrite) would suggest, indicating that expected sorption of OM to naturally-occurring Fe oxides in aqueous environments may be overestimated. Native OM impurities in and occluded to BIO sheaths are likely responsible for observed decreased allochthonous OM reactivity compared to synthetic 2-line ferrihydrite. Surface area and Fe normalization

of the sorption data resulted in similar sorption trends, suggesting that native OM interactions are likely why less OM was sorbed by BIO per sorbent mass compared to synthetic 2-line ferrihydrite. We also provide a direct analytic linkage of FT-ICR-MS and FTIR spectroscopies to illustrate the preferential sorption of OC compounds between BIOs and surrounding DOM (Figure 3.1). Using both techniques, we provide compelling evidence that carboxylic, either associated or unassociated with polysaccharides, and aromatic moieties play a critical role in the sorption of OM. This conclusion supports previous research suggesting that organo-mineral associations are largely dictated by reactive carboxylic moieties (Chen et al., 2014b; Kleber et al., 2015; Sowers et al., 2018). Aliphatic groups unassociated with N increased in solution post-sorption, likely due to a combination of enrichment, selective sorption, and/or release of native OM from BIO. These results have applications to understanding OC cycling at redox interfaces, which applies to previous research attributing “iron traps”, likely containing BIOs, to acting as a barrier that limits transport of terrestrial DOM to the ocean (Riedel et al., 2013). These findings contribute to understanding the impact of BIOs on nutrient cycling in inundated rhizosphere and stream water systems and may also have impacts on the potential for BIOs to sorb metal(loid) contaminants through the possible creation of additional domains with high affinity for polyvalent metals or through competitive interference. (Bolan et al., 2011; Chakraborty et al., 2014) Also, understanding the molecular fractionation of OM on BIOs may provide better prediction of the transport of organic contaminants (i.e., pesticides) consisting of moieties that are preferentially sequestered by BIOs, which may inform future contaminant management strategies in terrestrial and aquatic systems. (Bolan et al.,

2011; Chakraborty et al., 2014; McKnight et al., 1992) Further support in the form of continued exploration of BIO heterogeneity, reactivity for DOM sources, and BIO mass assessment on larger scales is needed to make definitive conclusions on the biogeochemical impacts of BIO on OM cycling.

Table 3.1: DOM and BIO chemical composition and zeta potential at pH 6.5, with BET surface area for BIO. All values are reported within 10% error.

Sample	Fe	C	Al	Si	Ca	B	Cu	K	Mg	Mn	Na	P	S	Zn	SSA (m <sup>2</sup> g <sup>-1</sup> )	ζ-potential (mV)
BIO*	162.7	28.0	2.2	4.8	3.6	<0.1	<0.1	1.4	0.8	0.7	0.5	4.5	0.8	<0.1	124.1	-5.2
DOM**	2.2	1883.1	3.5	1.6	131.0	0.2	0.4	62.5	59.2	63.7	2.6	37.5	16.0	0.8	NA	-13.7

Table 3.2: Molecular composition of DOM stock and DOM-reacted BIO (BIO<sub>200</sub>). Relative abundancy is reported normalized to total spectral intensity.

	Intensity-Normalized Relative Abundancy (%)					
	Polycyclic Aromatic	Aromatic	Lignin-like	Carbohydrate-like	Aliphatic_No N	Aliphatic_N
DOM Stock	3.19%	3.91%	64.16%	1.42%	24.27%	3.06%
BIO-Reacted DOM	0.02%	0.35%	61.57%	0.00%	36.92%	1.15%

Table 3.3: FT-ICR-MS abundancy in DOM versus BIO<sub>200</sub> by peak count and total peak intensity of specific organic compound classes.

	DOM Stock					
	Polycyclic Aromatic	Aromatic	Lignin-like	Carbohydrate-like	Aliphatic_No N	Aliphatic_N
Peak Counts	186	182	1330	75	646	117
Peak Intensity	6.80E+08	8.32E+08	1.37E+10	3.03E+08	5.17E+09	6.51E+08

	BIO <sub>200</sub>					
	Polycyclic Aromatic	Aromatic	Lignin-like	Carbohydrate-like	Aliphatic_No N	Aliphatic_N
Peak Counts	1	23	832	0	433	41
Peak Intensity	9.84E+05	3.63E+07	7.87E+09	0.00E+00	4.71E+09	1.42E+08

Table 3.4: FT-ICR-MS abundancy in DOM extracted from leaf litter for 24 hrs by peak count and total peak intensity of specific organic compound classes. This DOM was not used in sorption experiments.

DOM Stock-24 hr extraction (For Comparison Only)						
	Polycyclic Aromatic	Aromatic	Lignin-like	Carbohydrate-like	Aliphatic_No N	Aliphatic_N
Peak Totals	71	126	1816	30	680	76
Peak Intensity	1.07E+08	2.73E+08	8.50E+09	7.55E+07	3.01E+09	1.98E+08
Rel. Abundancy - Intensity Normalized	0.88%	2.24%	69.85%	0.62%	24.78%	1.63%

Table 3.5: Pre-edge energy and edge-energy ranges used for average stack maps for C and Fe. Values were chosen according to the authors' previous research (Chen et al., 2014a; Sowers et al., 2018).

Element	Absorption Edge	Pre-edge Energy Stack Range (eV)	Edge Energy Stack Range (ev)
C	K	280-282	287.7-288.8
Fe	L <sub>3</sub>	700-703	709.5-710.5

Table 3.6: Desorption of BIO native OC using four different desorbing reagents.

	<b>Initial [C]</b>	<b>Desorbed</b>	<b>Error</b>	<b>Desorbed</b>	<b>Error</b>
<b>Desorbent</b>	mg kg <sup>-1</sup>	mg L <sup>-1</sup>	mg L <sup>-1</sup>	%	%
DI	24	4.99	0.09	20.79%	0.38%
0.1 M NaCl	24	4.23	0.10	17.62%	0.42%
0.5 M NaCl	24	4.52	0.02	18.85%	0.08%
0.1 M H <sub>2</sub> PO <sub>4</sub>	24	8.57	0.06	35.71%	0.25%
1.0 M H <sub>2</sub> PO <sub>4</sub>	24	13.37	0.15	55.71%	0.63%

Table 3.7: Langmuir model fitting parameters used to fit sorption isotherm data presented in Fig. 2a, where S is sorbed concentration, S<sub>max</sub> is the calculated maximum sorption, K is a sorption constant, C is dissolved sorbate concentration, and E is model efficiency.

$S = \frac{S_{\max} KC}{1 + KC}$		<i>95% Confidence Limits</i>				
		<b>Fitted Values</b>	<b>Standard Error</b>	<b>Lower Bound</b>	<b>Upper Bound</b>	<b>E</b>
<b>OM Source</b>	<b>Parameters</b>	mg OC g <sup>-1</sup> BIOs				
SRHA	K	0.004	0.001	0.002	0.005	0.98
	S <sub>max</sub>	151.1	10.4	137.6	165.6	1
SRFA & DOM	K	0.005	0.001	0.003	0.004	0.96
	S <sub>max</sub>	125.2	6.62	111.3	138.2	5

Table 3.8: Langmuir model fitting parameters used to fit sorption isotherm data presented in Fig. 2b, where S is sorbed concentration,  $S_{\max}$  is the calculated maximum sorption, K is a sorption constant, C is dissolved sorbate concentration and E is model efficiency.

<b>Parameters</b>	<i>95% Confidence Limits</i>				<b>E</b>
	<b>Fitted Values</b>	<b>Standard Error</b>	<b>Lower Bound</b>	<b>Upper Bound</b>	
	mg OC m <sup>-2</sup> BIOs				
K	0.004	0.001	0.003	0.005	0.93
Smax	0.996	0.044	0.904	1.088	

Table 3.9: ATR-FTIR peak positions shown in Figure 3.11, with interpreted assignments and corresponding references.

Peak Position (cm <sup>-1</sup> )	Assignment	References
1720	-C=O stretch of -COOH Symmetric C=O stretch of esters	Baes and Bloom, 1989; Niemeyer et al., 1992; Heckman et al., 2011
(i) 1620	Aromatic C=C stretch and/or shifted assymmetric COO- stretch	Niemeyer et al., 1992; Gu et al., 1994; Eusterhues et al., 2011
(ii) 1580	Assymmetric COO- stretch	Heckman et al., 2011
(iii) 1525	Aromatic C=C stretching	Niemeyer et al., 1992; Gu et al., 1994; Chen et al., 2014
1460	CH <sub>2</sub> scissoring	Heckman et al., 2011
1400	Symmetric COO- stretch	Chen et al., 2014
(iv) 1390-1378	Fe-COO stretch	Gu et al., 1994; Fu and Quan, 2006; Chen et al., 2014; Sowers et al., 2018
(v) 1270-1250	Phenolic O-H stretch	Niemeyer et al., 1992; Artz et al., 2008
(vi) 1225	C-O stretching of carbohydrates and OH deformation of COOH	Stevenson et al., 1994; Heckman et al., 2011
1080-1170	C-O stretch of aliphatic OH C-O stretch of polysaccharide	Baes and Bloom, 1989; Heckman et al., 2011
1040-1005	Acidic polysaccharides C-O stretching. Enrichment of carboxylic and OH groups	Gu et al., 1994; Fu and Quan, 2006; Heckman et al., 2011
910-908	Alkene =C-H bending	Stevenson et al., 1994

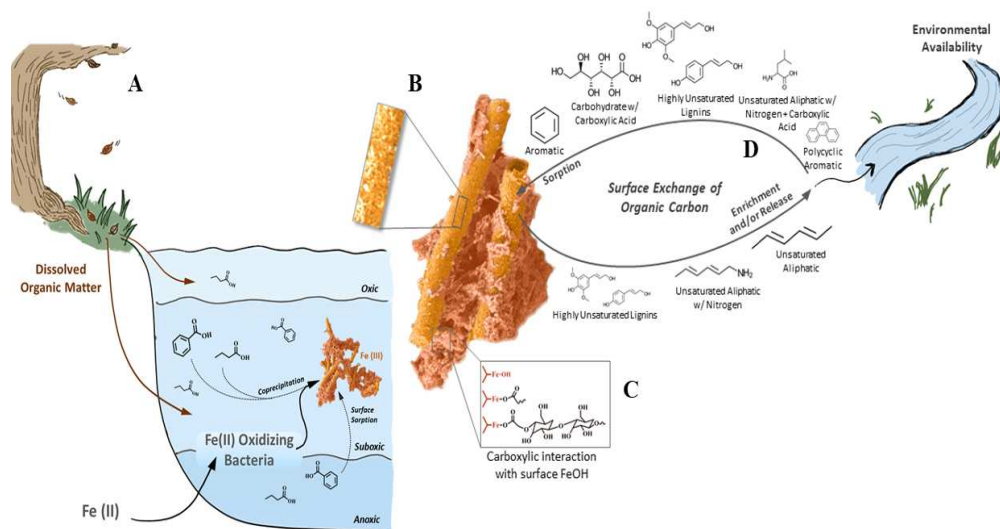


Figure 3.1: Conceptual model of the natural formation of bacteriogenic iron (oxyhydr)oxides (BIOs) in an aqueous system and the interactions hypothesized with organic carbon both during and after formation. Formation of BIOs via oxidation of Fe(II) by iron oxidizing bacteria (A). Organic carbon is incorporated into the mineral during BIOs formation via coprecipitation and sorbed to the surface after formation. The surface texture of these poorly crystalline structures is a fibrous network of highly associated Fe and C (B). Surficial hydroxyl groups on BIO sheaths are expected to exchange predominately with carboxylic moieties (C). Specific OC functional moieties are preferentially exchanged with the surface of BIOs, resulting in moiety-dependent OC sequestration and mobilization (D).

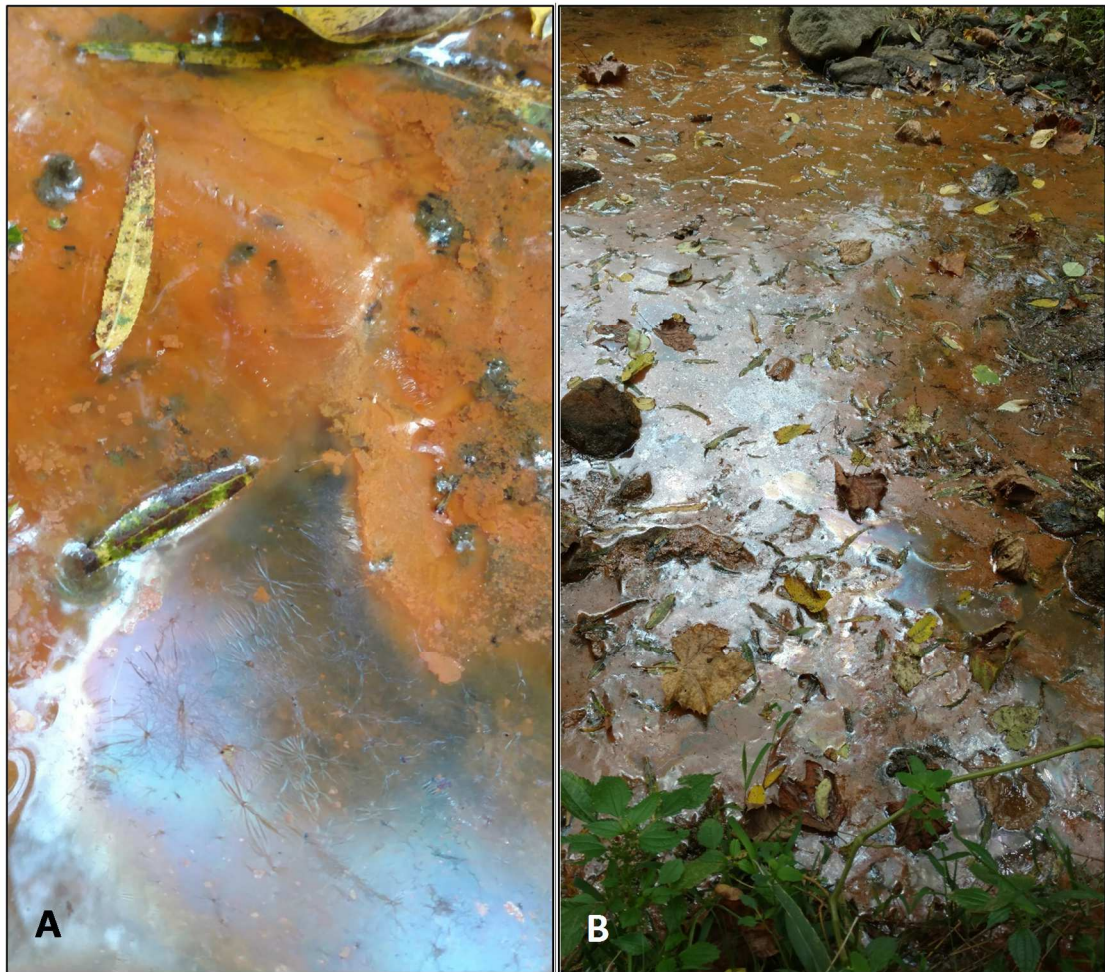


Figure 3.2: Naturally-occurring bacteriogenic iron oxides (BIOs) with visible sheens and corresponding biomass observed at the macroscale (A) and field scale (B). Images were taken at White Clay Creek, Newark, Delaware.

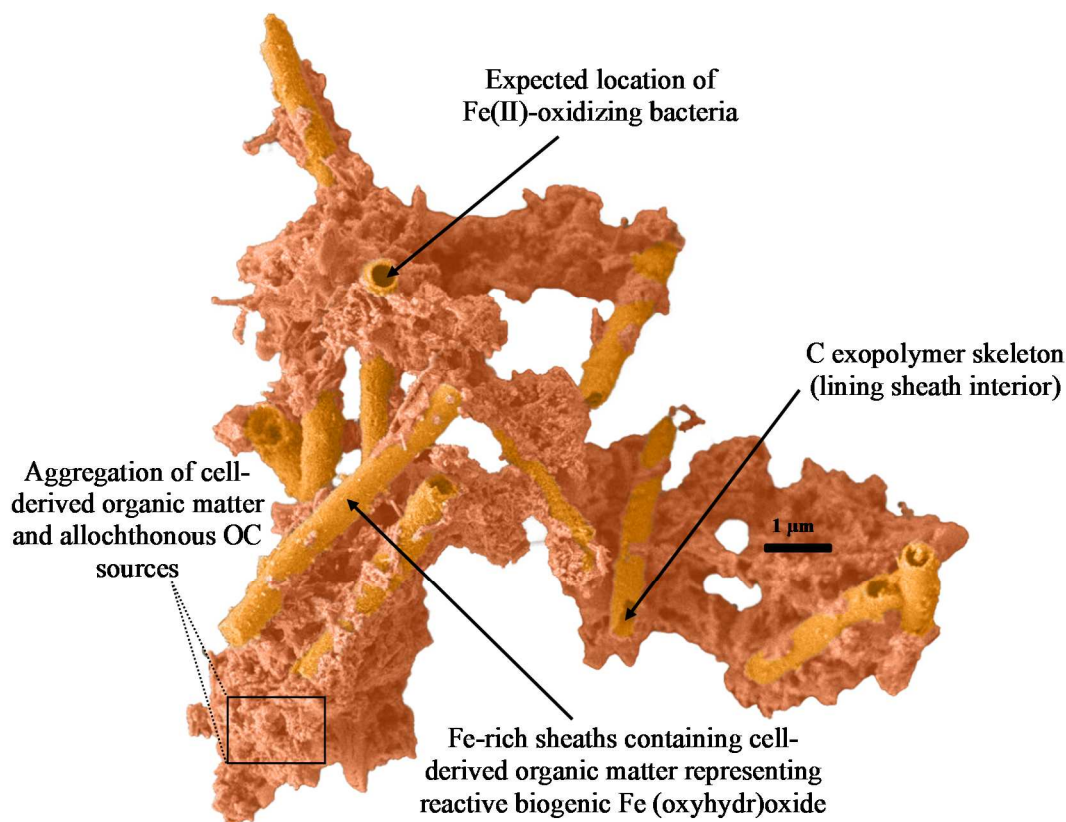


Figure 3.3: Generalized schematic of biogenic iron (oxyhydr)oxides collected from White Clay Creek, DE. Observed sheath/rod-like morphology is characteristic of Fe(II)-oxidizing bacteria *Leptothrix* and is expected to be responsible for surface interactions with potential sorptives. Incorporated cell-derived organic matter and surrounding EPS biomass is expected to affect reactivity. Native OC is used in the manuscript to refer to OC already present upon BIOs collection, which includes cell-derived OM and previously sorbed/coprecipitated OC.

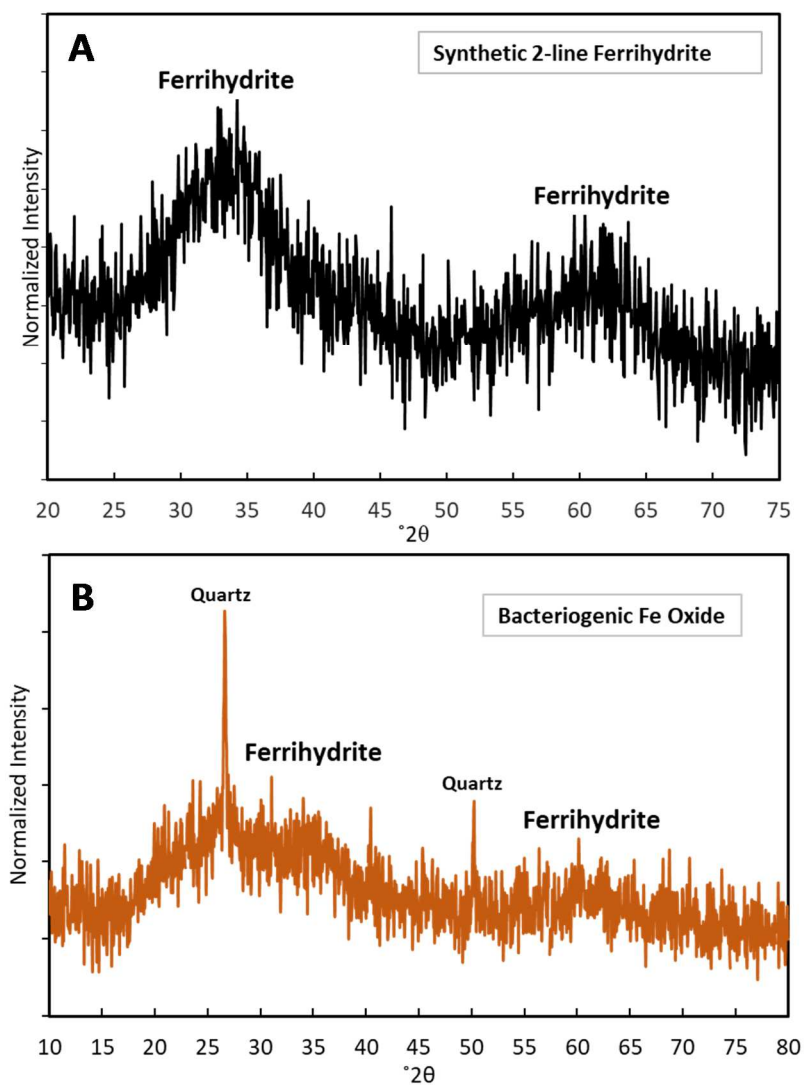


Figure 3.4: X-ray diffractograms for synthetic 2-line ferrihydrite (A) and BIO (B). BIOs was found to correspond well to the beat pattern of 2-line ferrihydrite, along with the inclusion of quartz grains.

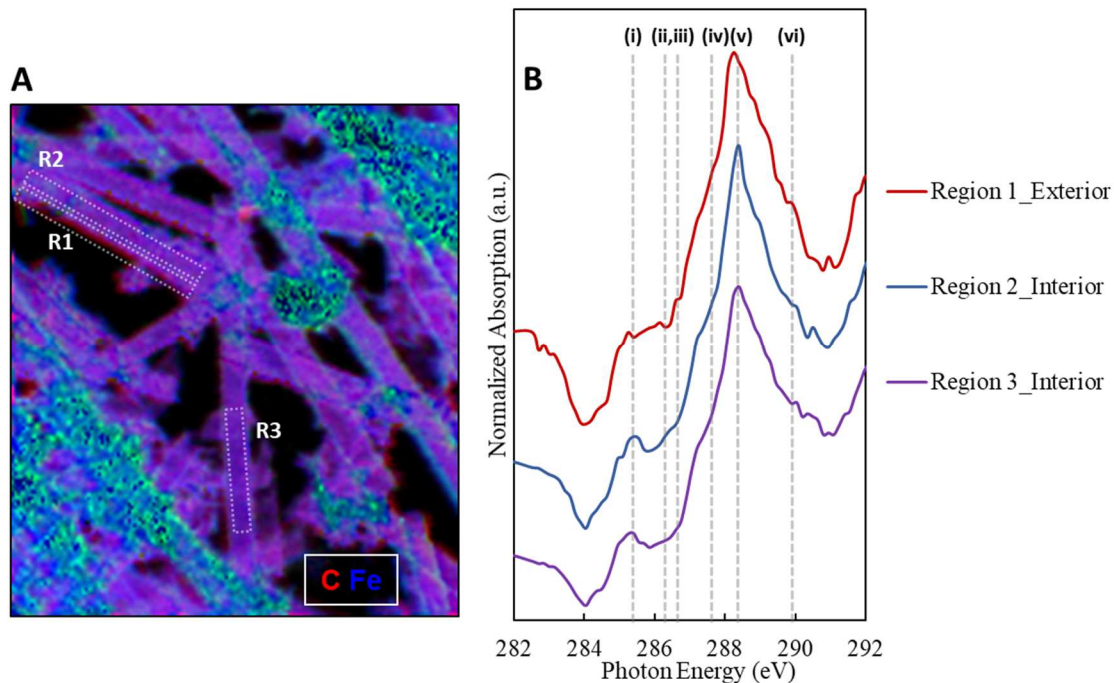


Figure 3.5: STXM optical density RGB image for BIO (A) paired with NEXAFS spectra at specific regions of interest at the interior or exterior of a BIO sheath (B). Red, green, and blue represent carbon, calcium, and iron, respectively. Purple regions represent areas of high C and Fe correlation whereas cyan regions were identified as areas too thick for transmission (optical density  $\geq 2.5$ ). Red coating present at the edges of the sheaths resemble potential C accumulations. NEXAFS spectra show unique OC speciation consisting of (i) aromatic (285.4-285.6 eV), (ii, iii) ketone carbonylic (286.5 eV), (iv) aliphatic (287.4 eV), (v) carboxylic (288.5 eV), and (vi) polysaccharide-associated aliphatic (289.8 eV) function moities.

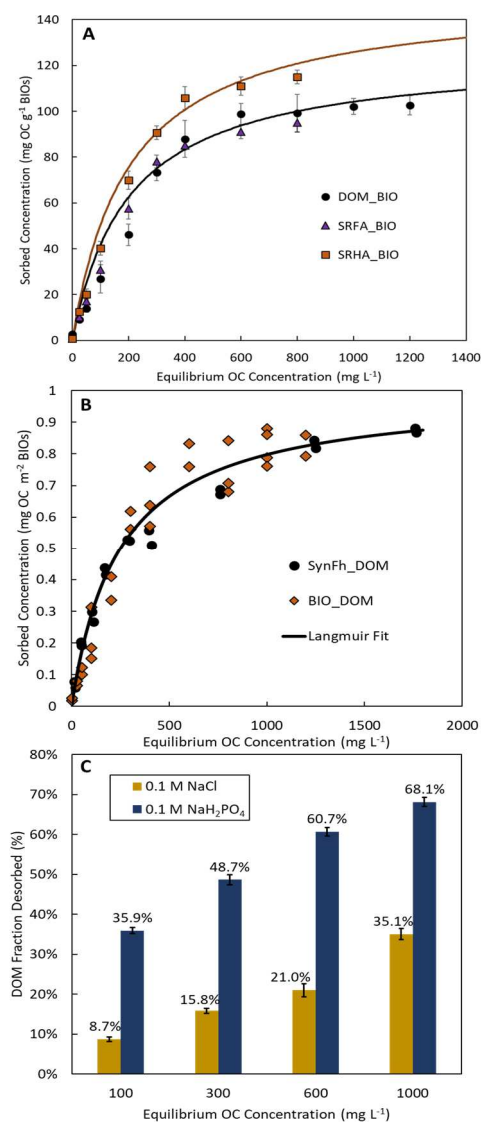


Figure 3.6: Sorption isotherm plot of DOM, Suwannee River Fulvic Acid (SRFA), or Suwannee River Humic Acid (SRHA) sorption to BIOs (A) compared to surface area-normalized sorption data for DOM sorption to BIOs or synthetic 2-line ferrihydrite (B), followed by desorption of OC from DOM-reacted BIO samples (C). A single Langmuir fit was found to fit both the DOM and SRFA data sets (model efficiency = 0.965) and surface area normalization resulted in a strong Langmuir fit (0.931) for both 2-line ferrihydrite and BIO reacted with DOM.

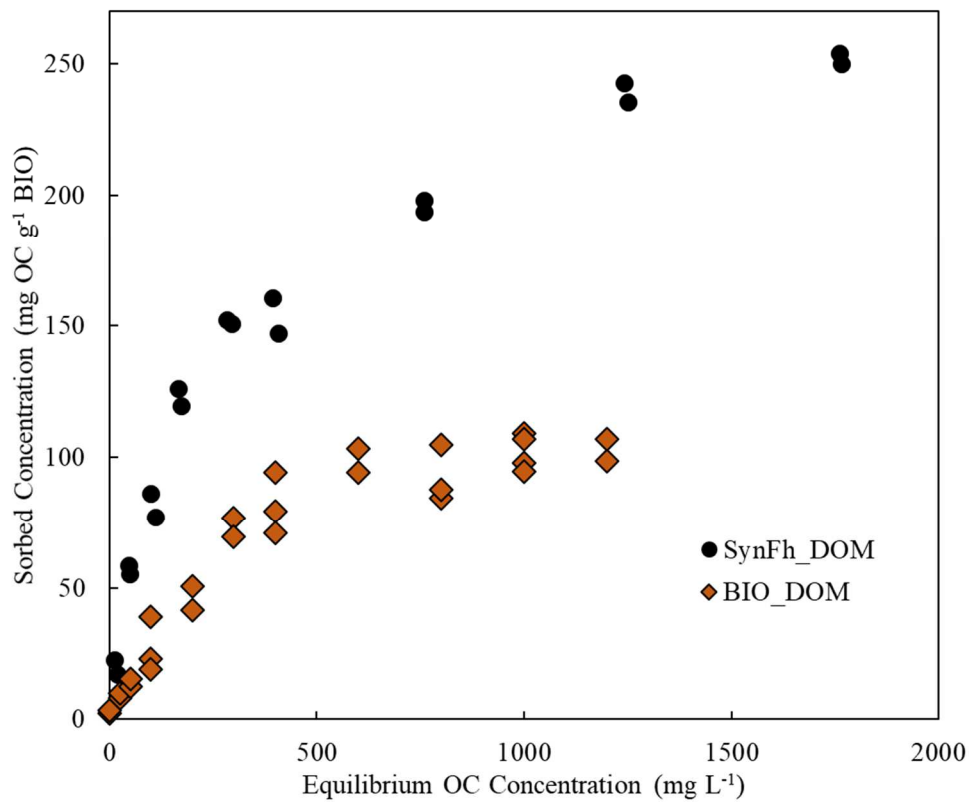


Figure 3.7: Sorption isotherm for DOM sorption to BIO or synthetic 2-line ferrihydrite. Sorption data is normalized to mass of sorbent.

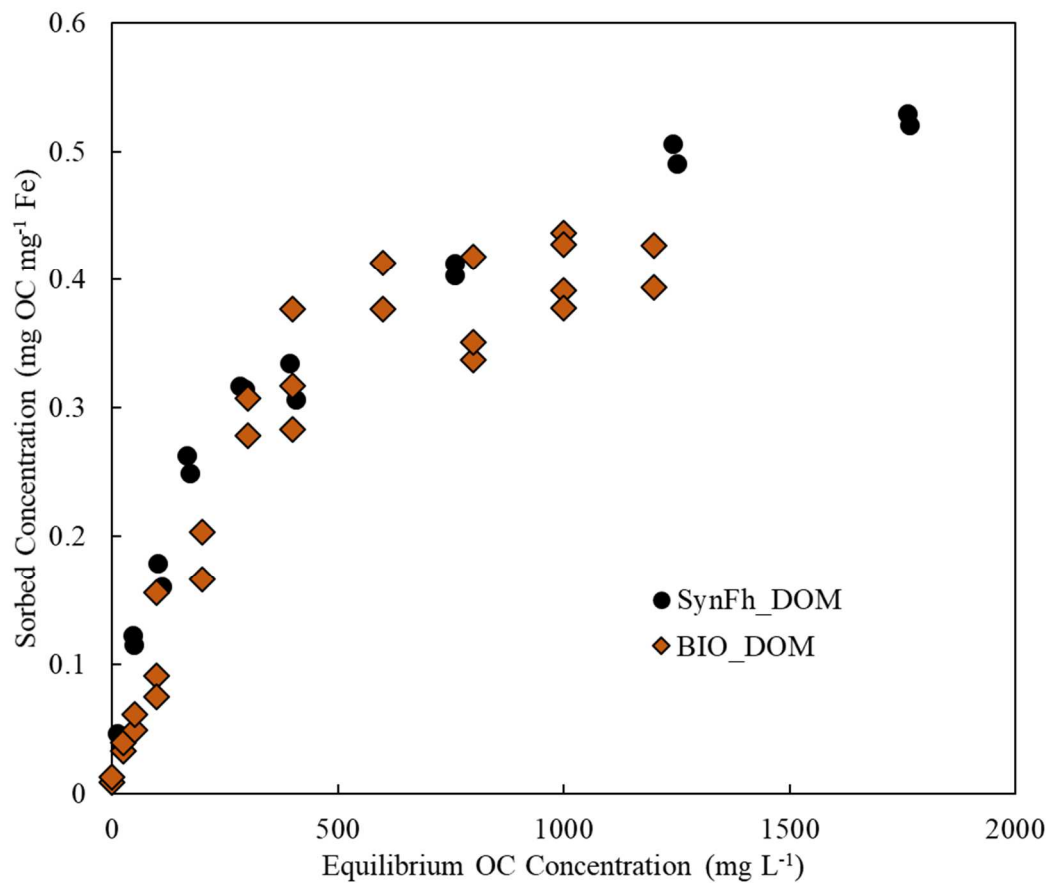


Figure 3.8: Sorption isotherm for DOM sorption to BIO or synthetic 2-line ferrihydrite. Sorption data is normalized to the Fe content of the sorbent.

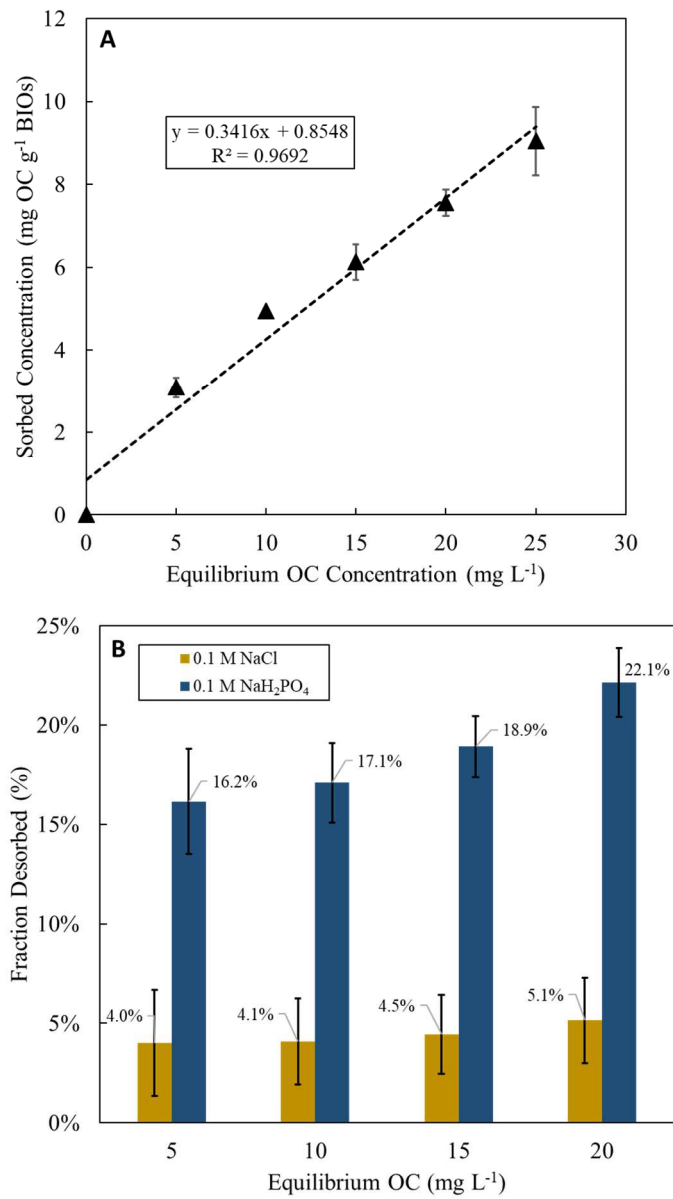


Figure 3.9: OC sorption to BIO isotherm (A) with corresponding desorption results (B) for samples reacted at low initial OC concentrations.

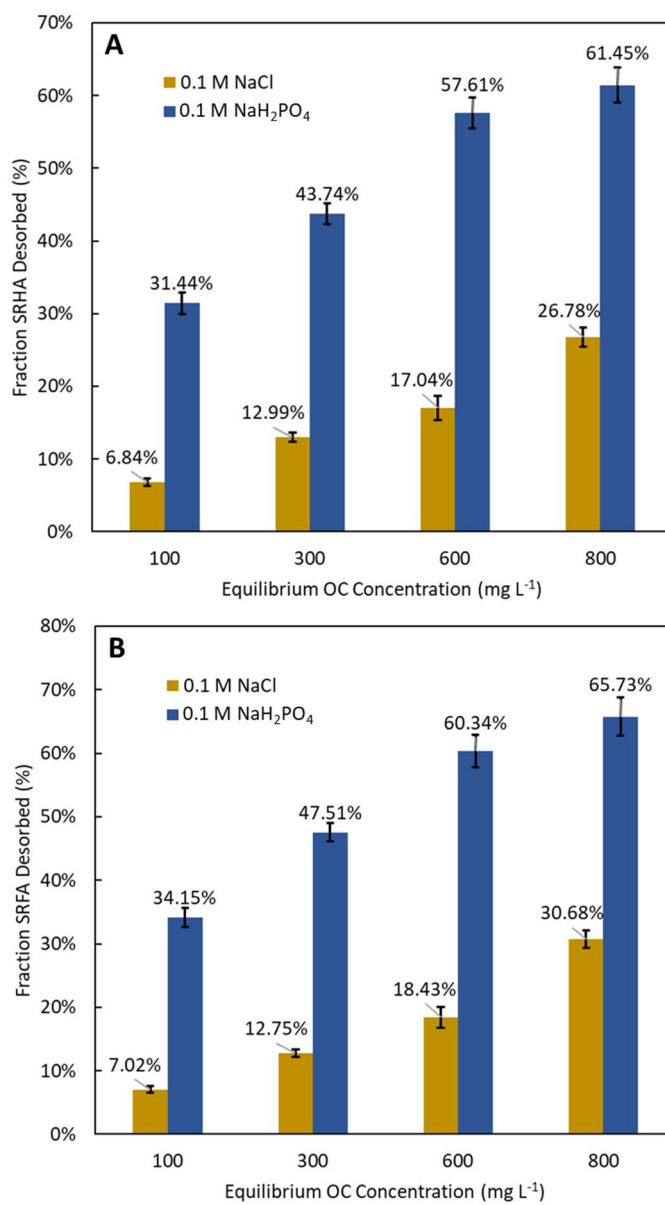


Figure 3.10: Desorption of SRHA (a) and SRFA (b) from BIOs that were reacted with SRHA or SRFA at OC concentrations ranging from 100 to 800 mg L<sup>-1</sup>.

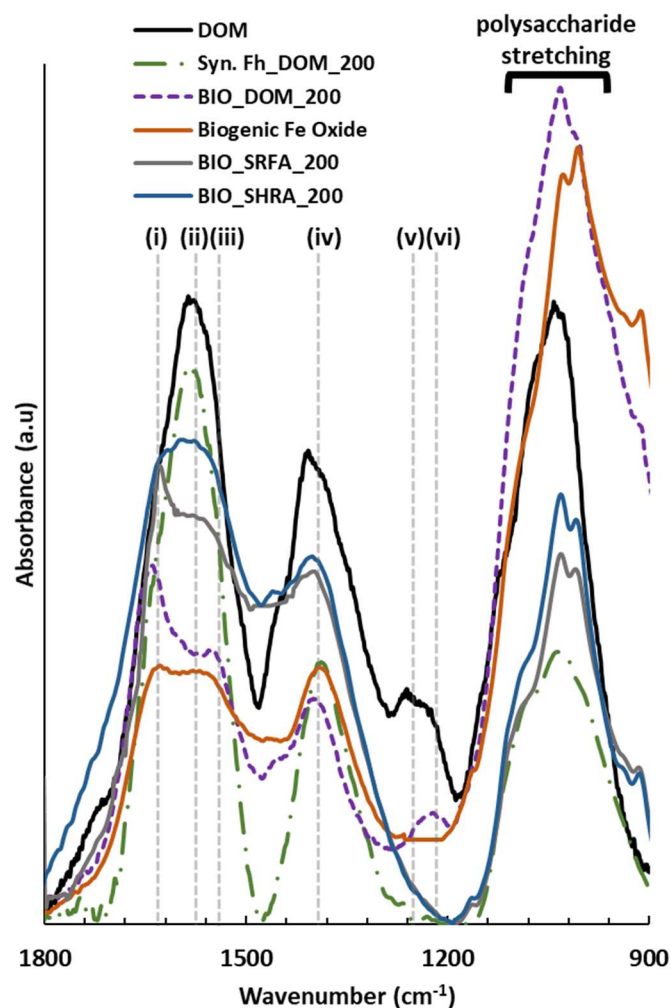


Figure 3.11: ATR-FTIR spectra showcasing potential mechanisms of OM sorption to BIOs and OC species preferentially sequestered. Primary features of interest (Table 3.9) include a shifted asymmetric carboxylic stretch for DOM-reacted BIO (i), asymmetric carboxylic stretch of DOM (ii), aromatic C=C stretching for all spectra (iii), ligand exchanged Fe-COO stretch for all Fe oxide samples (iv), phenolic stretching found only for DOM (v), carboxylic associated-carbohydrate stretching for DOM-reacted BIOs (vi). 1040 to 1005  $\text{cm}^{-1}$  represents the major involvement of BIOs with polysaccharides, with distortions of DOM-reacted BIOs attributable to enrichment by carboxylic moieties.

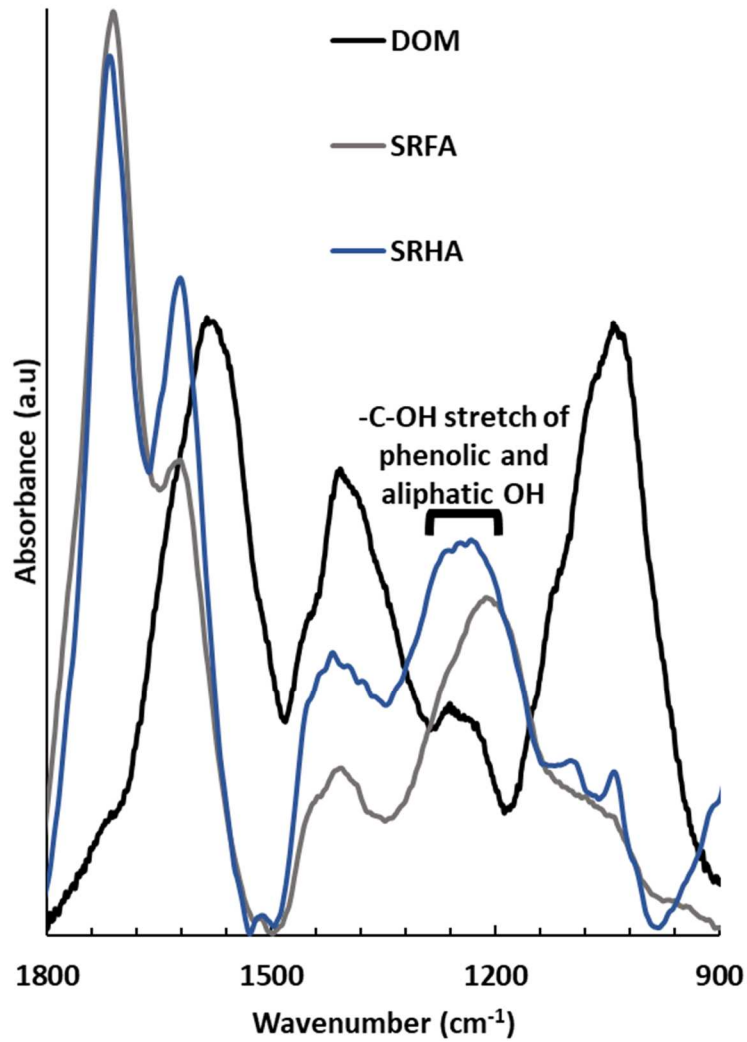


Figure 3.12: ATR-FTIR results for SRHA and SRFA standards. Dominant peaks are found at 1720, 1620, 1400, 1270-1250, and 1225-1200  $\text{cm}^{-1}$ , with corresponding assignments found in Table 3.9.

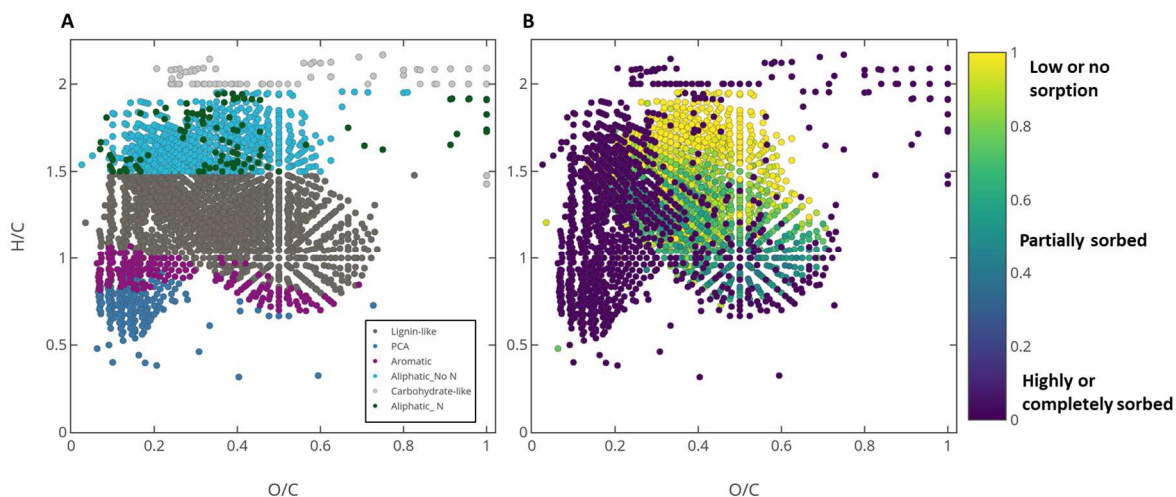


Figure 3.13: van Krevelen diagrams of unreacted DOM (A) compared to BIOs-reacted DOM (BIO<sub>200</sub>) (B). For A, assigned OC compound classification is shown. For B, the degree of sorption is displayed as highly or completely sorbed (dark purple), partially sorbed (color index), or low/no sorption (yellow), derived from spectral intensity pre- and post-sorption (see SI). The relative intensity index modeling sorption of DOM to BIOs was calculated by dividing BIO<sub>200</sub> by the peak intensity of the DOM before sorption. Color-scale indicates this index value, with lower index values signifying high extent of adsorption, while greater values indicate low extent of adsorption. Samples that are at a value of zero may be affected by low initial signal intensity; however, all sorption trends are supported by FTIR analysis of the BIO solid phase.

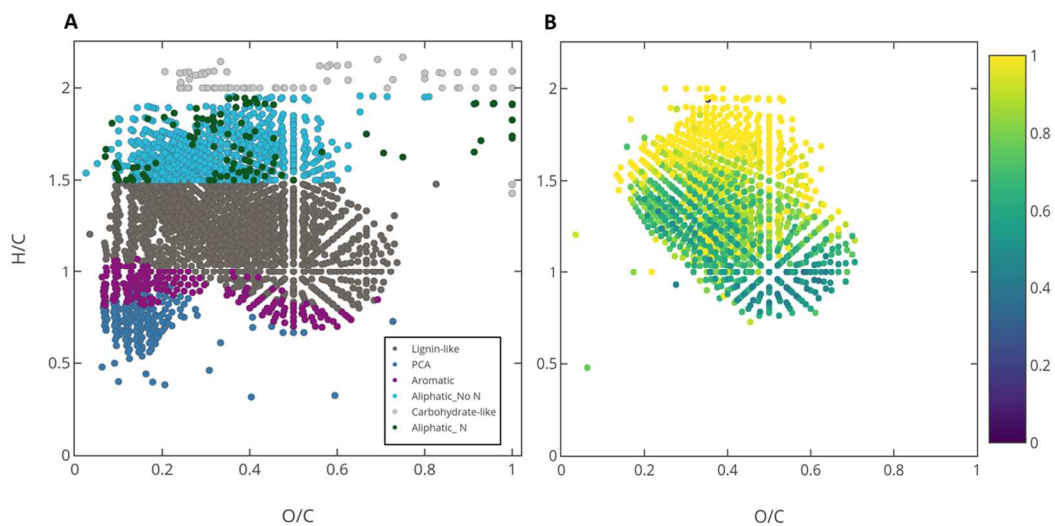


Figure 3.14: van Krevelen diagrams of pre-sorption initial DOM (A) and post-sorption formulae, as categorized by a relative intensity index (see SI for calculation), deemed partially adsorbed to BIOs (B). Colorscale for B indicates this index value, with lower index values indicating high extent of adsorption, while greater values are of indicative of low extent of adsorption.

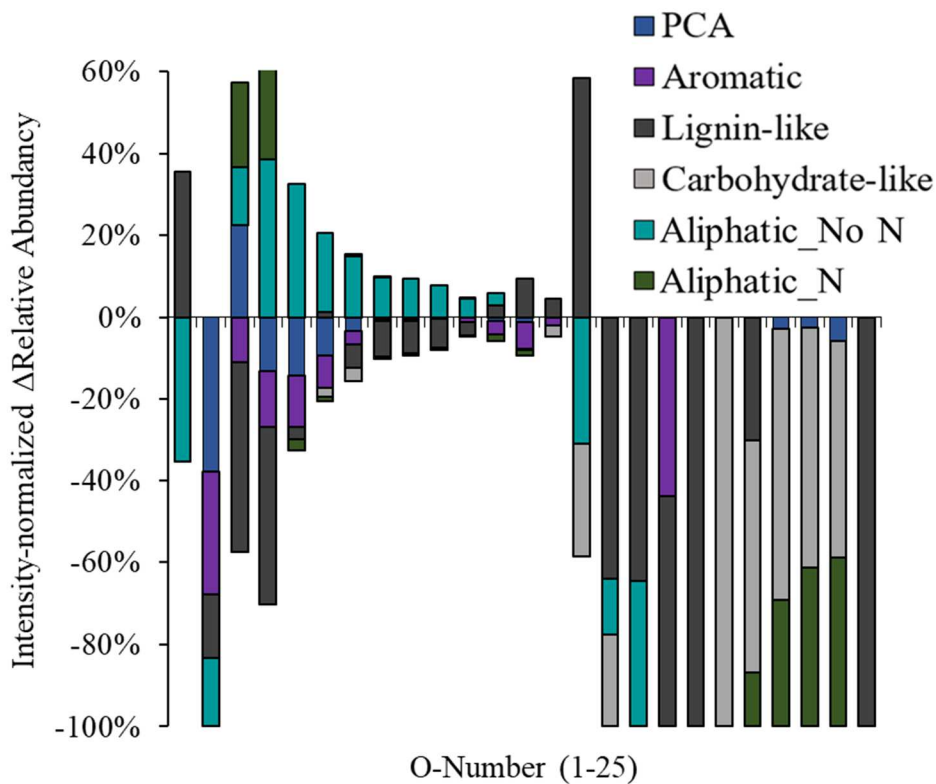


Figure 3.15: Molecular fractionation of sorbed OC parsed by formulae O content (O-number). Changes in relative abundance ( $\Delta$  %) of compound classes were parsed by formulae O-number, in which the abundance of post-sorption formulae in each compound class and O-number were compared to that observed in initial, unexposed DOM. The relative abundances of formulae within each O-number and compound class found for the initial DOM was then subtracted from the  $BIO_{200}$  normalized relative abundances, resulting in a  $\Delta$  % value. Positive percentages correspond to enrichment as a result of high sorption of other compounds or as release of native OC from BIO. Negative percentages indicate preferential sorption to BIOs.

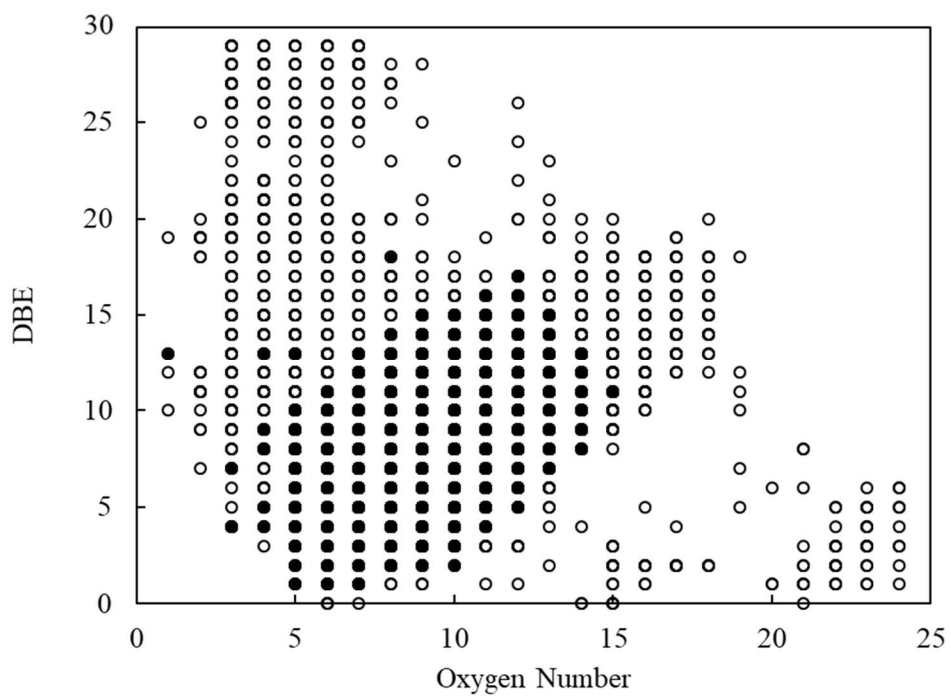


Figure 3.16: The double bond equivalence (DBE) and formulae oxygen number (0 - 25) of compounds in initial DOM (open circles) overlaid by those detected post-sorption to BIOs (closed circles).

## REFERENCES

- Amundson, R. (2001). The carbon budget in soils. *Annual Review of Earth and Planetary Sciences* 29, 535-562.
- Avneri-Katz, S., Young, R. B., McKenna, A. M., Chen, H., Corilo, Y. E., Polubesova, T., Borch, T., and Chefetz, B. (2017). Adsorptive fractionation of dissolved organic matter (DOM) by mineral soil: Macroscale approach and molecular insight. *Organic Geochemistry* 103, 113-124.
- Baes, A., and Bloom, P. (1989). Diffuse reflectance and transmission Fourier transform infrared (DRIFT) spectroscopy of humic and fulvic acids. *Soil Science Society of America Journal* 53, 695-700.
- Bauer, J., and Bianchi, T. (2011). 5.02—dissolved organic carbon cycling and transformation. *Treatise on estuarine and coastal science. Academic Press, Waltham*, 7-67.
- Bolan, N. S., Adriano, D. C., Kunhikrishnan, A., James, T., McDowell, R., and Senesi, N. (2011). Dissolved organic matter: biogeochemistry, dynamics, and environmental significance in soils. In "Advances in agronomy", Vol. 110, pp. 1-75. Elsevier.
- Bolster, C. H., and Hornberger, G. M. (2007). On the Use of Linearized Langmuir Equations All rights reserved. No part of this periodical may be reproduced or transmitted in any form or by any means, electronic or mechanical, including photocopying, recording, or any information storage and retrieval system, without permission in writing from the publisher. Permission for printing and for reprinting the material contained herein has been obtained by the publisher. *Soil Science Society of America Journal* 71.
- Chakraborty, P., Sharma, B., Babu, P. R., Yao, K. M., and Jaychandran, S. (2014). Impact of total organic carbon (in sediments) and dissolved organic carbon (in overlying water column) on Hg sequestration by coastal sediments from the central east coast of India. *Marine pollution bulletin* 79, 342-347.

- Chan, C. S., Fakra, S. C., Edwards, D. C., Emerson, D., and Banfield, J. F. (2009). Iron oxyhydroxide mineralization on microbial extracellular polysaccharides. *Geochimica et Cosmochimica Acta* 73, 3807-3818.
- Chen, C., Dynes, J. J., Wang, J., Karunakaran, C., and Sparks, D. L. (2014a). Soft X-ray spectromicroscopy study of mineral-organic matter associations in pasture soil clay fractions. *Environmental science & technology* 48, 6678-6686.
- Chen, C., Dynes, J. J., Wang, J., and Sparks, D. L. (2014b). Properties of Fe-organic matter associations via coprecipitation versus adsorption. *Environmental science & technology* 48, 13751-13759.
- Chen, C., Kukkadapu, R., and Sparks, D. L. (2015). Influence of Coprecipitated Organic Matter on Fe<sup>2+</sup> (aq)-Catalyzed Transformation of Ferrihydrite: Implications for Carbon Dynamics. *Environmental science & technology* 49, 10927-10936.
- Chorover, J., and Amistadi, M. K. (2001). Reaction of forest floor organic matter at goethite, birnessite and smectite surfaces. *Geochimica et Cosmochimica Acta* 65, 95-109.
- Cismasu, A. C., Michel, F. M., Tcaciuc, A. P., Tyliczszak, T., and Brown Jr, G. E. (2011). Composition and structural aspects of naturally occurring ferrihydrite. *Comptes Rendus Geoscience* 343, 210-218.
- Coward, E. K., Ohno, T., and Plante, A. F. (2018). Adsorption and Molecular Fractionation of Dissolved Organic Matter on Iron-Bearing Mineral Matrices of Varying Crystallinity. *Environmental science & technology* 52, 1036-1044.
- Davis, J. A. (1982). Adsorption of natural dissolved organic matter at the oxide/water interface. *Geochimica et Cosmochimica Acta* 46, 2381-2393.
- Dittmar, T., Koch, B., Hertkorn, N., and Kattner, G. (2008). A simple and efficient method for the solid-phase extraction of dissolved organic matter (SPE-DOM) from seawater. *Limnology and Oceanography: Methods* 6, 230-235.
- Duckworth, O. W., Holmström, S. J., Peña, J., and Sposito, G. (2009). Biogeochemistry of iron oxidation in a circumneutral freshwater habitat. *Chemical Geology* 260, 149-158.

- Emerson, D., Fleming, E. J., and McBeth, J. M. (2010). Iron-oxidizing bacteria: an environmental and genomic perspective. *Annual review of microbiology* 64, 561-583.
- Emerson, D., and Moyer, C. (1997). Isolation and characterization of novel iron-oxidizing bacteria that grow at circumneutral pH. *Applied and environmental microbiology* 63, 4784-4792.
- Emerson, D., and Weiss, J. V. (2004). Bacterial iron oxidation in circumneutral freshwater habitats: findings from the field and the laboratory. *Geomicrobiology Journal* 21, 405-414.
- Eusterhues, K., Rennert, T., Knicker, H., Kögel-Knabner, I., Totsche, K. U., and Schwertmann, U. (2010). Fractionation of organic matter due to reaction with ferrihydrite: coprecipitation versus adsorption. *Environmental science & technology* 45, 527-533.
- Eusterhues, K., Wagner, F. E., Häusler, W., Hanzlik, M., Knicker, H., Totsche, K. U., Kögel-Knabner, I., and Schwertmann, U. (2008). Characterization of ferrihydrite-soil organic matter coprecipitates by X-ray diffraction and Mossbauer spectroscopy. *Environmental science & technology* 42, 7891-7897.
- Ferris, F. G. (2005). Biogeochemical Properties of Bacteriogenic Iron Oxides. *Geomicrobiology Journal* 22, 79-85.
- Fortin, D., and Langley, S. (2005). Formation and occurrence of biogenic iron-rich minerals. *Earth-Science Reviews* 72, 1-19.
- Fu, H., and Quan, X. (2006). Complexes of fulvic acid on the surface of hematite, goethite, and akaganeite: FTIR observation. *Chemosphere* 63, 403-410.
- Grafe, M., Eick, M., and Grossl, P. (2001). Adsorption of arsenate (V) and arsenite (III) on goethite in the presence and absence of dissolved organic carbon. *Soil Science Society of America Journal* 65, 1680-1687.
- Gu, B., Schmitt, J., Chen, Z., Liang, L., and McCarthy, J. F. (1994). Adsorption and desorption of natural organic matter on iron oxide: mechanisms and models. *Environmental Science & Technology* 28, 38-46.

- Gu, B., Schmitt, J., Chen, Z., Liang, L., and McCarthy, J. F. (1995). Adsorption and desorption of different organic matter fractions on iron oxide. *Geochimica et Cosmochimica Acta* 59, 219-229.
- Heckman, K., Vazquez-Ortega, A., Gao, X., Chorover, J., and Rasmussen, C. (2011). Changes in water extractable organic matter during incubation of forest floor material in the presence of quartz, goethite and gibbsite surfaces. *Geochimica et Cosmochimica Acta* 75, 4295-4309.
- Hitchcock, A., Obst, M., Wang, J., Lu, Y., and Tyliczszak, T. (2012). Advances in the detection of As in environmental samples using low energy X-ray fluorescence in a scanning transmission X-ray microscope: arsenic immobilization by an Fe (II)-oxidizing freshwater bacteria. *Environmental science & technology* 46, 2821-2829.
- Jacobsen, C., Wirick, S., Flynn, G., and Zimba, C. (2000). Soft X-ray spectroscopy from image sequences with sub-100 nm spatial resolution. *Journal of Microscopy* 197, 173-184.
- Jambor, J. L., and Dutrizac, J. E. (1998). Occurrence and constitution of natural and synthetic ferrihydrite, a widespread iron oxyhydroxide. *Chemical Reviews* 98, 2549-2586.
- Jilling, A., Keiluweit, M., Contosta, A. R., Frey, S., Schimel, J., Schneck, J., Smith, R. G., Tiemann, L., and Grandy, A. S. (2018). Minerals in the rhizosphere: overlooked mediators of soil nitrogen availability to plants and microbes. *Biogeochemistry* 139, 103-122.
- Kaiser, K., and Guggenberger, G. (2000). The role of DOM sorption to mineral surfaces in the preservation of organic matter in soils. *Organic geochemistry* 31, 711-725.
- Kaiser, K., and Guggenberger, G. (2003). Mineral surfaces and soil organic matter. *European Journal of Soil Science* 54, 219-236.
- Kleber, M., Eusterhues, K., Keiluweit, M., Mikutta, C., Mikutta, R., and Nico, P. S. (2015). Chapter one-mineral-organic associations: formation, properties, and relevance in soil environments. *Advances in agronomy* 130, 1-140.

- Kleber, M., Sollins, P., and Sutton, R. (2007). A conceptual model of organo-mineral interactions in soils: self-assembly of organic molecular fragments into zonal structures on mineral surfaces. *Biogeochemistry* 85, 9-24.
- Kleinert, S., Muehe, E. M., Posth, N. R., Dippon, U., Daus, B., and Kappler, A. (2011). Biogenic Fe (III) minerals lower the efficiency of iron-mineral-based commercial filter systems for arsenic removal. *Environmental science & technology* 45, 7533-7541.
- Koch, B., and Dittmar, T. (2006a). From mass to structure: An aromaticity index for high-resolution mass data of natural organic matter. *Rapid communications in mass spectrometry* 20, 926-932.
- Koch, B. P., and Dittmar, T. (2006b). From mass to structure: an aromaticity index for high-resolution mass data of natural organic matter. *Rapid Communications in Mass Spectrometry* 20, 926-932.
- Kujawinski, E. B., and Behn, M. D. (2006). Automated analysis of electrospray ionization Fourier transform ion cyclotron resonance mass spectra of natural organic matter. *Analytical chemistry* 78, 4363-4373.
- Lalonde, K., Mucci, A., Ouellet, A., and Gélinas, Y. (2012). Preservation of organic matter in sediments promoted by iron. *Nature* 483, 198-200.
- Lerotic, M., Jacobsen, C., Gillow, J., Francis, A., Wirick, S., Vogt, S., and Maser, J. (2005). Cluster analysis in soft X-ray spectromicroscopy: finding the patterns in complex specimens. *Journal of Electron Spectroscopy and Related Phenomena* 144, 1137-1143.
- Lv, J., Miao, Y., Huang, Z., Han, R., and Zhang, S. (2018). Facet-Mediated Adsorption and Molecular Fractionation of Humic Substances on Hematite Surfaces. *Environmental science & technology* 52, 11660-11669.
- Lv, J., Zhang, S., Wang, S., Luo, L., Cao, D., and Christie, P. (2016). Molecular-scale investigation with ESI-FT-ICR-MS on fractionation of dissolved organic matter induced by adsorption on iron oxyhydroxides. *Environmental science & technology* 50, 2328-2336.

- McKnight, D. M., Bencala, K. E., Zellweger, G. W., Aiken, G. R., Feder, G. L., and Thorn, K. A. (1992). Sorption of dissolved organic carbon by hydrous aluminum and iron oxides occurring at the confluence of Deer Creek with the Snake River, Summit County, Colorado. *Environmental science & technology* 26, 1388-1396.
- Meier, M., Namjesnik-Dejanovic, K., Maurice, P. A., Chin, Y.-P., and Aiken, G. R. (1999). Fractionation of aquatic natural organic matter upon sorption to goethite and kaolinite. *Chemical geology* 157, 275-284.
- Mikutta, R., Mikutta, C., Kalbitz, K., Scheel, T., Kaiser, K., and Jahn, R. (2007). Biodegradation of forest floor organic matter bound to minerals via different binding mechanisms. *Geochimica et Cosmochimica Acta* 71, 2569-2590.
- Miot, J., Benzerara, K., Morin, G., Kappler, A., Bernard, S., Obst, M., Féraud, C., Skouri-Panet, F., Guigner, J.-M., and Posth, N. (2009a). Iron biomineralization by anaerobic neutrophilic iron-oxidizing bacteria. *Geochimica et cosmochimica Acta* 73, 696-711.
- Miot, J., Benzerara, K., Obst, M., Kappler, A., Hegler, F., Schädler, S., Bouchez, C., Guyot, F., and Morin, G. (2009b). Extracellular iron biomineralization by photoautotrophic iron-oxidizing bacteria. *Applied and Environmental Microbiology* 75, 5586-5591.
- Muehe, E. M., Scheer, L., Daus, B., and Kappler, A. (2013). Fate of Arsenic during Microbial Reduction of Biogenic versus Abiogenic As–Fe(III)–Mineral Coprecipitates. *Environmental Science & Technology* 47, 8297-8307.
- Niemeyer, J., Chen, Y., and Bollag, J.-M. (1992). Characterization of humic acids, composts, and peat by diffuse reflectance Fourier-transform infrared spectroscopy. *Soil Science Society of America Journal* 56, 135-140.
- Ohno, T., and Ohno, P. E. (2013). Influence of heteroatom pre-selection on the molecular formula assignment of soil organic matter components determined by ultrahigh resolution mass spectrometry. *Analytical and bioanalytical chemistry* 405, 3299-3306.
- Ohno, T., Parr, T. B., Gruselle, M. C. c. I., Fernandez, I. J., Sleighter, R. L., and Hatcher, P. G. (2014). Molecular composition and biodegradability of soil organic matter: a case study comparing two New England forest types. *Environmental science & technology* 48, 7229-7236.

- Rentz, J. A., Turner, I. P., and Ullman, J. L. (2009). Removal of phosphorus from solution using biogenic iron oxides. *Water research* 43, 2029-2035.
- Riedel, T., Biester, H., and Dittmar, T. (2012). Molecular fractionation of dissolved organic matter with metal salts. *Environmental science & technology* 46, 4419-4426.
- Riedel, T., Zak, D., Biester, H., and Dittmar, T. (2013). Iron traps terrestrially derived dissolved organic matter at redox interfaces. *Proceedings of the National Academy of Sciences* 110, 10101-10105.
- Rillig, M. C., Caldwell, B. A., Wösten, H. A., and Sollins, P. (2007). Role of proteins in soil carbon and nitrogen storage: controls on persistence. *Biogeochemistry* 85, 25-44.
- Schmidt, M. W., Torn, M. S., Abiven, S., Dittmar, T., Guggenberger, G., Janssens, I. A., Kleber, M., Kögel-Knabner, I., Lehmann, J., and Manning, D. A. (2011). Persistence of soil organic matter as an ecosystem property. *Nature* 478, 49-56.
- Sleighter, R. L., Chen, H., Wozniak, A. S., Willoughby, A. S., Caricasole, P., and Hatcher, P. G. (2012). Establishing a measure of reproducibility of ultrahigh-resolution mass spectra for complex mixtures of natural organic matter. *Analytical chemistry* 84, 9184-9191.
- Solomon, D., Lehmann, J., Harden, J., Wang, J., Kinyangi, J., Heymann, K., Karunakaran, C., Lu, Y., Wirick, S., and Jacobsen, C. (2012). Micro- and nano-environments of carbon sequestration: Multi-element STXM-NEXAFS spectromicroscopy assessment of microbial carbon and mineral associations. *Chemical geology* 329, 53-73.
- Sowers, T., Adhikari, D., Wang, J., Yang, Y., and Sparks, D. L. (2018). Spatial associations and chemical composition of organic carbon sequestered in Fe, Ca, and organic carbon ternary systems. *Environmental science & technology*.
- Sowers, T. D., Harrington, J. M., Polizzotto, M. L., and Duckworth, O. W. (2017). Sorption of arsenic to biogenic iron (oxyhydr) oxides produced in circumneutral environments. *Geochimica et Cosmochimica Acta* 198, 194-207.
- Sparks, D. L. (2003). "Environmental soil chemistry," Academic press.
- Sposito, G. (2008). "The chemistry of soils," Oxford university press.

- Stevenson, F. J. (1994). "Humus chemistry: genesis, composition, reactions," John Wiley & Sons.
- Stuckey, J. W., Goodwin, C., Wang, J., Kaplan, L. A., Vidal-Esquivel, P., Beebe, T. P., and Sparks, D. L. (2018). Impacts of hydrous manganese oxide on the retention and lability of dissolved organic matter. *Geochemical transactions* 19, 6.
- Whitaker, A. H., Amor, M., Pena, J., and Duckworth, O. W. (2018). Cr (VI) Uptake and Reduction by Biogenic Iron (Oxyhydr) oxides. *Environmental Science: Processes & Impacts*.
- Whitaker, A. H., and Duckworth, O. W. (2018). Cu, Pb, and Zn Sorption to Biogenic Iron (Oxyhydr) Oxides Formed in Circumneutral Environments. *Soil Systems* 2, 18.

## Chapter 4

### ADVANCED SPATIALLY-RESOLVED ANALYSIS OF PERMAFROST ORGANO-MINERAL ASSOCIATIONS

#### 4.1 Introduction

As uncertainty regarding future global climatic conditions increases and global temperatures rise (Kjellström et al., 2018; New et al., 2011; Rogelj et al., 2018), the importance of understanding terrestrial carbon sinks is paramount. Permafrost soils currently are estimated to sequester approximately 1700 Pg C across all depths (Drake et al., 2015; Schuur et al., 2008). Across this depth range, permafrost soils store 1035 Pg C in the top 3 m of soil (Schuur et al., 2015), which is an astounding ~50% of the current estimate for global soil C storage within the surface 3 m (~2100 Pg C) (Scharlemann et al., 2014). Rising temperatures increases the depth of the active layer, soil zone representing the area of freeze-thaw that is not perennially frozen, and results in a larger soil carbon fraction that is available for biodegradation (Drake et al., 2015; Schuur et al., 2015; Waldrop et al., 2010). Although previously thought to be more resistant to biodegradation, recent research has revealed high labile C fractions released from thawing permafrost soils (Burkert et al., 2019; Drake et al., 2015; Waldrop et al., 2010). In addition to increased C availability for soil microbial

decomposition and subsequent release to the atmosphere via respiration, thawing permafrost may contribute to the loading of C in aquatic systems (Drake et al., 2015; Schuur et al., 2015); therefore, elevated global temperatures are making C mass budget calculation increasingly challenging as both terrestrial and aquatic C cycling processes are being affected by the thawing of the massive C stock represented by permafrost systems.

Discontinuous permafrost areas, representing land where 50 to 90% of the surface landscape is in permafrost conditions (Schuur et al., 2008), are particularly sensitive to current increases in global temperature (Osterkamp and Romanovsky, 1999), with the Yedoma complex being one of the most sensitive to thaw (Schuur et al., 2008; Schuur et al., 2015). The Yedoma region consists of ancient permafrost zones that developed from the deposition of high organic matter (OM) loess, consisting of wind-blown soil with high silt content (Drake et al., 2015; Pewe and Sellmann, 1973). Up to 500 Pg C is suspected to be sequestered in the Yedoma region (Schuur et al., 2015), making this a major pool controlling permafrost feedbacks to the atmosphere. High sensitivity to thaw and recently observed high biodegradation of thawed Yedoma permafrost C to CO<sub>2</sub> makes understanding the stabilization of this zone critical to predicting C mass balance in a changing climate. However, investigations of the Yedoma regions have primarily focused on studying ancient microbial communities and the biodegradability of dissolved OC release from thawed

permafrost (Burkert et al., 2019; Drake et al., 2015; Waldrop et al., 2010), with limited characterization of thawed solid phases (Burkert et al., 2019; Sellmann, 1972). This current research has revealed striking observations of high OC biodegradability, with one study reporting a 53% decrease in OC (87% of which was low-molecular-weight) over a 200 hr period after thaw (Drake et al., 2015). The high lability of OM reported in this study exemplifies the need for understanding how soil phases (i.e., Fe oxides, aluminosilicates, etc.) impact C sequestration or release processes. Understanding microbial processes in these systems is critical as it will significantly affect C emissions from thawing permafrost; however, the associations of C with metal oxides and aluminosilicates in permafrost systems is poorly understood and may have far-reaching implications to C cycling post-thaw.

In addition to microbial communities, composition of OM and organo-mineral associations significantly mediate C sequestration or transformation processes in terrestrial and aquatic systems (Bolan et al., 2011; Davidson et al., 2000; Schmidt et al., 2011). The importance of organo-mineral processes in the global C cycle is exemplified by the intensification of research investigating the relationship of OM with metal oxides and aluminosilicates in the past 20 years (Chen et al., 2014b; Gu et al., 1994; Gu et al., 1995; Lalonde et al., 2012; Lehmann et al., 2007), and has recently employed the use of advanced X-ray absorption spectroscopic and Fourier transform infrared cyclotron mass spectrometric techniques to elucidate OM sequestration

mechanisms and molecular fractionation (Chen and Sparks, 2015; Coward et al., 2018; Lv et al., 2016; Sowers et al., 2018a; Sowers et al., 2019). For example, scanning transmission X-ray microscopy-near-edge X-ray absorption fine structure (STXM-NEXAFS) spectroscopy of soils and Fe oxides at various redox states has found high co-association of Fe/C and C/Ca (Chen et al., 2015; Chen and Sparks, 2015; Sowers et al., 2018a; Wan et al., 2007), with both STXM-NEXAFS and FT-ICR-MS OC revealing organic compounds rich with carboxylic moieties and/or aromatics being highly sorbed to Fe oxide phases (Avneri-Katz et al., 2017; Coward et al., 2018; Lv et al., 2016; Sowers et al., 2019). Understanding moiety-scale interactions of OM with reactive solid phases provides a critical window into the primary controls dictating C sequestration (Sparks, 2003; Sposito, 2008); therefore, applying advanced spectroscopic investigation to OM and Fe oxides in permafrost soils will provide a needed window into the mechanisms driving OM stability or lability.

Due to the sensitivity of the Yedoma region to thaw and subsequent OM biodegradation (Drake et al., 2015; Schuur et al., 2015), we sought to elucidate the OM speciation and organo-mineral relationships of soil metal oxide and aluminosilicate minerals in permafrost samples immediately upon thaw from the Yedoma zone at the Fox Permafrost Tunnel in Fairbanks, Alaska. To address this knowledge gap, we performed STXM-NEXAFS spectroscopic experiments across a permafrost chronosequence in the Fox Permafrost Tunnel and above the tunnel to 1)

determine heterogeneity of OC speciation across Yedoma permafrost soils and 2) unearth organo-mineral associations and sequestration mechanisms of thawed permafrost Fe oxides and aluminosilicate minerals.

## **4.2 Materials and Methods**

### **4.2.1 Collection and Preparation of Permafrost Samples**

Permafrost samples were collected from within and above the Fox Permafrost Tunnel (PT) (Figure 4.1) located north of Fairbanks, Alaska 64.951°N, -147.621°W (Burkert et al., 2019; Hamilton et al., 1988). The tunnel is operated by the US Army Corps of Engineers Cold Region Research and Engineering and Laboratory (CREEL), which is under the Engineer Research and Development Center. The Fox PT was excavated 55 years ago, with the main tunnel stretching approximately 100 m into a hillside and 15 m below the ground surface (Hamilton et al., 1988; Sellmann, 1972). The temperature of the tunnel is maintained below freezing naturally during Winter months and refrigerated to approximately -2.5°C to -3°C during temperate months (Douglas et al., 2011; Hamilton et al., 1988). Permafrost within the tunnel is characterized as Yedoma, OM-containing Pleistocene-age permafrost, and is dominated by ancient wind-deposited silt (Douglas et al., 2011; Sellmann, 1972). The horizontal excavation of the tunnel represents a chronosequence ranging up to approximately 40,000 y B.P (Douglas et al., 2011; Pewe and Sellmann, 1973).

We collected PT samples in triplicate on August 28, 2018 at 10 m, 52 m, and 94 m from the tunnel entrance, which has been previously radiocarbon-dated as approximately 19, 27, and 36 ky B.P., respectively (Douglas et al., 2011; Mackelprang et al., 2017). A 10 cm diameter x 5 cm deep keyhole saw attached to a power drill was used to collect samples, similar to past methods used for collecting permafrost samples from the Fox PT (Mackelprang et al., 2017). Triplicate permafrost samples above the tunnel (AT) were collected the previous day (August 27, 2019) at a depth range of 120-147 cm using a SIPRE coring auger. Samples from both days were kept frozen at CREEL (-20°C) and same-day shipped (frozen) in two 65-quart Otterbox coolers to the University of Delaware Harker Interdisciplinary Science and Engineering Laboratory.

Permafrost cores were sectioned using a bandsaw and the exterior was shaved by approximately 2 cm using a sterilized cartilage knife to remove any exterior debris that may be present due to the drilling process. A subsample of the sections was thawed at 30°C in a water bath and solid phase was separated via centrifugation at 10,000 g. Wet paste samples were freeze-dried prior to STXM analysis and characterization analyses. Subsamples of all permafrost samples were analyzed on a vario Micro cube CHNS analyzer to determine solid phase concentration of C, N, and sulfur, with solid phase metal concentrations being determined using a microwave digestion performed according to EPA Method 3051 (EPA, 2007). Percent

concentrations of measured in elements in thawed soil solid phases are reported in Table 4.1.

#### **4.2.2 Scanning Transmission X-ray Microscopy**

Beamline 10ID-1 at the Canadian Light Source (Saskatoon, Saskatchewan) was utilized to prepare and analyze all thawed permafrost samples using STXM-NEXAFS. Samples were analyzed via a similar method previously published by the authors (Chen et al., 2014a; Sowers et al., 2018a). Approximately 1 mg of recently freeze-dried permafrost was suspended in 1 mL of deionized (DI) water, sonicated for 30 s, and approximately 3  $\mu$ L of sonicated soil was deposited on a Si<sub>3</sub>N<sub>4</sub> window. This was repeated 1-2 times until the window was full. All Si<sub>3</sub>N<sub>4</sub> windows were placed onto a multisample holder and mounted in the STXM chamber. Samples were analyzed at a 1/6 atm of helium (He) and measured using a 25 nm Fresnel zone plate, enhancing maximum spatial resolution (approximately 30 nm).

After locating regions of interest at low magnification (approximately 2500  $\mu$ m<sup>2</sup>) and focusing the microscope on regions having acceptable thickness at the C K-edge (288 eV), samples were raster scanned using synchrotron X-rays across an eV range capturing C 1s, Ca 2p, Fe 2p, Al 1s, and Si 1s NEXAFS data. For soil PT\_B, Al and Si were not analyzed due to beamtime constrictions. Carbon, Ca, and Fe were scanned in order from 280 to 735 eV, followed by Al and Si analysis from 1555 to

1860 eV. Stack measurements for each element were obtained with dwell times of 1–1.5 ms and with pixel sizes from 40 to 80 nm.

#### **4.2.3 STXM-NEXAFS Data Processing and Principal Component Analysis**

Data processing was performed according to methods established in Sowers et al. (2018a). All data stacks were aligned using Stack Analyze (Stony Brook, V2.7) and processed using the aXis2000 software package (Hitchcock; Jacobsen et al., 2000).

After alignment and identifying  $I_0$  (incident flux), aXis2000 was used to convert aligned and stacked image data to optical density using the following equation:  $OD = \ln(I_0/I)$ , where  $I$  is equal to the flux transmitted through the sample. Generated images up to  $\pm 0.5$  eV of the resonance energy for each element were averaged for chemical mapping. The averaged images at each element's resonance energies were subtracted with averaged images at the elements' specific pre-edge range (Table 4.2) in order to obtain chemical maps.

Principal component analysis, along with corresponding cluster analysis, was performed to identify soil regions of statistically unique elemental spectra. PCA and cluster analysis was performed using PCA GUI 1.1.1 software (Lerotic et al., 2005). Four to five components were used when beginning the search for significant components and then sequentially lowered until significant, element-specific features between two components were congruent. An eigenimage scaling factor of 0.3 was

used for all cluster analyses and singular value decomposition was performed when analyzing cluster spectra. PCA data is limited to C and Fe as PCA revealed a lack of multiple, unique regions for Ca, Al, and Si.

### **4.3 Results and Discussion**

#### **4.3.1 RGB and Optical Density Correlations for C, Ca, Fe**

All permafrost samples across the permafrost tunnel chronosequence (PT\_A, B, and C) and above the tunnel (AT) were qualitatively and quantitatively analyzed for C, Ca, and Fe using STXM optical density maps (Figures 4.2-4.5). The mixture of red, green, and blue for the RGB optical density maps indicate the presence of C, Ca, and Fe, respectively and provide insight into elemental co-associations. All permafrost samples were observed to be Fe-rich, as showcased by Figures 4.2A & C and 4.3A & C. RGB plots in Figure 4.2 & 4.3 showed a high proportion of purple, indicating co-association of C and Fe for PT\_A and PT\_C. Similar purple features representative of high C and Fe co-association have been observed in many other STXM investigations of OM-bearing Fe oxides in previous work (Chen et al., 2014b; Sowers et al., 2018a; Sowers et al., 2019). Therefore, Fe oxides appear to be provide a major framework for C retention in this soil system. However, this trend was not observed for the PT\_B and AT maps. Large red regions for PT\_B and thin red coatings for AT were found attached to expansive blue, Fe-rich areas, suggesting the presence of OM aggregated

around Fe-rich particles. Interestingly, previous research investigating a Phaeozem saw both co-association features and features suggesting OM aggregation (Wan et al., 2007). All permafrost soils are similar in soil chemical characteristic to the Phaeozem tested, which are circumneutral soils containing high base cations, due to a shared parent material of loess/glacial till (Targulian and Krasilnikov, 2007). Therefore, parent material may have a significant effect on observed organo-mineral associations.

Calcium was also found to highly co-associate with C for soils PT\_A (Figure 4.2B) and PT\_B (Figure 4.2D). White coatings observed for PT\_A suggest similar contributions of C, Ca, and Fe, which is similar to previous observations observed for OM sorbed to ferrihydrite in the presence of Ca (Sowers et al., 2018a; Sowers et al., 2018b). This observation is a new component in a growing body of work suggesting that ternary complex formation facilitated through Ca-bridging may be playing a significant role in terrestrial organo-mineral complexes (Chen et al., 2014a; Kramer and Chadwick, 2018; Sowers et al., 2018a; Wan et al., 2007). Interestingly, only the presence of yellow regions and coatings, representative of C and Ca co-association, were observed for soil PT\_B and AT (Figure 4.2D). This observation is closely related to what was observed by Wan et al. (2007) for a Phaeozem soil and Chen et al. (2014a) for a pasture Ultisol. No evidence of ternary associations were observed for PT\_B, unlike PT\_A, and potentially indicates that Ca may impact C cycling via multiple mechanisms that needs to be further explored. Soil PT\_C (Figure 4.3B) was

found to dominantly consists of green shades, with areas of seemingly high Ca and Fe co-association. In Figure 4.3A, we can more clearly observe C and Fe co-association at distinct regions of the particles shown; however, Ca seems to dominate a majority of the map. Therefore, Ca is likely coating Fe-rich particles seen in Figure 4.3B, or may contain a combination of Ca or Fe minerals (e.g., aragonite or siderite, respectively).

Spatially-resolved correlations of elemental co-associations were quantitatively identified using OD correlation plots (Figure 4.4 & 4.5) for all PT soils, with the AT soil being excluded due to sample thickness effects skewing OD values (Wan et al., 2007). We found a positive linear correlation between C and Fe for soils PT\_A and PT\_C (Figure 4.2A & C, respectively), which corroborates our interpretation that pervasive purple regions observed in 4.2A and 4.3C are areas of high C-Fe organo-mineral associations. Conversely, poor correlation between C and Fe for PT\_A was observed (Figure 4.4B). This result was expected, due to the presence of a high C region, likely representing an OM aggregate (Lehmann et al., 2007; Lehmann et al., 2008), surrounding an Fe particle observed in Figure 4.2C. Similar to past investigations, Ca and C optical density were found to correlate for soils PT\_A and PT\_B (Figure 4.4D & E) (Chen et al., 2014a; Chen and Sparks, 2015; Wan et al., 2007). However, the correlation coefficients for PT\_A and PT\_B ( $R^2 = 0.54$  &  $0.51$ , respectively) is lower than past observations of optical density correlation plots for C

and Ca published for soils, which showed correlations of 0.77 and 0.87 for Mollisols (Wan et al., 2007) and Ultisols (Chen et al., 2014a), respectively. This disparity is likely due to the unique soil chemical conditions fostered by the PT, such as unique Fe, Al, or Si speciation/phases, and will be discussed later using NEXAFS.

Additionally, soil PT\_A was observed to have positive correlation of both C/Ca and C/Fe, and was also the only sample that was observed to contain distinct white regions (Figure 4.2B) characteristic of C, Ca, and Fe ternary association for all samples tested. STXM RGP map and optical density correlation data for soil PT\_A is similar to previously published results for Fe-Ca-C ternary complexes formed through sorption and/or coprecipitation processes (Adhikari et al., 2019; Chen et al., 2014a; Sowers et al., 2018a), providing compelling evidence that Fe, Ca, OM ternary complexes may be integral to permafrost soils in the Yedoma region. Although C and Ca are positively correlated for soil PT\_B, the relationship of C, Ca, and Fe is suspected to differ due to the lack of a correlation observed for C and Fe. The co-association of Ca with C without correlation to Fe suggests that the presence of Ca may impact OM chemical processes. Results for soil PT\_B compared to PT\_A suggests that permafrost soils have heterogenous organo-mineral associations that are potentially affected by the presence of Ca, providing evidence that Ca, and potentially other polyvalent cations, may be critically important when assessing C transformation processes in permafrost systems. We found low correlation of C and Ca (Figure 4.4E), but high correlation of

Fe and Ca (Figure 4.5) for soil PT\_C. This supports our previous conclusions drawn from Figure 4.3B that Ca is likely coating an Fe mineral particle, with localized spots where either Fe or Ca is interacting with OM.

#### **4.3.2 RGB and Optical Density Correlations for C, Al, Si**

Similar to Figures 4.2-4.5, STXM RGB optical density maps and corresponding elemental optical density correlations were used to investigate the relationship of C with aluminum (Al) and silicon (Si) for permafrost soils (Figures 4.6 & 4.7). We found no purple or yellow regions that would be indicative of high partitioning of C with Si or Al, respectively, for all RGB maps (Figure 4.6). Additionally, red regions were distinctively separated from areas containing Al, Si, or both, with all permafrost soils having at least one particle with no observable C on the RGB optical density map. However, Al and Si were found to be more closely related, which is observable for soils PT\_C and AT (PT\_A not shown due to thickness effects) from spatially-resolved optical density correlation plots (Figure 4.7). Silicon and Al were found to have an average Si:Al ratio of approximately 1.4 and 2.5 for the optical density maps of soils PT\_C and AT, respectively (Figure 4.7A & B, respectively). The spatially-resolved optical density ratio of Si and Al has been commonly used in the past to provide evidence of the presence of aluminosilicates in soils (Chen et al., 2014a; Wan et al., 2007). Typically, aluminosilicates consist of one octahedrally-

coordinated Al sheet aligned with either one or two tetrahedrally-coordinated Si sheet(s), forming either a 1:1 or 2:1 layer silicate mineral, respectively (Sparks, 2003; Sposito, 2008). Therefore, we assert that aluminosilicates are present in all permafrost soils tested and that soil PT\_C consists of a mixture of 1:1 and 2:1 aluminosilicate minerals. Past X-ray diffraction analysis of Fox Tunnel PT samples, collected at sites similar to this study, has previously been performed to investigate the clay mineralogy. Sellman (1972) found that Fox Tunnel PT samples were dominated by a mixture of montmorillonite (2:1 aluminosilicate) and kaolinite (1:1 aluminosilicate); therefore, STXM results provide corroborative evidence that a mixture of 1:1 and 2:1 aluminosilicates are present. Additionally, a Si:Al ratio of 1.8 and 1.7 identified through STXM elemental optical density correlations has been found for soils containing predominately 2:1 aluminosilicates (Chen et al., 2014a; Chen and Sparks, 2015; Wan et al., 2007), emphasizing the mixture of aluminosilicates present in the PT system. Soil AT likely consists of primarily 2:1 aluminosilicate minerals and quartz grains due to the Si:Al ratio exceeding two. Substitution of Fe for Al could also explain an increase in Si:Al ratio (Wan et al., 2007), as Fe was found to be associated with areas having Al/Si co-association when comparing STXM RGB optical density plots in Figure 4.4 versus Figure 4.6; however, a majority of these regions are suspected to be Fe coatings since no discrete Fe particles were observed separate from Si/Al particles that are likely representative of aluminosilicates (Chen et al., 2014a).

The combination of STXM RGB maps and OD correlation plots for the PT and AT soils provides evidence that Al and Si, separately and/or as aluminosilicates, is not a directly critical component of permafrost soil organo-mineral interactions. This result is contradictory to what has observed in previous STXM investigations of Ultisol systems. For example, Wan et al. (2009) and Chen et al. (2014a) observed C optical density to be well-correlated with Al and Si, having C to Si/Al linear correlation coefficients of 0.81 and 0.72, respectively, whereas we found no observable optical correlation between C and Si/Al. A similar lack of correlation between C and Si/Al was reported by Wan et al. (2009) for a Cambisol. Likeness of the permafrost soils to a Cambisol is sensible since Cambisols are “young” soils with little development progressing past the parent material (Targulian and Krasilnikov, 2007). Freezing temperatures associated with the permafrost soils promotes slow soil development and PT soils are predominately preserved loess (parent material) (Targulian and Krasilnikov, 2007); therefore, the relative of the age of these soils may contribute to the disparity of C interactions with Si/Al relative to previously observed STXM investigations of soils.

Interestingly, the shared lack of overlapping regions between C and Al/Si for both PT and AT soils suggests that the ratio of Si/Al, serving as a proxy for the proportion of 1:1 versus 2:1 aluminosilicate minerals, did not impact C associations. This outcome was surprising, as soils with higher proportion of 2:1 aluminosilicates

are commonly observed to possess higher reactivity for OM due to increased surface and interlayer activity. However, Fe oxides are likely responsible for this result. Soil aluminosilicates are known to possess considerably less reactivity for OM compared to Fe oxide minerals (Kaiser and Guggenberger, 2000; Mikutta et al., 2007); therefore, we suspect that high association of C with Fe oxides for all permafrost soils is antagonistically affecting the association of C with Si and/or Al. Although the STXM evidence provides a convincing argument for the lack of direct organo-mineral association of C with aluminosilicate minerals, aluminosilicates remain indirectly critical to the facilitation of metal oxide-OM relationships. As previously discussed, Fe oxides are expected to coat aluminosilicate particles due to the dependence of Fe regions on the presence of a larger Si/Al region. STXM RGB optical maps in Figure 4.4 and 4.6 indicate that Fe surface coated-aluminosilicates are highly associated with C and C/Ca particles; therefore, aluminosilicate minerals, Fe oxide minerals, and C have a dynamic relationship dictated by physical and chemical factors that represent the potential complexity of organo-mineral associations in one of the world's largest C sinks. These conclusions are congruent with past STXM-focused studies showcasing the dual importance of soil aluminosilicate physical and chemical features to C cycling processes (Lehmann and Solomon, 2010; Solomon et al., 2012b). Future investigations of the heterogeneity and stability of these relationships are necessary for accurate C modeling in a changing climate.

### 4.3.3 Carbon NEXAFS and PCA

Carbon speciation and spatial heterogeneity was explored using C 1s NEXAFS and principal component analysis (PCA) for all permafrost soils (Figure 4.8A-F). Prior to performing PCA, STXM-NEXAFS maps averaged at the C pre-edge (280-282 eV) were subtracted from maps averaged at the C K-edge peak of greatest intensity (287.7-288.7 eV) to avoid the inclusion of unwanted regions that are too thick and may distort spectra, which was repeated for all elements analyzed (Table 4.2). Distinct map regions, or pixel clusters, possessing statistically unique spectra were identified for each permafrost soil via PCA, allowing for the spatial assignment of functional groups dependent on observed resonance energies (Table 4.3). Yellow clusters were excluded from the following discussion as these were too thick for C analysis.

Variations in C speciation were observed for all permafrost soils across the tested chronosequence, along with C compositional micro-heterogeneity for each soil. For all soils, we observed the presence of aromatic and carboxylic moieties (peak (i) at 285.2-285.6 eV and peak (v) at 288.5 eV, respectively). This result was expected as aromatic and carboxylic moieties are commonly found in soils (Chen et al., 2014b; Lehmann and Solomon, 2010; Lehmann et al., 2008; Solomon et al., 2012b; Wan et al., 2007), especially those containing metal oxide (i.e., Fe oxide) minerals (Chen et al., 2014b; Sowers et al., 2018a). However, the intensity and distortion of aromatic and carboxylic peaks varied by permafrost sample and cluster. For PT\_A\_1 (red) and

PT\_A\_2 (green) (Figure 4.8A and B), we observed both clusters to have intense aromatic and aliphatic (peak (iii) at 287.5) peaks. Also, both were observed to have an amide-carbonyl peak at 288.1 eV (peak (iv)), representing the presence of a proteinaceous structure that was seemingly more present in cluster PT\_A\_1 (Chen and Sparks, 2015; Liang et al., 2006; Solomon et al., 2012a). Carboxylic moieties were found to have higher intensity for cluster PT\_A\_2 compared to cluster PT\_A\_1. Interestingly, cluster PT\_A\_2 is in alignment with the white, ternary regions identified in Figure 4.2B, suggesting that OC associated with carboxylic moieties may facilitate potential Ca-bridged complexes (Chen et al., 2014b; Chen et al., 2015; Sowers et al., 2018a). Carboxylic moieties were similarly found to be integral to proposed ternary complex development in previous studies of systems containing Fe(III) oxides, Ca, and OM (Adhikari et al., 2019; Sowers et al., 2018a). Cluster PT\_A\_1 was found to have a small feature at 290.1 eV (peak (vi)), unlike cluster PT\_A\_2, which is representative of the presence of carbonate. However, carbonate is not expected to be a major component in permafrost PT\_A due to the relatively low intensity at 290.1 eV compared to other features noted in Table 4.3.

Carbon speciation for soil PT\_B (Figure 4.8A and C) was found to be most heterogenous compared to other soils, as NEXAFS revealed more peaks and PCA revealed more unique spectral clusters. Aromatic and carboxylic moieties were distinctly observed for all clusters. In addition to aromatic and carboxylic moieties,

cluster PT\_B\_1 (red) and cluster PT\_B\_2 (green) was observed to possess spectral features corresponding to phenolic (peak (ii) at 286.7-286.9 eV) and aliphatic moieties, whereas cluster PT\_B\_3 (purple) was found to have phenolic, aliphatic, and amide-carbonyl functional groups. Surprisingly, all clusters for soil PT\_B were found to have phenolic moieties whereas none were observed for soil PT\_A. Phenolic moieties are commonly found in soil OM, which has especially been reported in temperate soil systems (Chen and Sparks, 2015; Kaiser and Guggenberger, 2003; Wan et al., 2007). Excluding the presence of phenolic moieties, the C spectra for cluster PT\_B\_1 corresponds well to observed spectra for soil PT\_A. However, cluster PT\_B\_3 was found to be highly unique from all spectra observed for other analyzed permafrost soils. The combination of a distinct aromatic peak and an intense, broad region from 287.5 to 288.5 is similar to C spectra for OM derived from fungi or microbial residues (Kinyangi et al., 2006; Liang et al., 2006). These compounds likely consist of C compounds resistant to biodegradation, consisting of melanin, lipids of cell walls, and/or chitin (Chen et al., 2014a; Chen and Sparks, 2015; Kinyangi et al., 2006; Liang et al., 2006). Cluster PT\_B\_2 was observed to have low signal throughout the tested eV range. This occurred most likely due to a low concentration of C, which is observable by the limited presence of red in Figure 4.2C.

Only one unique cluster was found for soil PT\_C (Figure 4.8A and D) due to a low degree of C heterogeneity observable by C NEXAFS. Additionally, there is a lack

of C moiety diversity compared to the other PT soils examined. Aromatic and carboxylic moieties were the only C NEXAFS features observed. Lack of C functional moiety diversity is likely a result of an advanced stage of OM degradation, where only aromatic, carboxylic, and/or carboxylic-associated aromatic groups remain due to stabilization facilitated by metal oxides and other soil minerals (Burkert et al., 2019; Chen et al., 2014b). Advanced OM degradation of soil PT\_C is plausible due to the increased age of the permafrost soil relative to the other PT soils (Figure 4.1; 36,000 y B.P. for PT\_C versus 27,000 and 19,000 y B.P. for PT\_B and PT\_A, respectively).

Similarly, both clusters for soil AT did not have as much C speciation diversity as PT\_A and PT\_B but were found to have an intense carboxylic peak with a shoulder at 289.5 eV, typical of an O-alkyl group (Chen et al., 2014a), along with a broad aromatic feature. This combination is consistent with polysaccharides, which are typically reported to be integral to soil OM physical (aggregation) and chemical (sorption) associations with clay and metal oxide minerals (Chen et al., 2014b; Coward et al., 2018; Kalbitz et al., 2003; McKnight et al., 1992; Sparks, 2003). Cluster AT\_2 has significantly lower intensity compared to cluster AT\_1 due to lower C concentration and potential thickness effects. The intense, distinct carboxylic peak for soil AT has been concluded in other STXM-NEXAFS soils studies to be representative of metal oxide mediated organo-mineral associations (Chen et al.,

2014b; Chen and Sparks, 2015) and compares well to the intensity of the carboxylic peak for the Fh\_DOM standard.

#### **4.3.4 Iron NEXAFS and PCA**

Spatial heterogeneity of Fe for the PT chronosequence and the AT soil (Figure 4.9) was investigated due to the importance of Fe to the transport and stabilization of C (Kalbitz et al., 2003; Kalbitz et al., 2000; Schmidt et al., 2011). For all permafrost samples, we observed peaks at 708, 710, 721, and 723 eV which correspond to Fe L<sub>3</sub>-edges (708 and 710 eV) and Fe L<sub>2</sub>-edges (721 and 723 eV). The Fe L<sub>3</sub>-edges at 708 and 710 eV provide insight into Fe speciation, with the relative intensity of the two edges indicating the proportion of Fe(II) versus Fe(III); however, a peak at both edges is present for both Fe species. This trend is observable for the FeO and Fe<sub>2</sub>O<sub>3</sub> standards included in Figure 4.9, with FeO (Fe(II)) having a dominant peak at 708 eV relative to 710 eV and Fe<sub>2</sub>O<sub>3</sub> having the dominant peak at 710 eV. We found variable Fe speciation for all permafrost soils analyzed using Fe NEXAFS and unique Fe oxidation state at micro-localized regions identified via PCA for a majority of the soils tested.

Soil PT\_A was found to have two unique Fe clusters (Figure 4.9A and B). PT\_A\_1 (red) and PT\_A\_2 (green) was dominantly composed of Fe(II), especially for cluster PT\_A\_2. Cluster PT\_A\_1 was found to have similar intensity peaks at 708 and

710 eV, indicating that this is a particle region of mixed Fe valence. However, Fe spectra for cluster PT\_A\_2 closely matched the FeO standard; therefore, this region is expected to be dominated by Fe(II). Soil PT\_B was found to primarily consist of Fe(III) for both spectra clusters (Figure 4.9A and C), with PT\_B\_1 (yellow) having more observable Fe(II) than PT\_B\_2 (red). Similar to the C NEXAFS, soil PT\_C was found to have only one unique Fe spectrum (Figure 4.9D) and well-aligned to the location of the C cluster in Figure 4.8D (Figure 4.9D). Cluster PT\_C\_1 was found to be seemingly entirely Fe(III), mimicking the Fe<sub>2</sub>O<sub>3</sub> standard. The Fe speciation of soil AT (Figure 4.9A and E) resembled spectral results for PT\_A, with two clusters in which cluster AT\_1 (red) had similar intensities at 708 and 710 eV indicative of mixed Fe(II)-Fe(III) valence and cluster AT\_2 (green) closely matched the Fe(II) standard (FeO). Iron identified in all maps is likely a combination of Fe minerals and Fe substituted in aluminosilicates as no separate Fe(II) or Fe(III) particles were observed (Chen et al., 2014a; Chen and Sparks, 2015).

For all permafrost soils tested, Fe minerals of all NEXAFS-observable valence states were found to be present and associated with soil OM. All regions with Fe(III), including regions with mixed valence state, were found to be associated with C when comparing Figure 4.9 with elemental optical density RGB maps (Figures 4.2 and 4.3) and PCA identified regions (Figure 4.8). Fe(III)-dominated minerals are known to highly co-associate with OM and form well-documented stabilization mechanisms

with OC (Chen et al., 2014b; Schmidt et al., 2011); therefore, sequestration of OM to Fe(III) minerals via strong, inner sphere complexes are expected to occur for all permafrost soils examined (Kleber et al., 2015; Sparks, 2003). Additionally, it is equally possible that Fe(III)-OM coprecipitates are in this system, which would be expected due to the presence of high ice content potentially indicating past fluctuations in redox conditions (Chen et al., 2014b; Douglas et al., 2011). Fe(III)-OM coprecipitates may also be represented by regions possessing mixed Fe valence state, as incomplete oxidation of Fe(II) before freezing may allow for physical encapsulation and/or surface sorption of Fe(II) in/to Fe(III)-OM coprecipitates (Chen et al., 2014b; Chen et al., 2015; Sodano et al., 2017). Coprecipitation of OM with Fe has been reported to be highly effective at sequestering OM (Adhikari et al., 2019; Chen et al., 2014b), making it likely an important component of OM preservation in frozen systems transitioning to active layer material. Surprisingly, regions that were dominantly Fe(II), such as soil PT\_A\_2, were also found to overlap with C regions (Figure 4.2A). The Fe NEXAFS spectra for PT\_A\_2 closely resembles Fe NEXAFS spectra for hydroxychloride green rust (Miot et al., 2014) and green rust is known to have reactivity for oxyanions (Grybos et al., 2009; Jönsson and Sherman, 2008); therefore, precipitated Fe(II)-minerals resembling green rusts may be an important contributor of OM sequestration. In summary, OM transformation and stability present in all permafrost soils is expected to be heavily dictated by the stability of Fe(III)-OM

sorption complexes and/or Fe(II/III)-OM coprecipitates. These results indicate the stability of potential Fe-OM complexes may heavily dictate C cycling processes in permafrost.

#### **4.3.5 Calcium NEXAFS**

Bulk Ca speciation was explored using Ca L-edge NEXAFS due to increasing evidence that Ca may be directly involved in environmental organo-mineral associations (Figure 4.10). Edges at 349.3 (ii) and 352.6 eV (iv) represent Ca L<sub>3</sub> 2P<sub>3/2</sub> and L<sub>2</sub> 2P<sub>1/2</sub> spin-orbital partners, and are each preceded by peaks of typically lower intensity at 348.2 (i) and 351.4 eV (iii). Soils were compared to CaCl<sub>2</sub>, Ca sorbed to extracellular polymeric substances (EPS) or ferrihydrite (Ca-EPS and Ca-Fh, respectively), and calcite. All soils were found to have edges at 349.3 and 352.6 eV, providing evidence for the presence of Ca as either a sorbed or mineral phase since these spectra did not align with L edges observed for the CaCl<sub>2</sub> standard (Chen et al., 2014a; Chen and Sparks, 2015; Sowers et al., 2018a). However, peak intensity preceding these edges varied among permafrost samples. Soils PT\_A and PT\_C were found to have higher intensity peaks at 348.2 and 351.4 eV compared to soils PT\_B and AT. Intensity of the Ca L-edges at 348.2 and 351.4 eV is positively correlated with increased Ca structure crystallinity (Politi et al., 2008), which is clearly demonstrated by the intense peaks for the calcite standard; therefore, soils PT\_A and

PT\_C are expected to partially contain crystalline forms of Ca (e.g, CaCO<sub>3</sub>) whereas Ca in PT\_B and PT\_C are solely in sorbed and/or amorphous phases. However, Ca spectra for calcite compared to soils PT\_A and PT\_C remain disparate, suggesting that Ca in these systems is dominantly in amorphous and/or poorly-crystalline states.

#### **4.3.6 Aluminum and Silicon NEXAFS**

Characterization of aluminosilicates and other potential Al and Si phases was investigated for permafrost samples. We found three characteristic peaks in the Al K-edge NEXAFS for our samples, located at 1565.6 (i), 1567.7 (ii), and 1570 eV (iii) (Figure 4.11). The presence of all three of these peaks is indicative of a mix of octahedrally- and tetrahedrally-coordinate Al, representative of 2:1 layer aluminosilicates (Chen et al., 2014a; Ildefonse et al., 1998; Shaw et al., 2009). The muscovite (2:1 aluminosilicate) standard showcases these features and closely resembles the spectra observed for soil AT. This result is congruent with conclusions made from Figure 4.7, where Si:Al ratio indicated a predominance of 2:1 aluminosilicates. Aluminum spectra for PT\_A and PT\_C are similar and have a distorted peak at 1567.7 eV with a relatively more intense peak at 1570 eV. This represents the relative increase of Al in the aluminosilicate thus 1:1 aluminosilicates are likely present as this increase would be lesser for a 2:1 due to a relative decrease in Al present per area (Chen and Sparks, 2015; Shaw et al., 2009). Therefore, this result,

in conjunction with Figure 4.7, indicates that both 2:1 and 1:1 aluminosilicates are present in PT soils. The presence of 2:1 and 1:1 aluminosilicates has also been observed via XRD analysis of the Fox Permafrost Tunnel (Sellmann, 1972). Silicon K-edge NEXAFS spectra for bulk permafrost samples revealed that Si present in all soils was predominantly in aluminosilicate phases due to peaks located at 1846.5 (i), 1850.4 (ii), and 1857.0 eV (iv). Distinguishment of specific 1:1 and/or 2:1 aluminosilicates using Si NEXAFS is unreliable and no evidence of chlorite or other 2:1:1 clay minerals were present in any of the soils (Chen et al., 2014a; Chen and Sparks, 2015; Shaw et al., 2009). Additionally, no significant peak was observed at 1854.6 eV (iii), suggesting quartz was not present to a high extent for all soils. However, a slight shift of peak (i) from 1846.5 to 1846.8 was observed for soil AT, which is similar to the quartz standard and is an agreement with the prior assertion that Si in quartz in soil AT may be driving the Si:Al ratio increase above 2:1 (Figure 4.7B) (Chen and Sparks, 2015; Shaw et al., 2009).

#### **4.4 Conclusions**

Our STXM-NEXAFS investigation of Yedoma region permafrost soil across a chronosequence revealed novel insights into organo-mineral relationships in the Arctic. Carbon and Fe are highly co-associated for the youngest (PT\_A) and oldest (PT\_B) permafrost tunnel samples; however, organic matter was aggregated around Fe for

PT\_B suggesting that physical processes may play a more important role than sorption processes for some permafrost soils. Also, Ca and C were found to be well-correlated for permafrost tunnel (PT) samples, as seen in other STXM-NEXAFS studies of soils (Chen et al., 2014a). This provides further evidence that polyvalent cations, such as Ca, may be an integral component of terrestrial organo-mineral associations that could be providing unknown benefits to C stability. Carbon stability is likely also dependent on OM composition, which was found to be heterogeneous across the PT chronosequence. With decreasing age, we found an increase in amino acid-rich moieties which likely indicates the presence of more proteins and dense microbial populations. Similar to other soil organo-mineral studies, carboxylic acids were observed to be highly present across all permafrost samples, strongly suggesting that the importance of carboxylic moieties for soil organo-mineral associations are not limited to temperate soils. Aliphatic moieties were present with decreasing abundance as the PT age increased, indicating that the importance of these moieties for C stability may be limited at certain permafrost ages. For all permafrost samples, Fe speciation was heterogeneous, with principle component analysis (PCA) revealing a mix of Fe(III), Fe(III)-Fe(II), and Fe(II) regions. Interestingly, C was found to be associated with all mixed valence regions. Aliphatic and aromatic moieties were predominately present in regions containing Fe(II). Therefore, this study provides evidence that the

chemistry of C cycling in permafrost soils is likely driven by heterogenous Fe phases and organo-mineral association development may be Fe speciation dependent.

To our knowledge, this is the first expansive spectroscopic study of permafrost soils across a chronosequence that provide spatially-resolved C, Ca, Fe, Al, and Si speciation and co-association results. Determining amino acid stability is likely greatly important when attempting to understand C cycling in these systems, which is less marked in temperate soils. Soil aluminosilicates (observed via Si and Al STXM analysis) were found to not co-associate with C to an observable degree, implying that aluminosilicates serve as a coating surface but may not provide the same stability that Fe-rich particles do. Lastly, we provide evidence that Ca may be important to C cycling processes. This is similar to other studies of soils and Fe oxides in the presence of Ca in the past 10 years; therefore, there is a growing body of work that Ca is a major component of C sequestration/transformation processes and our work suggests that C stability in permafrost soils may also be critically affected by C-Ca complexes. These findings have major impacts to how permafrost soils are studied in the future, as this provides the first spectroscopic baseline for beginning to understand C chemistry in permafrost soil systems at the moiety level. This research is ever critical, as global temperatures continue to rise and one of the world's largest terrestrial sinks of OC (i.e. permafrost) becomes at risk of mobilization to the atmosphere, creating a globally endangering climate change feedback loop.

Table 4.1: Elemental composition of permafrost soils following digestion using EPA Method 3051 (*aqua regia* digestion). All values are reported as percent by mass, with an error of approximately 0.1%.

	<b>Fe</b>	<b>C</b>	<b>N</b>	<b>Ca</b>	<b>Al</b>	<b>K</b>	<b>Mg</b>	<b>Mn</b>	<b>Na</b>	<b>P</b>	<b>S</b>
	%										
<b>PT_A</b>	2.54	3.27	0.22	0.82	1.38	0.09	0.70	0.03	0.06	0.06	0.11
<b>PT_B</b>	2.46	1.59	0.08	0.40	1.16	0.10	0.48	0.03	0.02	0.08	0.01
<b>PT_C</b>	2.81	1.09	0.09	0.53	1.83	0.15	0.64	0.04	0.02	0.06	0.02
<b>AT</b>	3.94	5.29	0.35	1.91	2.39	0.22	1.02	0.06	0.07	0.08	0.18
<b>FL</b>	2.67	1.82	0.19	0.65	1.87	0.16	0.67	0.04	0.03	0.05	0.02

Table 4.2: Pre-edge energy and edge-energy ranges used for average stack maps.

Element	Absorption Edge	Pre-edge Energy Stack Range (eV)	Edge Energy Stack Range (ev)
C	K	280-282	287.7-288.7
Ca	L <sub>2</sub>	350.3-350.7	352.3-352.9
Fe	L <sub>3</sub>	700-703	709.5-710.5
Al	K	1555-1557	1569.7-1570.3
Si	L	1840-1841	1846-1846.8

Table 4.3: Carbon K-edge NEXAFS assignments observed in Figure 4.8.

Peak Number	Peak Energies (eV)	C Functional Groups	Transition	References
(i)	285.2-285.6	Aromatic (C <sub>aromatic</sub> =C <sub>aromatic</sub> )	1s- $\pi^*$	Henneberry et al., 2009; Solomon et al., 2012; Chen et al., 2014
(ii)	286.7-286.9	Phenolic C <sub>aromatic</sub> -OH	1s- $\pi^*$	Wan et al., 2007; Solomon et al., 2012; Chen et al., 2014
(iii)	287.5	Aliphatic (C-H)	1s-3p/ $\sigma^*$	Wan et al., 2007; Solomon et al., 2013
(iv)	288.1	Amide-carbonyl (C=O)	1s- $\pi^*$	Wan et al., 2007; Solomon et al., 2014
(v)	288.5	Carboxylic (COOH)	1s- $\pi^*$	Wan et al., 2007; Solomon et al., 2012; Chen et al., 2014
(vi)	290.1	Carbonate	1s- $\pi^*$	Wan et al., 2007; Solomon et al., 2012; Chen et al., 2014

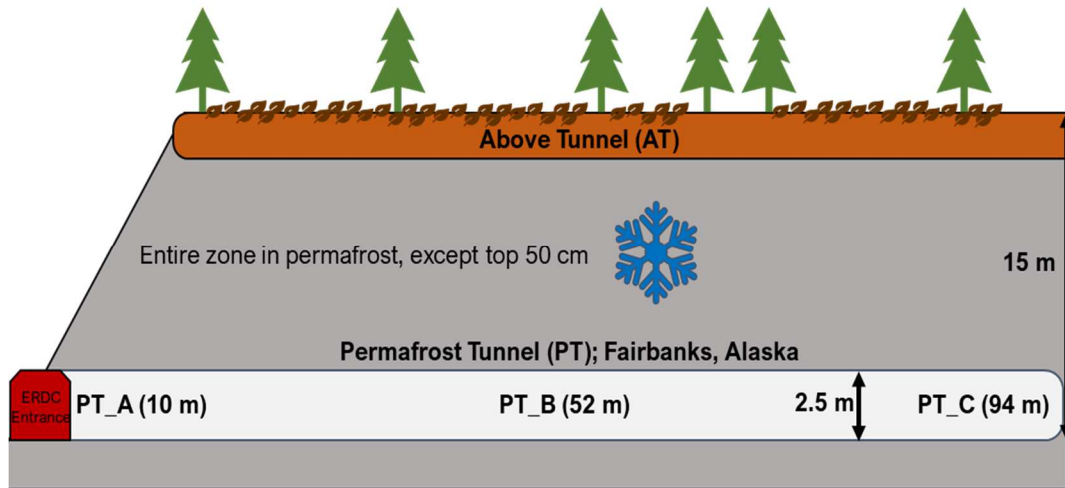


Figure 4.1: Cross-section of the Permafrost Tunnel Research Facility operated by the US Army Corps of Engineers Cold Regions Research and Engineering Laboratory (CREEL) in Fairbanks, Alaska. The sampling locations of four permafrost soils are shown as PT\_A, PT\_B, PT\_C, and AT.

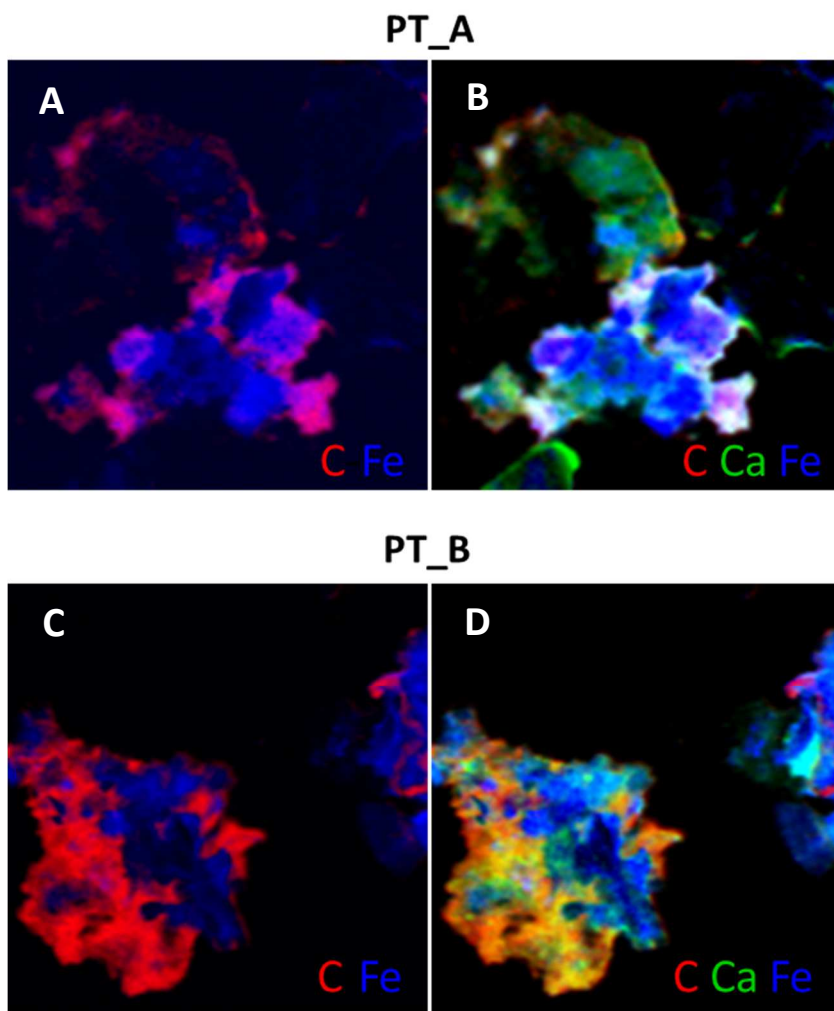


Figure 4.2: Color-coded composite RB and RGB optical density maps created from STXM-NEXAFS data. Red, green, and blue represent carbon, calcium, and iron, respectively. Maps are shown for soils PT\_A (A, B) and PT\_C (C, D).

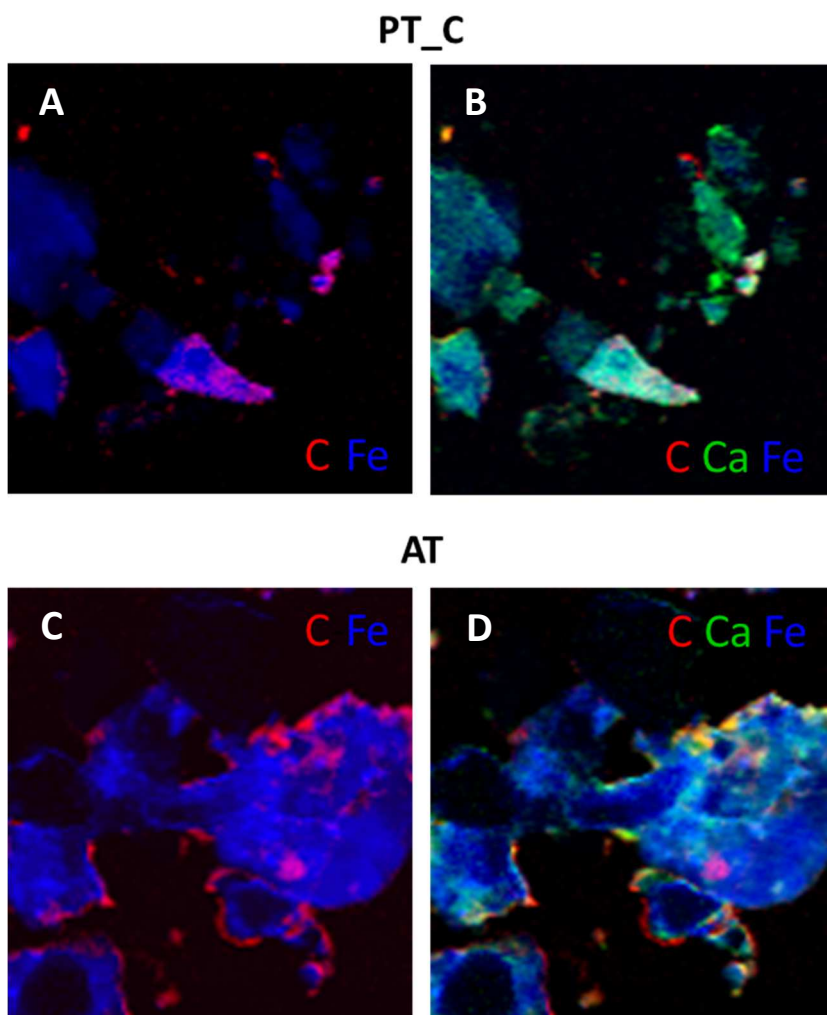


Figure 4.3: Color-coded composite RB and RGB optical density maps created from STXM-NEXAFS data. Red, green, and blue represent carbon, calcium, and iron, respectively. Maps are shown for soils PT\_C (A, B) and AT (C, D).

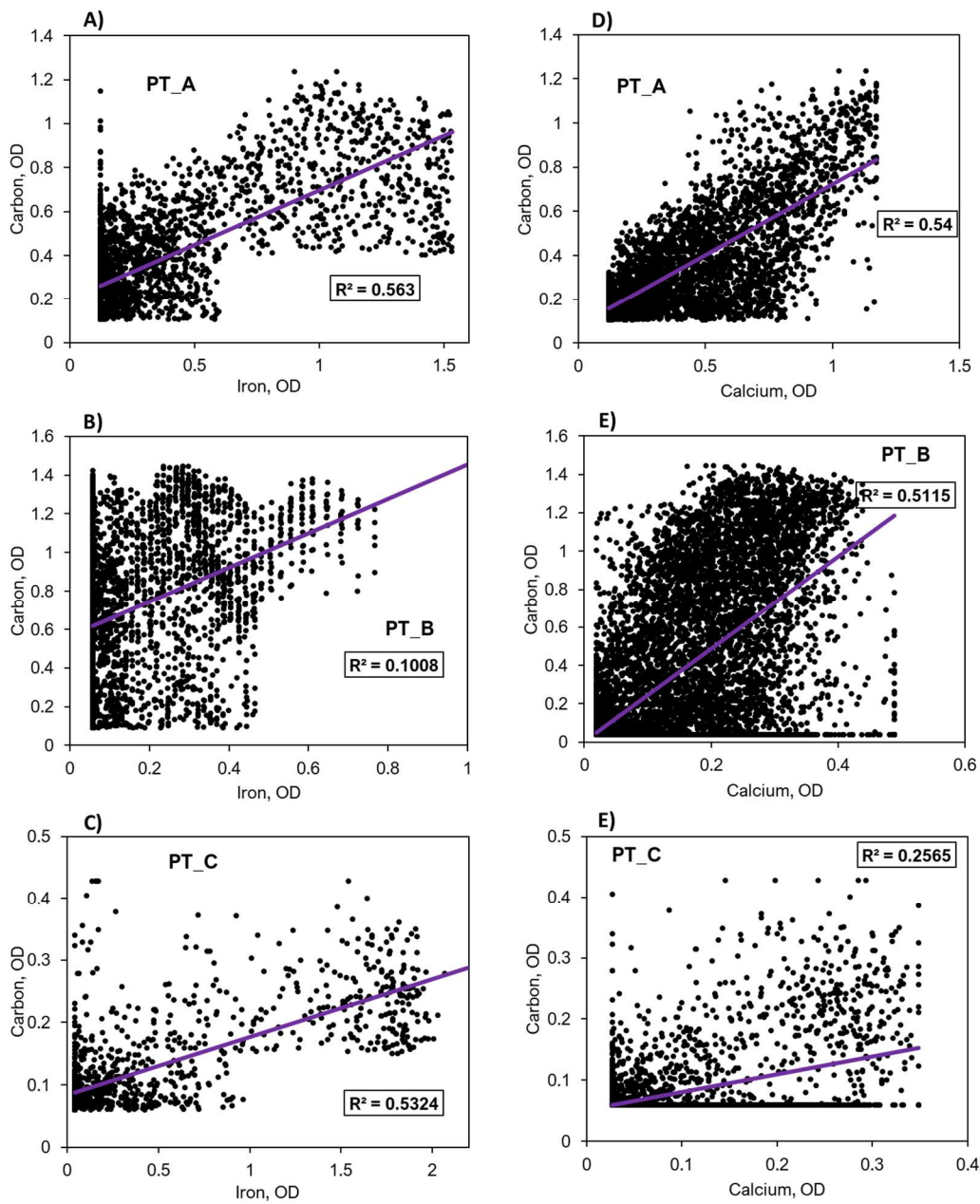


Figure 4.4: Elemental optical density correlation plots for spatially-resolved C signature versus Fe (A-C) and C versus Ca (D-E) for all PT soils. Linear correlation coefficients are provided for each plot.

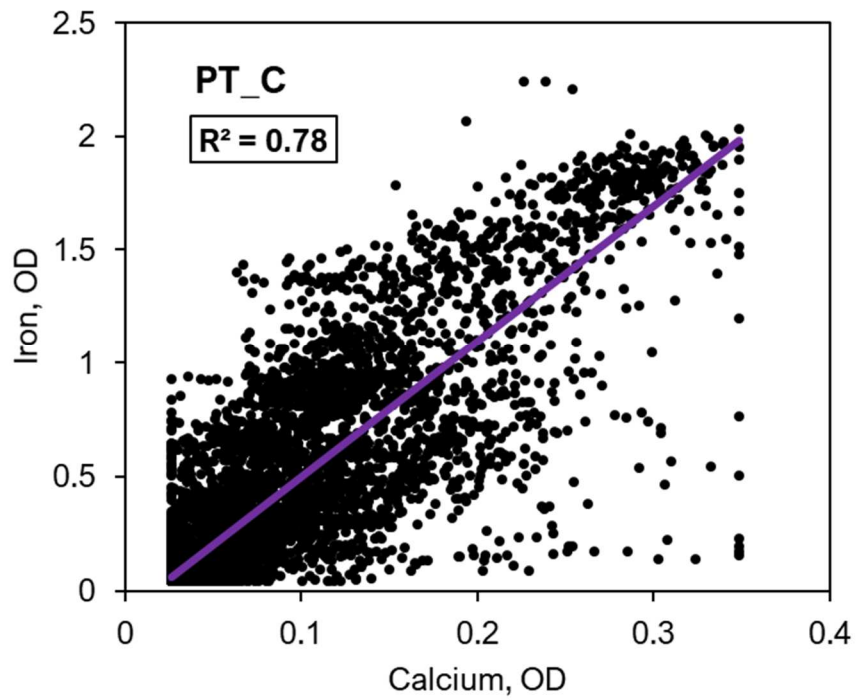


Figure 4.5: Elemental optical density correlation plots for spatially-resolved Fe signature versus Ca for soil PT\_C. Linear regression revealed Fe and Ca to be strongly correlated ( $R^2 = 0.78$ ). All other soils had no observable correlation between Fe and Ca.

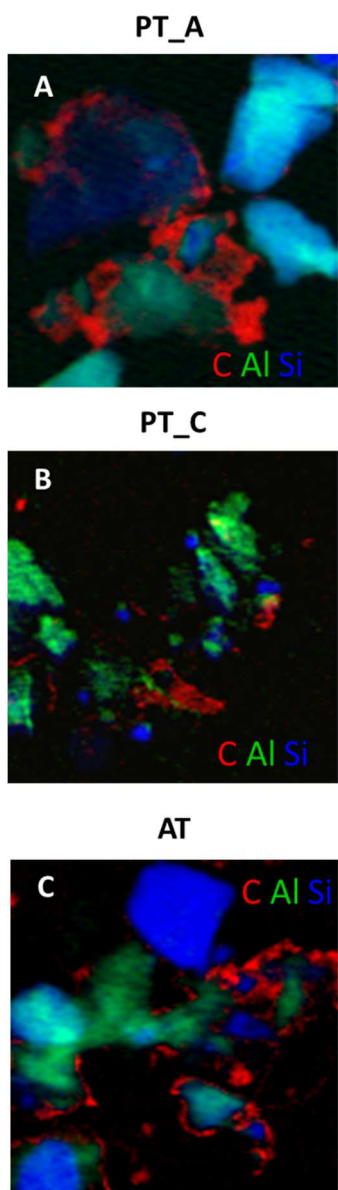


Figure 4.6: Color-coded composite RGB optical density maps created from STXM-NEXAFS data. Red, green, and blue represent carbon, aluminum, and silicon, respectively. Maps are shown for soils PT\_A (A), PT\_B (B), PT\_C (C). Note the coating of C to Al and Si phases without overlap, suggesting a lack of sorbed C by these phases. Al and Si phases are likely clay phyllosilicates mixed with quartz fragments.

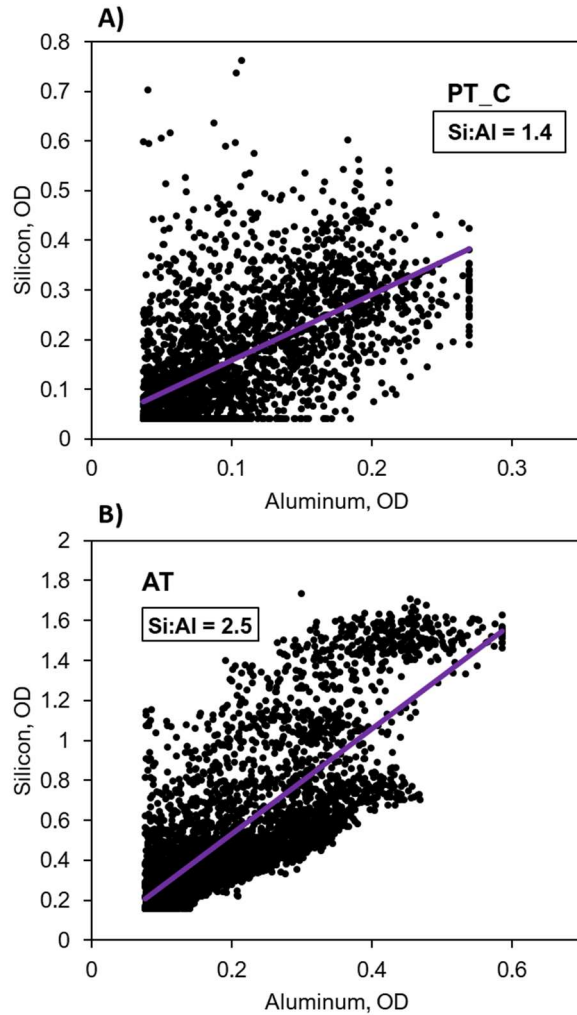


Figure 4.7: Elemental optical density correlation plots for spatially-resolved Si signature versus Al for a PT soil (PT\_C; A) compared to an AT soil (B). A linear regression line is present for each, with the slope indicating Si:Al ratio. Clay aluminosilicates typically have either a 1:1 or 2:1 ratio of tetrahedral to octahedral sheets, typically representing Si:Al. Therefore, PT\_C (Si:Al = 1.4) is likely a mixture of 2:1 and 1:1 aluminosilicates whereas AT (Si:Al = 2.5) likely consists predominately of 2:1. Values higher than 2 suggest that a component of the observed Si is potentially from sources other than clays, such as quartz.

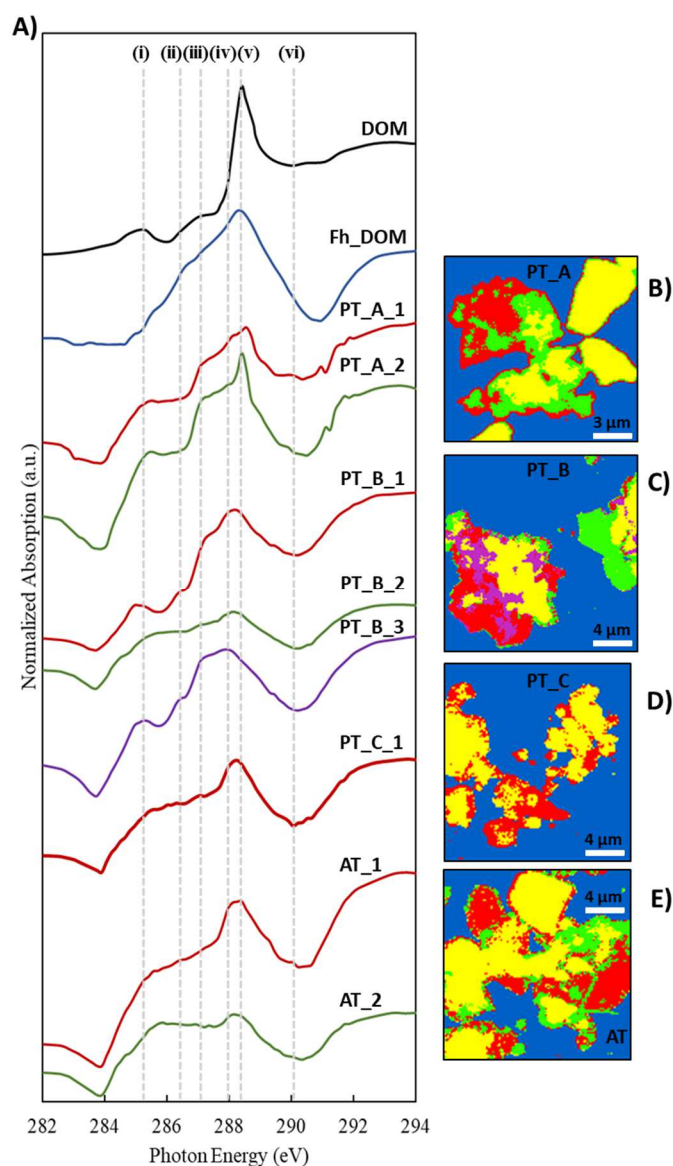


Figure 4.8: Carbon K-edge NEXAFS spectra (A) for unique clusters spatially identified using principal component analysis (PCA) for soils PT\_A (B), PT\_B (C), PT\_C (D), AT\_C (E). All spectra are color-coded to match the adjacent respective PCA map. Yellow regions were too thick ( $OD > 2.25$ ) for analysis. NEXAFS spectra for DI water-extractable leaf litter DOM and DOM sorbed to 2-line ferrihydrite are also included as standards. Peak assignments are found in Table 4.3.

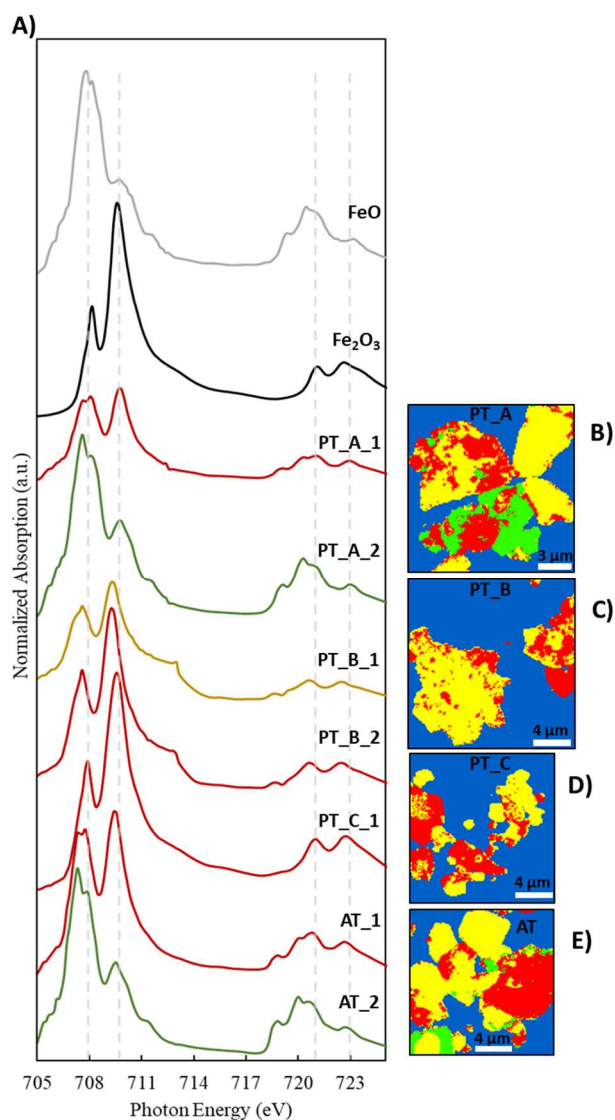


Figure 4.9: Iron L-edge NEXAFS spectra (A) for unique clusters spatially identified using principal component analysis (PCA) for soils PT\_A (B), PT\_B (C), PT\_C (D), AT\_C (E). All spectra are color-coded to match the adjacent respective PCA map. Yellow regions, excluding PT\_B, were too thick ( $OD > 2.25$ ) for analysis. Reference compounds of FeO and Fe<sub>2</sub>O<sub>3</sub> are included to comparatively assess the proportion of Fe(II) versus Fe(III), respectively, in samples. Vertical dashed lines correspond to (i) 708, (ii) 710, (iii) 721, and (iv) 723 eV.

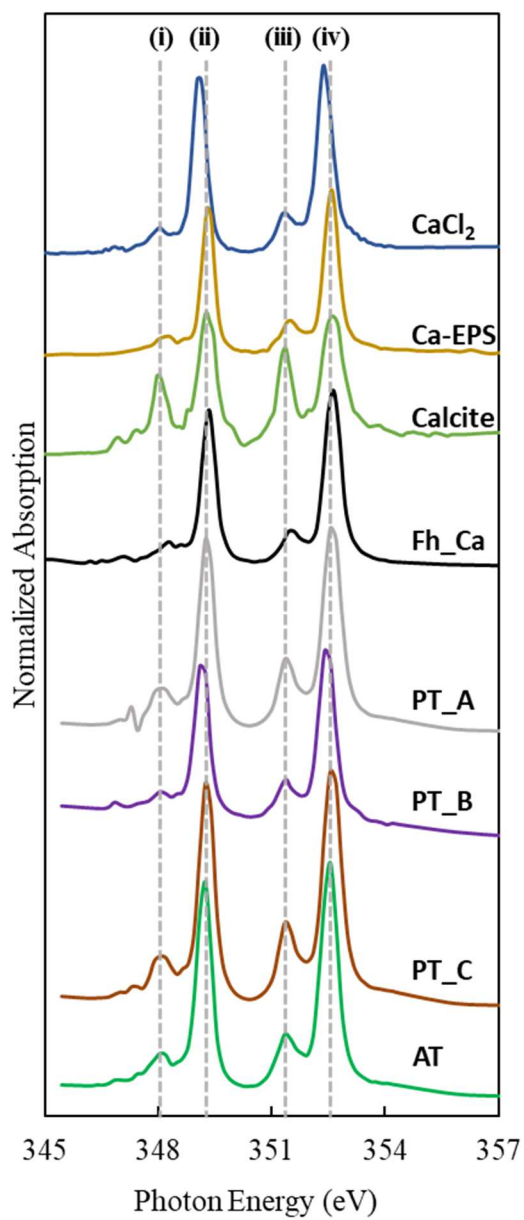


Figure 4.10: Calcium L-edge NEXAFS spectra for all permafrost soils, along with previously published reference standards for Ca sorbed to extracellular polymer structures,  $\text{CaCl}_2$ , and calcite (Chen et al., 2014a). Vertical dashed lines correspond to (i) 348.2, (ii) 349.3, (iii) 351.4, and (iv) 352.6 eV.

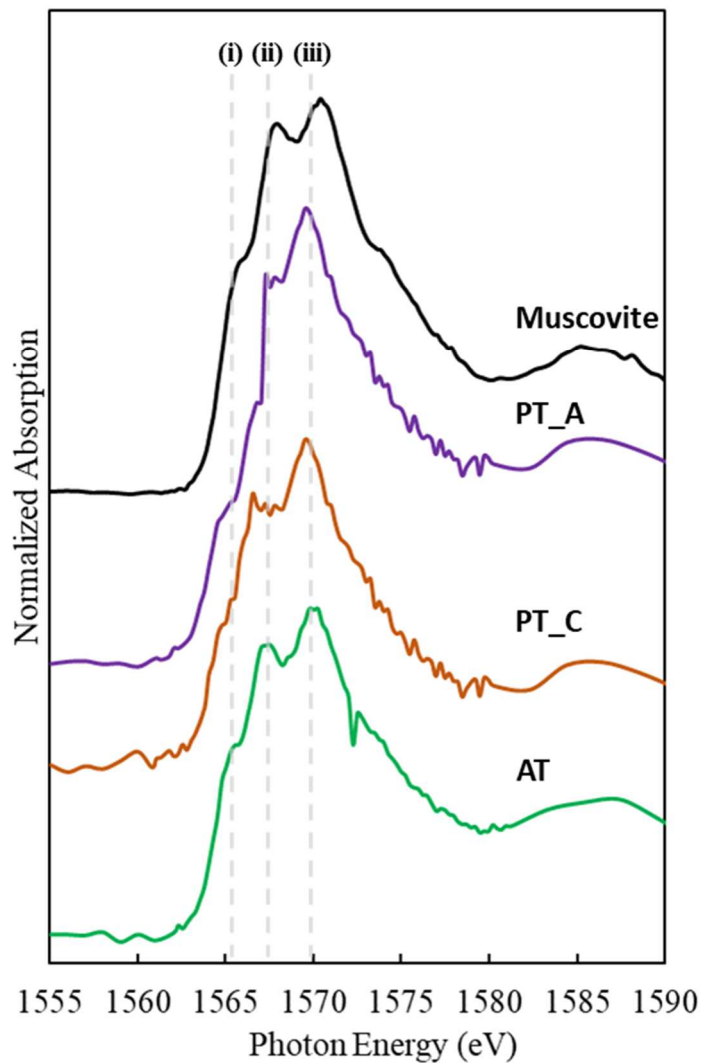


Figure 4.11: Aluminum L-edge NEXAFS spectra for soils PT\_A, PT\_C, and AT, along with a muscovite reference standard. Vertical dashed lines correspond to (i) 1565.6, (ii) 1567.7, and (iii) 1570.0 eV.

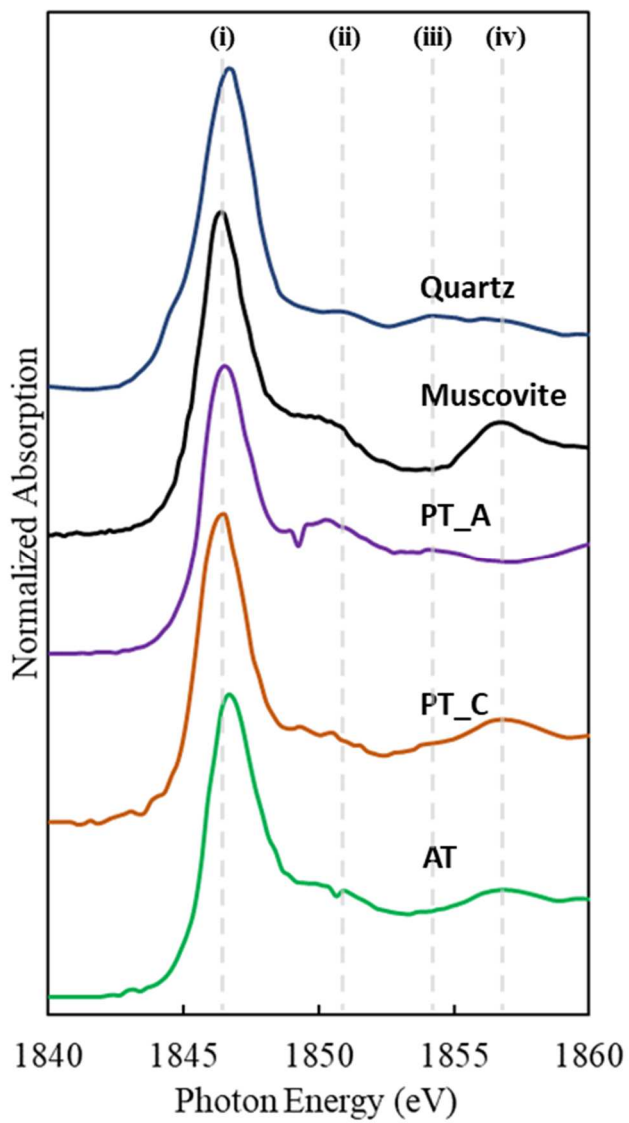


Figure 4.12: Silicon L-edge NEXAFS spectra for soils PT\_A, PT\_C, and AT, along with quartz and muscovite as reference standards. Vertical dashed lines correspond to (i) 1846.5, (ii) 1850.4, (iii) 1854.6 eV, and (iv) 1857.0.

## REFERENCES

- Adhikari, D., Sowers, T., Stuckey, J. W., Wang, X., Sparks, D. L., and Yang, Y. (2019). Formation and redox reactivity of ferrihydrite-organic carbon-calcium co-precipitates. *Geochimica et Cosmochimica Acta* 244, 86-98.
- Avneri-Katz, S., Young, R. B., McKenna, A. M., Chen, H., Corilo, Y. E., Polubesova, T., Borch, T., and Chefetz, B. (2017). Adsorptive fractionation of dissolved organic matter (DOM) by mineral soil: Macroscale approach and molecular insight. *Organic Geochemistry* 103, 113-124.
- Bolan, N. S., Adriano, D. C., Kunhikrishnan, A., James, T., McDowell, R., and Senesi, N. (2011). Dissolved organic matter: biogeochemistry, dynamics, and environmental significance in soils. In "Advances in agronomy", Vol. 110, pp. 1-75. Elsevier.
- Burkert, A., Douglas, T. A., Waldrop, M. P., and Mackelprang, R. (2019). Changes in the Active, Dead, and Dormant Microbial Community Structure Across a Pleistocene Permafrost Chronosequence. *Appl. Environ. Microbiol.* 85, e02646-18.
- Chen, C., Dynes, J. J., Wang, J., Karunakaran, C., and Sparks, D. L. (2014a). Soft X-ray spectromicroscopy study of mineral-organic matter associations in pasture soil clay fractions. *Environmental science & technology* 48, 6678-6686.
- Chen, C., Dynes, J. J., Wang, J., and Sparks, D. L. (2014b). Properties of Fe-organic matter associations via coprecipitation versus adsorption. *Environmental science & technology* 48, 13751-13759.
- Chen, C., Kukkadapu, R., and Sparks, D. L. (2015). Influence of Coprecipitated Organic Matter on Fe<sup>2+</sup> (aq)-Catalyzed Transformation of Ferrihydrite: Implications for Carbon Dynamics. *Environmental science & technology* 49, 10927-10936.

- Chen, C., and Sparks, D. L. (2015). Multi-elemental scanning transmission X-ray microscopy–near edge X-ray absorption fine structure spectroscopy assessment of organo–mineral associations in soils from reduced environments. *Environmental Chemistry* 12, 64-73.
- Coward, E. K., Ohno, T., and Plante, A. F. (2018). Adsorption and Molecular Fractionation of Dissolved Organic Matter on Iron-Bearing Mineral Matrices of Varying Crystallinity. *Environmental science & technology* 52, 1036-1044.
- Davidson, E. A., Trumbore, S. E., and Amundson, R. (2000). Biogeochemistry: soil warming and organic carbon content. *Nature* 408, 789-790.
- Douglas, T. A., Fortier, D., Shur, Y. L., Kanevskiy, M. Z., Guo, L., Cai, Y., and Bray, M. T. (2011). Biogeochemical and geocryological characteristics of wedge and thermokarst cave ice in the CRREL permafrost tunnel, Alaska. *Permafrost and Periglacial Processes* 22, 120-128.
- Drake, T. W., Wickland, K. P., Spencer, R. G., McKnight, D. M., and Striegl, R. G. (2015). Ancient low–molecular-weight organic acids in permafrost fuel rapid carbon dioxide production upon thaw. *Proceedings of the National Academy of Sciences* 112, 13946-13951.
- EPA, U. (1994). Microwave assisted acid digestion of sediments, sludges, soils, and oils. *SW-846 method A* 3051, 1997.
- Grybos, M., Davranche, M., Gruau, G., Petitjean, P., and Pédrot, M. (2009). Increasing pH drives organic matter solubilization from wetland soils under reducing conditions. *Geoderma* 154, 13-19.
- Gu, B., Schmitt, J., Chen, Z., Liang, L., and McCarthy, J. F. (1994). Adsorption and desorption of natural organic matter on iron oxide: mechanisms and models. *Environmental Science & Technology* 28, 38-46.
- Gu, B., Schmitt, J., Chen, Z., Liang, L., and McCarthy, J. F. (1995). Adsorption and desorption of different organic matter fractions on iron oxide. *Geochimica et Cosmochimica Acta* 59, 219-229.
- Hamilton, T. D., Craig, J. L., and Sellmann, P. V. (1988). The Fox permafrost tunnel: a late Quaternary geologic record in central Alaska. *Geological Society of America Bulletin* 100, 948-969.

- Hitchcock, A. aXis-2000 is an IDL-based analytical package 2000.
- Ildefonse, P., Cabaret, D., Saintavit, P., Calas, G., Flank, A.-M., and Lagarde, P. (1998). Aluminium X-ray absorption near edge structure in model compounds and Earth's surface minerals. *Physics and Chemistry of Minerals* 25, 112-121.
- Jacobsen, C., Wirick, S., Flynn, G., and Zimba, C. (2000). Soft X-ray spectroscopy from image sequences with sub-100 nm spatial resolution. *Journal of Microscopy* 197, 173-184.
- Jönsson, J., and Sherman, D. M. (2008). Sorption of As (III) and As (V) to siderite, green rust (fougerite) and magnetite: Implications for arsenic release in anoxic groundwaters. *Chemical Geology* 255, 173-181.
- Kaiser, K., and Guggenberger, G. (2000). The role of DOM sorption to mineral surfaces in the preservation of organic matter in soils. *Organic geochemistry* 31, 711-725.
- Kaiser, K., and Guggenberger, G. (2003). Mineral surfaces and soil organic matter. *European Journal of Soil Science* 54, 219-236.
- Kalbitz, K., Schwesig, D., Schmerwitz, J., Kaiser, K., Haumaier, L., Glaser, B., Ellerbrock, R., and Leinweber, P. (2003). Changes in properties of soil-derived dissolved organic matter induced by biodegradation. *Soil Biology and Biochemistry* 35, 1129-1142.
- Kalbitz, K., Solinger, S., Park, J.-H., Michalzik, B., and Matzner, E. (2000). Controls on the dynamics of dissolved organic matter in soils: a review. *Soil science* 165, 277-304.
- Kinyangi, J., Solomon, D., Liang, B., Lerotic, M., Wirick, S., and Lehmann, J. (2006). Nanoscale biogeocomplexity of the organomineral assemblage in soil. *Soil Science Society of America Journal* 70, 1708-1718.
- Kjellström, E., Nikulin, G., Strandberg, G., Christensen, O. B., Jacob, D., Keuler, K., Lenderink, G., van Meijgaard, E., Schär, C., and Somot, S. (2018). European climate change at global mean temperature increases of 1.5 and 2 degrees C above pre-industrial conditions as simulated by the EURO-CORDEX regional climate models. *Earth System Dynamics* 9, 459-478.

- Kleber, M., Eusterhues, K., Keiluweit, M., Mikutta, C., Mikutta, R., and Nico, P. S. (2015). Chapter one-mineral–organic associations: formation, properties, and relevance in soil environments. *Advances in agronomy* 130, 1-140.
- Kramer, M. G., and Chadwick, O. A. (2018). Climate-driven thresholds in reactive mineral retention of soil carbon at the global scale. *Nature Climate Change* 8, 1104.
- Lalonde, K., Mucci, A., Ouellet, A., and G elinas, Y. (2012). Preservation of organic matter in sediments promoted by iron. *Nature* 483, 198-200.
- Lehmann, J., Kinyangi, J., and Solomon, D. (2007). Organic matter stabilization in soil microaggregates: implications from spatial heterogeneity of organic carbon contents and carbon forms. *Biogeochemistry* 85, 45-57.
- Lehmann, J., and Solomon, D. (2010). Organic carbon chemistry in soils observed by synchrotron-based spectroscopy. In "Developments in soil science", Vol. 34, pp. 289-312. Elsevier.
- Lehmann, J., Solomon, D., Kinyangi, J., Dathe, L., Wirick, S., and Jacobsen, C. (2008). Spatial complexity of soil organic matter forms at nanometre scales. *Nature Geoscience* 1, 238.
- Lerotic, M., Jacobsen, C., Gillow, J., Francis, A., Wirick, S., Vogt, S., and Maser, J. (2005). Cluster analysis in soft X-ray spectromicroscopy: finding the patterns in complex specimens. *Journal of Electron Spectroscopy and Related Phenomena* 144, 1137-1143.
- Liang, B., Lehmann, J., Solomon, D., Kinyangi, J., Grossman, J., O'Neill, B., Skjemstad, J., Thies, J., Luizao, F., and Petersen, J. (2006). Black carbon increases cation exchange capacity in soils. *Soil Science Society of America Journal* 70, 1719-1730.
- Lv, J., Zhang, S., Wang, S., Luo, L., Cao, D., and Christie, P. (2016). Molecular-scale investigation with ESI-FT-ICR-MS on fractionation of dissolved organic matter induced by adsorption on iron oxyhydroxides. *Environmental science & technology* 50, 2328-2336.
- Mackelprang, R., Burkert, A., Haw, M., Mahendrarajah, T., Conaway, C. H., Douglas, T. A., and Waldrop, M. P. (2017). Microbial survival strategies in ancient permafrost: insights from metagenomics. *The ISME journal* 11, 2305.

- McKnight, D. M., Bencala, K. E., Zellweger, G. W., Aiken, G. R., Feder, G. L., and Thorn, K. A. (1992). Sorption of dissolved organic carbon by hydrous aluminum and iron oxides occurring at the confluence of Deer Creek with the Snake River, Summit County, Colorado. *Environmental science & technology* 26, 1388-1396.
- Mikutta, R., Mikutta, C., Kalbitz, K., Scheel, T., Kaiser, K., and Jahn, R. (2007). Biodegradation of forest floor organic matter bound to minerals via different binding mechanisms. *Geochimica et Cosmochimica Acta* 71, 2569-2590.
- Miot, J., Li, J., Benzerara, K., Sougrati, M. T., Ona-Nguema, G., Bernard, S., Jumas, J.-C., and Guyot, F. (2014). Formation of single domain magnetite by green rust oxidation promoted by microbial anaerobic nitrate-dependent iron oxidation. *Geochimica et Cosmochimica Acta* 139, 327-343.
- New, M., Liverman, D., Schroder, H., and Anderson, K. (2011). Four degrees and beyond: the potential for a global temperature increase of four degrees and its implications. The Royal Society Publishing.
- Osterkamp, T., and Romanovsky, V. (1999). Evidence for warming and thawing of discontinuous permafrost in Alaska. *Permafrost and Periglacial Processes* 10, 17-37.
- Pewe, T. L., and Sellmann, P. V. (1973). Geochemistry of permafrost and Quaternary stratigraphy. In "Permafrost: the North American contribution to the 2nd International Conference, Yakutsk, USSR National Academy of Science Press", pp. 166-170.
- Politi, Y., Metzler, R. A., Abrecht, M., Gilbert, B., Wilt, F. H., Sagi, I., Addadi, L., Weiner, S., and Gilbert, P. (2008). Transformation mechanism of amorphous calcium carbonate into calcite in the sea urchin larval spicule. *Proceedings of the National Academy of Sciences* 105, 17362-17366.
- Rogelj, J., Popp, A., Calvin, K. V., Luderer, G., Emmerling, J., Gernaat, D., Fujimori, S., Strefler, J., Hasegawa, T., and Marangoni, G. (2018). Scenarios towards limiting global mean temperature increase below 1.5 C. *Nature Climate Change* 8, 325.
- Scharlemann, J. P., Tanner, E. V., Hiederer, R., and Kapos, V. (2014). Global soil carbon: understanding and managing the largest terrestrial carbon pool. *Carbon Management* 5, 81-91.

- Schmidt, M. W., Torn, M. S., Abiven, S., Dittmar, T., Guggenberger, G., Janssens, I. A., Kleber, M., Kögel-Knabner, I., Lehmann, J., and Manning, D. A. (2011). Persistence of soil organic matter as an ecosystem property. *Nature* 478, 49-56.
- Schuur, E. A., Bockheim, J., Canadell, J. G., Euskirchen, E., Field, C. B., Goryachkin, S. V., Hagemann, S., Kuhry, P., Lafleur, P. M., and Lee, H. (2008). Vulnerability of permafrost carbon to climate change: Implications for the global carbon cycle. *BioScience* 58, 701-714.
- Schuur, E. A., McGuire, A. D., Schädel, C., Grosse, G., Harden, J., Hayes, D. J., Hugelius, G., Koven, C., Kuhry, P., and Lawrence, D. M. (2015). Climate change and the permafrost carbon feedback. *Nature* 520, 171.
- Sellmann, P. V. (1972). "Geology and Properties of Materials Exposed in the USACRREL Permafrost Tunnel." COLD REGIONS RESEARCH AND ENGINEERING LAB HANOVER NH.
- Shaw, S. A., Peak, D., and Hendry, M. J. (2009). Investigation of acidic dissolution of mixed clays between pH 1.0 and– 3.0 using Si and Al X-ray absorption near edge structure. *Geochimica et Cosmochimica Acta* 73, 4151-4165.
- Sodano, M., Lerda, C., Nisticò, R., Martin, M., Magnacca, G., Celi, L., and Said-Pullicino, D. (2017). Dissolved organic carbon retention by coprecipitation during the oxidation of ferrous iron. *Geoderma* 307, 19-29.
- Solomon, D., Lehmann, J., Harden, J., Wang, J., Kinyangi, J., Heymann, K., Karunakaran, C., Lu, Y., Wirick, S., and Jacobsen, C. (2012a). Micro-and nano-environments of carbon sequestration: Multi-element STXM–NEXAFS spectromicroscopy assessment of microbial carbon and mineral associations. *Chemical geology* 329, 53-73.
- Solomon, D., Lehmann, J., Wang, J., Kinyangi, J., Heymann, K., Lu, Y., Wirick, S., and Jacobsen, C. (2012b). Micro-and nano-environments of C sequestration in soil: A multi-elemental STXM–NEXAFS assessment of black C and organomineral associations. *Science of the Total Environment* 438, 372-388.
- Sowers, T., Adhikari, D., Wang, J., Yang, Y., and Sparks, D. L. (2018a). Spatial associations and chemical composition of organic carbon sequestered in Fe, Ca, and organic carbon ternary systems. *Environmental science & technology*.

- Sowers, T. D., Holden, K. L., Coward, E. K., and Sparks, D. L. (2019). Dissolved organic matter sorption and molecular fractionation by naturally-occurring bacteriogenic iron (oxyhydr) oxides. *Environmental science & technology*.
- Sowers, T. D., Stuckey, J. W., and Sparks, D. L. (2018b). The synergistic effect of calcium on organic carbon sequestration to ferrihydrite. *Geochemical transactions* 19, 4.
- Sparks, D. L. (2003). "Environmental soil chemistry," Academic press.
- Sposito, G. (2008). "The chemistry of soils," Oxford university press.
- Targulian, V., and Krasilnikov, P. (2007). Soil system and pedogenic processes: Self-organization, time scales, and environmental significance. *Catena* 71, 373-381.
- Waldrop, M. P., Wickland, K. P., White Iii, R., Berhe, A. A., Harden, J. W., and Romanovsky, V. E. (2010). Molecular investigations into a globally important carbon pool: Permafrost-protected carbon in Alaskan soils. *Global change biology* 16, 2543-2554.
- Wan, J., Tylliszczak, T., and Tokunaga, T. K. (2007). Organic carbon distribution, speciation, and elemental correlations within soil microaggregates: applications of STXM and NEXAFS spectroscopy. *Geochimica et Cosmochimica Acta* 71, 5439-5449.

## Appendix A

### PROBING THE OCCURRENCE AND ORGANO-MINERAL ASSOCIATIONS OF IRON, CALCIUM, AND ORGANIC MATTER TERNARY COMPLEXES

#### A.1 Copyright Information

© 2018a and 2018b Sowers et al. The work in this chapter has been published in the following journal: *Geochemical Transaction and Environmental Science and Technology*. The manuscript published in *Geochemical Transactions* is titled “The synergistic effect of calcium on organic carbon sequestration to ferrihydrite” (<https://doi.org/10.1186/s12932-018-0049-4>) and should be properly cited if referencing data from Chapter 2. The manuscript published in *Environmental Science and Technology* is titled “Spatial Associations and Chemical Composition of Organic Carbon Sequestered in Fe, Ca, and Organic Carbon Ternary Systems” (DOI: 10.1021/acs.est.8b01158) and should be properly cited if referencing data from Chapter 2.

## **Appendix B**

### **NATURALLY-OCCURRING BACTERIOGENIC IRON OXIDES: AN UNDERSTUDIED, UNIQUE ORGANIC MATTER SINK**

#### **B.1 Copyright Information**

© 2019 Sowers et al. The work in this chapter has been published in the following journal: Environmental Science and Technology. The manuscript published in Environmental Science and Technology is titled “Spatial Associations and Chemical Composition of Organic Carbon Sequestered in Fe, Ca, and Organic Carbon Ternary Systems” (DOI: 10.1021/acs.est.9b00540) and should be properly cited if referencing data from Chapter 3.